Light-Driven Electron Transfer and Catalysis in CdS Nanocrystal–Hydrogenase Biohybrid Complexes

by

Helena Rose Keller

B.S. Michigan Technological University, 2014

M.S. University of Colorado, 2020

A thesis submitted to the

Faculty of the Graduate School of the

University of Colorado in partial fulfillment

of the requirement for the degree of

Doctor of Philosophy

Materials Science and Engineering

2024

Committee Members:

Gordana Dukovic

Paul W. King

Jihye Park

Garry Rumbles

Niels H. Damrauer

Keller, Helena Rose (Ph.D., Materials Science and Engineering)

Light-Driven Electron Transfer and Catalysis
in CdS Nanocrystal-Hydrogenase Biohybrid Complexes

Thesis directed by Professor Gordana Dukovic

Abstract

Electron transfer (ET) pathways govern our world on one of the most fundamental levels, determining the outcomes of countless complex chemical processes that build our society. Controlling ET and driving chemical product formation effectively, however, is a substantial challenge. Coupling semiconductor nanocrystals with redox enzymes enables opportunities to drive complex, multielectron chemistry with a renewable solar energy source, while at the same time opening up a world of possibilities to study the fundamental principles behind the control of ET in these systems. This dissertation investigates ET pathways and catalysis in photoexcited CdS nanocrystals and CdS nanocrystal-[FeFe] hydrogenase biohybrid complexes. Each of the four projects described here focuses on ET in a different part of this system: 1) Interfacial nanocrystal-to-hydrogenase ET, with transient absorption spectroscopy and photochemical H_2 production with a size series of CdS quantum dots (QDs). We find that QD properties other than size, likely QD surface properties, have the greater influence on the photocatalytic outcomes here. 2) The kinetics of ET within a hydrogenase photoreduced by CdS QDs. We model the resulting hydrogenase redox species' kinetics from photochemical electron paramagnetic resonance spectroscopy experiments to gain a picture of the thermodynamic landscape of the intraprotein ET pathway. This work provides insight into the properties of the hydrogenase iron-sulfur clusters and organometallic active site that tune the directionality of ET and catalysis in this enzyme. 3) Examination of the nanocrystal-hydrogenase photochemical system as a whole, using experimental H_2 production trends and kinetic Monte Carlo simulations to reveal how key parameters such as hole transfer, catalyst turnover, and back-transfer processes determine rate-limiting conditions. 4) Investigation of a charge transfer pathway in CdS nanocrystals which, under certain conditions, leads to long-lived photoreduced states even in the absence of an external electron donor. We discuss the conditions under which this process occurs, and its relevance for other CdS photochemistries.

Acknowledgements

An incredible number of people have contributed to this work and my experiences over the years, both directly and indirectly, and I only hope I can do justice to a fraction of what this support has meant to me.

First, Gordana, thank you for your tireless efforts and mentorship, always supporting my interests and goals 100%, I couldn't have asked for a better advisor! You helped me to understand the perspective of a chemist in addition to that of an engineer, and how to aim for high impact goals. I've learned so much from you on how to craft a research narrative both in writing and presentation, how to negotiate for myself, and stay organized in the face of multiple simultaneous projects.

Thank you to my committee members Garry Rumbles, Jihye Park, and Niels Damrauer, for your time, energy, and interest that you took in my work, I greatly appreciate your support. I would also like to thank and remember Jeffery Cameron, who served on my comprehensive exam committee and who I got to know a bit better at a conference last summer; he was an amazing scientist and generous person who is now gone too soon.

Next, to our amazing collaborators. Paul, thank you for your constant support and patience discussing the many hydrogenase questions I've had over the years; not only your support but your enthusiasm for the work helped get me more excited about the work time and time again. I can't thank you enough for all the time and energy that you give. It's also thanks to you that my nanocrystal-hydrogenase work exists at all! David, thank you for all your support for my SCGSR experience that expanded the boundaries of my skills and the EPR work I got to do is now one of my favorite projects I've worked on. Thank you for all the time and effort you put in, both at the application stage and in training and advising on this work. Kate, we didn't get to overlap for long,

but you set a precedent of diligence and thoroughness that set me up for success in your wake. Effie, you're an EPR wizard and thank you for being both a great colleague and friend, all the hours you've spent training me in both wet lab and EPR knowledge. I also can't thank enough all of you who I've gotten to know at NREL for the daily help in the lab, as well as the friendship and making the long hours fun! Seth, Greg, Matt, there were so many days at the lab I couldn't have gotten anything done without you, your patience and friendly faces always willing to help at a moment's notice or discuss something interesting about research or otherwise, you made my time there so much fun even on long stressful days! Sarah and Isaac, you guys also really made my initial months at NREL fun and your energy really reignited my own! To Eric, Saad, Chris, Jon, thanks to you as well for all the little things day in and day out at the lab and outside of it. Peter, it's been so much fun to have you come in on the nanocrystal-enzyme work and gain inspiration from your many ideas and insights! I also want to thank Sean and Andrew at Boston University—the OGOR work has also been a big part of my PhD and thank you for all your efforts and support for it!

To Dukovic group alums and mentors—first and foremost, Hayden you were an amazing mentor, I admire how smart and meticulous you are and how effectively you built up especially the OGOR work and set me up with all the tools I needed for success. I owe it all to you! James thank you for all your help and guidance in my first couple years, for setting me up with the kinetic Monte Carlo work and all the time you've dedicated to it since! Orion thank you for always being down for an interesting scientific discussion or writing up a quick code, and ingenious pranks. Jesse you were an essential part of my nanocrystal-enzyme education and a excellent desk neighbor, and made me feel welcome when I first arrived. Katie, thank you for our many long hours running photocharging and TA experiments together, and everything I got to learn from you

about nanocrystal photophysics and spectroscopy. Thank you as well to Kristina, Leah, Marta, Nicholas, Shelby, who all made for such a welcoming and fun time starting out in the group.

To my current and ongoing Dukovic labmates, for everything in and outside the lab, Skylar, Benny, Olivia, Sophie, Daria, you guys are amazing and I can't wait to see how your research and your lives go on from here. To those of you that I've spent nearly to my entire time here with: Ben, thanks for being an indispensable OGOR partner-in-crime and the many long hours and days of experiments and discussions figuring out this challenging project—we've been through a lot and I've always admired your organization and thoroughness! Lauren, I've learned so much from you and your approach to research, whenever I've been stuck you've helped me realize the path forward and I really admire how you dive in and tackle new things in the lab as if you've already been doing them for years! Madison, from the moment you arrived you've been a paragon of knowledge—from your very first few months here, thank you for always being down to share your laser and data analysis wisdom, to talk through challenging problems, research or otherwise. I can't imagine my time here without you guys!

I wouldn't have gotten to this point without the experiences I had before ever setting foot in grad school: my high school biology teacher Mike Niziolek, who inspired us to not just memorize facts, but to think about how and why the world works the way it does. My undergraduate research mentors, David Shonnard, Karen McDonald, Lucas Arzola, and Kane Jennings, all of whom were dedicated mentors who instrumental in my developing research experience and realization that this was the path I wanted to pursue. My colleagues in Nauela, especially Lembrança and my science club students who taught me new perspectives on teaching science and what it means in different parts of the world.

To the many friends who have provided a listening ear and reminded me of life outside of grad school: Megan (Renny), Suryansh, Nora, Greg, Mollie, Megan (Dalbec), Ainslie, Boulder Chorale members. To family, who have supported me throughout my busy and stressed states of mind over the years, especially here in Colorado and nearby: Jane, Terry, Jen, Arthur, Bethany, Megan, Xavier, Ben, Greg, Alice. Getting to see you all more often and get to know you better these last years. To my family in Austria and Germany who have been incredible cheerleaders from afar: Judith, Manuela, Michel, and Claudia. I also want to remember the family members who have left us; Anja and Christoph, who were both taken from us far too soon. And Oma Brigitte, Roger, Solveig, who showed me what a full and engaged life looks like. My brother David, your constant support and passion you put into things constantly reminds me to do the same. And to my parents, Myrna and Florian, who always encouraged my interests from the beginning, with many trips to the Minnesota Science Museum and bedtime astronomy stories, listened patiently to my many attempts to explain my research, and helped me get to where I am today.

Last but not least, this work would not have been possible without several important funding sources: the CU Boulder Dean's Innovation Assistantship, the Graduate Assistantship in Areas of National Need (GAANN) in Soft Materials, the National Science Foundation Graduate Research Fellowship Program (NSF GRFP) under Grant No. DGE 1650115, the U.S. Department of Energy Office of Science Graduate Student Research (SCGSR) Program, and the National Science Foundation under Award No. CHE 2204639.

Table of Contents

List of Figures

List of Tables

Chapter 1
Introduction

1.1. Motivation

Our society relies on the production of a wide range of materials and products for every aspect of life—food, fuel, medicine, infrastructure, and so much more. The production of all these materials requires energy, and in some cases, complex chemical conversion processes.[1–4] The most widely used sources of energy today come from fossil fuels—finite resources which actively pollute our global atmosphere.[5,6] Carbon dioxide and methane emissions from the burning of fossil fuels are responsible for the increasing the atmospheric greenhouse effect, inducing climate change which has already accelerated the rate of extreme weather around the world, damaging agriculture and ecosystems.[7] Other fossil fuel emissions are the cause of numerous human health hazards.[8]

Creating a more sustainable world will require addressing two great challenges: learning to produce materials more efficiently, and with renewable energy sources. To this first point, increasing the efficiency of chemical conversion reactions requires fundamental understanding of how to control one of the most integral processes happening at the sub-atomic scale: electron transfer (ET). Electrons are the source of chemical bonding, the process which determines molecular structure and function.[9] As a result, many chemical reactions involve ET from one species to another to form or break chemical bonds—referred to as redox reactions.[10] These are often multielectron reactions, and the greater the number of ETs and intermediate steps, the greater the chances for inefficiencies such as back- or side-reactions to occur. To facilitate such reactions, chemical catalysts are often employed; these are components able to decrease the activation energy of a reaction step, improving the rate, efficiency, and selectivity of the process.[11] However,

designing effective catalysts that truly succeed at these goals is a multifaceted and challenging endeavor.[12–16]

Fortunately, nature is several steps ahead of us; biological catalysts known as enzymes are protein structures that have evolved to carry out complex chemistries with incredible efficiency and selectivity.[17,18] Redox enzymes of numerous types exist in all living organisms, carrying out thousands of reactions that synthetic catalysts frequently struggle to achieve at the same level.[19,20] Many factors contribute to enzymes' success: their physical and chemical structure, as well as electronic and thermodynamic properties of their internal components all work to control the directionality of ET and catalysis in enzyme-driven chemistry.[21–25] The better we can understand the interplay of these varying factors and how they facilitate the flow of electrons for specific chemical outcomes, the better we can design efficient methods of producing valuable material products.

To study ET in complex chemical reaction systems, we need means of controlling the initiation of the ET process. In their native cellular environments, ET to and from enzymes is often carried out by a co-protein which acts as a redox shuttle.[26–28] For ET to occur, the co-protein binds to the enzyme at a specific surface site, facilitated by compatible surface structure and electrostatic interactions between the two components.[29] For each ET event, a co-protein must find, bind to, and then de-bind from the enzyme. As a result, ET to the enzyme in the native system is diffusion-limited and controlling the timing of ET in an experimental setting is challenging. An alternate approach is to use a different source of electrons to drive enzyme chemistry. Electrode surfaces and photoactive materials have been used to drive charge transfer to enzymes for decades; more recently, semiconductor nanocrystals have become an increasingly versatile material for photochemistry.[30–34] Several of their key properties—size, shape, surface chemistry, and band gap

energy—are all readily tunable and well-suited for controlling ET to redox enzymes with light.[35–38] This biohybrid approach enables us to demonstrate that complex, multielectron chemistry can be driven with a renewable solar energy source, while at the same time opening up a world of possibilities to study the fundamental principles behind the control of ET in these systems.

1.2. Background

1.2.1 Semiconductor Nanocrystals

Semiconductors are materials whose electronic structure is characterized by a band gap, such that to photoexcite an electron from energy levels below the band gap (valence band) to above (conduction band), the incident light must be at an energy at or above that of the band gap.[39] The photoexcitation of the electron leaves behind a so-called "hole" in the valence band, and together the photoexcited electron and hole form what is known as an exciton. The exciton is delocalized over an area defined by the Bohr exciton radius, whose size depends on the chemical composition of the semiconductor.[40] When a semiconductor crystal is made small enough that it approaches its Bohr exciton radius, it becomes quantum-confined—a phenomenon in which the continuous energy levels in the valence and conduction bands become discrete states at the band edges, and the band gap energy increases.[41] As a result, semiconductor nanocrystal size becomes a means by which to tune its absorbance spectrum as well as the energy of the photoexcited electrons. The more quantum-confined dimensions a semiconductor nanocrystal has, the greater the range of tunability of the band gap energy.[36,37,41] In this work we will discuss semiconductor nanorods—confined in two dimensions—as well as spherical nanocrystals, or quantum dots (QDs)—which are confined in all three dimensions.

The other key feature of semiconductor nanocrystals is their surface chemistry. To enable colloidal stability, nanocrystals may be functionalized with surface-capping organic ligands. The

polarity and functional groups of the ligands determine their surface charge, the solvents in which the nanocrystals are colloidally stable, and impact their photophysical and photochemical properties.[42–46] In some systems, it has been proposed that photoexcited charges can transfer to a surface ligand, which then de-binds from the nanocrystal—as discussed in Chapter 5.[47] Meanwhile, undercoordinated surface atoms on a nanocrystal, when not passivated by ligands, can form mid-band gap states to which photoexcited electrons or holes can become localized, or "trapped" on the nanocrystal surface.[43,48,49] Photoexcited charge carrier trapping and electron-hole recombination are the two primary pathways of intrinsic semiconductor nanocrystal excited state decay with which ET pathways to an external acceptor—such as a redox enzyme—must compete.[34]

1.2.2 Hydrogenase Enzymes

Hydrogenases are redox enzymes which catalyze the reversible reaction of two protons (H^+) with two electrons (e^-) to form hydrogen gas (H_2), as shown in Eqn (1):

$$2H^+ + 2e^- \leftrightarrow H_2 \,. \tag{1}$$

H_2 is a potential clean combustion fuel alternative to fossil fuels, as well as a source of electrons in other chemical reactions—H_2 oxidation drives important metabolic reactions in many microorganisms.[50–52] Hydrogenases are metalloenzymes: enzymes containing a transition metal ion cofactor which contributes to their catalytic function.[53] There are three classes of hydrogenases, categorized based on the identity of their active site cofactor: [FeFe], [NiFe], and [Fe].[50–52] We focus on [FeFe]-hydrogenases, whose diiron-containing active site is termed the H-cluster. Many [FeFe]-hydrogenases also contain one or more iron-sulfur cofactors (F-clusters), which function in the transport of electrons between the H-cluster and a native ferredoxin co-protein redox shuttle.[54–56] Within the [FeFe]-hydrogenase family exists a wide range in the catalytic bias—

defined as the relative rate of H_2 production over the H_2 oxidation rate—spanning at least six orders of magnitude.[57] Most [FeFe]-hydrogenases are biased more strongly in the H_2 oxidation direction, but some have shown preference for the reduction direction.[57–62] Structural, electronic, and thermodynamic properties of both the H- and F-clusters have been shown to be important contributors to the directionality of the intraprotein ET pathway and overall catalytic bias, but there is still much to be learned about the details of these contributing parameters, as will be discussed further in Chapter 3.

1.2.3 Cadmium Chalcogenide Nanocrystals with [FeFe]-Hydrogenases

Cadmium chalcogenide nanocrystals (CdS, CdSe, CdTe) have been coupled with [FeFe]-hydrogenases for several investigations of nanocrystal-hydrogenase binding, ET, and photochemical H_2 production (**Figure 1**).[63–70] Their band edge potentials are at suitable levels to enable a driving force for ET to hydrogenases, as well as the use of ascorbic acid as a compatible sacrificial photoexcited hole scavenger in the system.[63,65] Finally, the tunability of cadmium chalcogenide nanocrystal size, shape, electronic structure, and surface chemistry allows for many avenues through which to modulate interactions with—and ET to—redox enzymes. One method of coupling nanocrystals with hydrogenases is by facilitating an electrostatic interaction in mimicry of the native co-protein to enzyme binding.[34,63,65] The surfaces of ferredoxins—the co-protein redox shuttles for many [FeFe]-hydrogenases—are predominantly negatively-charged and bind to a corresponding positively-charged patch on the hydrogenase near the distal F-cluster where inter-protein charge transfer occurs.[52,55] Nanocrystal surface charge can be tuned to mimic this property of the ferredoxin by the use of surface-capping ligands such as a mercaptopropionate, which due to its solvent-facing carboxylic acid group imparts a negative surface charge to the nanocrystal surface in neutral pH conditions.[63,65,71,72] Prior work with mercaptopropionate-capped

CdS nanorods paired with [FeFe]-hydrogenase I from *Clostridium acetobutylicum* (CaI) supported that the nanorods compete with ferredoxin binding to CaI.[65] This proposed site of nanocrystal binding to CaI was also supported by measurements of ET from nanorods to CaI compared with ET to catalytically-inactive CaI, and by photochemical electron paramagnetic resonance spectroscopy experiments on illuminated CdSe QD-CaI complexes.[66,70]

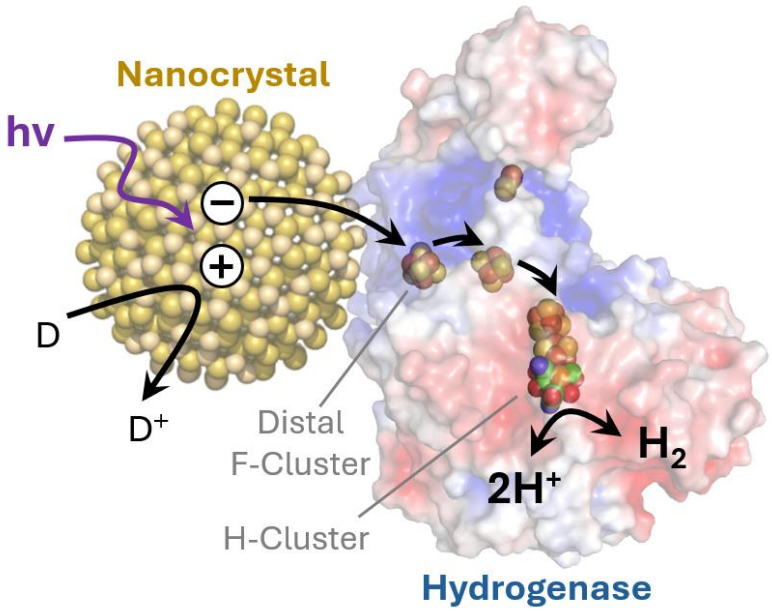

Figure 1.1: Scheme of ET and photochemical H_2 production in a cadmium chalcogenide nanocrystal-hydrogenase biohybrid. The nanocrystal is capped with mercaptopropionate ligands (not pictured), imparting a negative surface charge which binds to the positively-charged (blue) patch of the hydrogenase near the distal F-cluster. This protein crystal structure is of [FeFe] hydrogenase I from *Clostridium pasteurianum* (PDB 3C8Y), which serves as a homolog for CaI.[63,73] Photoexcited holes are scavenged by a sacrificial electron donor (D).

The [FeFe]-hydrogenase CaI mentioned above has been coupled with several types of cadmium chalcogenide nanocrystals including CdTe QDs, CdS nanorods, and CdSe QDs for photoreduction and photochemical H_2 production.[63,65–67,70] Quantum yields (QY) of H_2 production in these systems have been as high as 20%.[65] The use of nanorods enabled increased light absorption per particle compared to QDs, as well as higher CaI:nanocrystal molar ratios which revealed decreased photochemical H_2 production at the high CaI concentrations.[65] This work also

demonstrated a linear dependence of H_2 production on illumination intensity.[65] In Chapter 4, we revisit these CdS nanorod-CaI results and their implications for the interplay of nanorod-CaI system parameters. Further studies using transient absorption (TA) and time-resolved photoluminescence spectroscopy investigated the rates and quantum efficiencies of ET from cadmium chalcogenide nanocrystals to CaI. In CdS nanorod-CaI complexes, kinetic modeling of excited state decays from TA experiments found the rate constant of ET to be on the order of 10^7 s^{-1} with 3-mercaptopropionate-capped nanorods, decreasing exponentially with increasing ligand length.[66–69] In CdTe QD-CaI samples, the rate of ET from time-resolved photoluminescence (normalized by the number of bound CaI) was independent of CdTe QD size for diameters 2.0 to 3.5 nm.[64] In Chapter 2, we expand the investigation of ET rates and photochemical H_2 production in a series of CdS QDs of varying diameters 3.3 to 5.3 nm.

1.3. Summary and Dissertation Overview

Electron transfer pathways govern our world on one of the most fundamental levels, determining the outcome of countless complex chemical processes that build our society. Controlling ET and driving chemical product formation effectively, however, is a substantial challenge. Through the use of light-absorbing materials with highly tunable properties, combined with the most sophisticated catalysts grown by nature, we can further our understanding of the factors influencing electron flow.

The goal of this thesis work is to investigate ET pathways and catalysis in photoexcited CdS nanocrystals and CdS nanocrystal-[FeFe] hydrogenase biohybrid complexes. Each chapter examines ET in a different part of the system: Chapter 2 focuses on interfacial nanocrystal-to-hydrogenase ET, Chapter 3 on the kinetics of ET within a hydrogenase, Chapter 4 explores the nanocrystal-hydrogenase photochemical system as a whole, scrutinizing how key parameters

determine rate-limiting conditions, and Chapter 5 investigates a charge transfer pathway in CdS nanocrystals by themselves, and the relevance this process could have for CdS photochemistry.

Specifically, Chapter 2 examines the rate of ET to hydrogenase and photochemical H_2 production with a size series of CdS QDs, finding that QD properties other than size have the greater influence over CdS QD-hydrogenase interactions and H_2 production. Chapter 3 details the rise and decay of redox species within a hydrogenase photoreduced by CdS QDs, and models the resulting species' kinetics to gain a picture of the thermodynamic landscape of the intraprotein ET pathway. This work provides insight into how the properties of both the F- and H-clusters tune the directionality of ET and catalysis in this enzyme. Chapter 4 investigates experimental trends in photochemical CdS nanorod-hydrogenase H_2 production with the use of kinetic Monte Carlo simulations to understand the underlying processes limiting the catalytic output, particularly hole transfer, catalyst turnover, and back-transfer processes.

Chapter 5 is an adaptation of a 2021 Journal of Physical Chemistry C article which investigates the origin of long-lived photoreduced CdS nanocrystals in the absence of an external electron donor.[47] This photoreduction effect depends on both the CdS nanocrystal surface-capping ligand and the solvent; we propose a mechanism by which the photoexcited hole transfers to the surface ligand, which then de-binds from the nanocrystal. Notably, we find that ligand-mediated photocharging is not present in mercaptopropionate-capped CdS nanocrystals, only short-lived solvent-mediated photocharging when a hole scavenger is present. While the intrinsic photocharging process is therefore not involved in the CdS nanocrystal-hydrogenase work, we discuss relevant considerations for other CdS photochemical systems.

Chapter 2

Light-Driven Electron Transfer and H_2 Production of QD-Hydrogenase Complexes with CdS QDs of Varying Diameters

2.1. Abstract

Colloidal CdS nanocrystals coupled with [FeFe]-hydrogenase I from *Clostridium acetobutylicum* (CaI) are capable of driving enzymatic H_2 production with light. This work investigates interfacial photoexcited electron transfer (ET) to CaI and the resulting H_2 production in CdS QD-CaI complexes of varying CdS QD size 3.3 to 5.3 nm. We used transient absorption (TA) spectroscopy to monitor the CaI-induced changes to the nanocrystal photoexcited electron decay. Modeling of the TA kinetics demonstrated two CaI-induced excited state decay pathways, one on the order of 10^8 s^{-1} present in all the QDs tested, and a faster decay of 10^{10} s^{-1} present in all but the largest two QD of diameters 5.0 and 5.3 nm. The values of these rate constants appear to be independent of QD size, suggesting that the rate of ET to CaI does not vary with the driving force for ET in this CdS QD size range. The average number of CaI bound per QD varied markedly with select QDs, though QD characteristics other than size appear to be the dominating factor in CdS QD-CaI binding affinity. Photochemical H_2 production showed that the quantum yield of H_2 did not trend with the quantum efficiency of ET as calculated from the TA kinetics, demonstrating that different QDs with CaI may exhibit differences in aspects of the photochemical system other than ET or QD-CaI binding, or that not all of the CaI-induced excited state decay can be attributed to catalysis-productive ET pathways. This work highlights the complexity of charge transfer pathways in photochemistry with CdS QDs, and that QD characteristics other than size play a significant role in CdS QD-CaI interactions.

2.2. Introduction

Coupling redox enzymes with colloidal semiconductor nanocrystals allows the opportunity to drive multielectron chemistry with light, using the tunability of semiconductor nanocrystal material properties as a powerful handle to control light-induced electron transfer to the enzyme and resulting catalytic output.[1,2] Nanocrystal size, for example, can be modulated to tune the driving force for photoexcited electron transfer (ET) to an enzyme acceptor, as the quantum confinement nature of semiconductor nanocrystals causes the band gap energy to increase with decreasing particle size.[3,4] Nanocrystal size and shape may also play a role in the binding affinity and orientation of the nanocrystal to the enzyme surface.

Previous work on CdS nanorods coupled with a H_2 producing enzyme, [FeFe]-hydrogenase I from *Clostridium acetobutylicum* (CaI), demonstrated that capping the nanocrystal surface with negatively charged mercaptopropionate ligands allows for an electrostatic interaction with a positively charged patch on the CaI surface in biomimicry of the binding of the native CaI redox partner ferredoxin.[5,6] From this binding site, evidence supports that the photoexcited nanocrystal injects electrons into the distal [4Fe-4S] cluster of CaI (**Figure 2.1**), followed by intraprotein electron transport through a further series of FeS clusters to reach the CaI catalytic active site where proton reduction occurs to produce H_2.[5–7] Photoexcited holes are scavenged by ascorbate ($AscH^-$), a sacrificial electron donor.

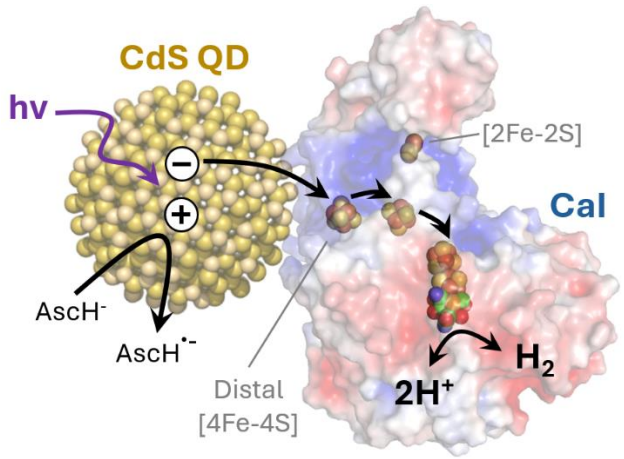

Figure 2.1: Proposed scheme of photochemical H_2 production in CdS QD-CaI complexes. CdS QDs capped with negatively charged mercaptopropionate ligands (not pictured) are proposed to bind electrostatically with the positively charged (blue) patch of the CaI surface near the distal [4Fe-4S] cluster into which photoexcited electrons are transferred from the QD. Intraprotein ET occurs through a series of further FeS clusters to the active site where the interconversion of protons into H_2 gas occurs, while photoexcited holes left behind in the QD are scavenged by ascorbate ($AscH^-$). A [2Fe-2S] cluster lies near the surface of a second, smaller positively charged patch of the CaI surface. This cluster is hypothesized to play a role in modulating the electronic environment of neighboring clusters, but it is not thought to be involved in electron transport itself.

One of the other FeS clusters in CaI, a [2Fe-2S] cluster, also lies near the enzyme surface in the vicinity of a smaller positively charged surface patch of CaI. It has been proposed that the [2Fe-2S] cluster is not an active participant in the CaI intraprotein electron transport chain, but rather serves a role in modulating the electronic properties of neighboring clusters.[7] Electron paramagnetic resonance experiments on photochemical reduction of CaI by CdSe quantum dots (QDs) demonstrated a rise in signal primarily from the reduced [4Fe-4S] cluster, but also possible features of [2Fe-2S] reduction, raising the question of whether QDs might bind to and carry out ET to this CaI surface site as well.[8] However, the extent to which this ET pathway may occur in QD-CaI complexes and the impact it would have on photochemical H_2 production is unknown. There is also still much that remains to be understood generally about the role that varying QD size may play in the rate constant of ET and binding affinity to CaI.

In this work, we investigate the role of QD size in controlling the interfacial ET step to CaI and the resulting photochemical H_2 production using a size series of CdS QDs 3.3, 4.3, 4.5, 5.0 and 5.3 nm in diameter. We measured the CaI-induced changes in the QD excited state decay kinetics with transient absorption (TA) spectroscopy. The CaI-induced decay kinetics were analyzed with a binomial model for the distribution of CaI bound per QD (N_{CaI}) to extract rate constants of ET and average number of CaI bound ($\langle N_{CaI} \rangle$). We found that in QD sizes 3.3 to 4.5 nm, two decay processes were necessary to fit the CaI-induced decay, a ~10^8 s^{-1} and a faster ~10^{10} s^{-1} decay. While the data may indicate an upper QD size cutoffs for the presence of the faster ~10^{10} s^{-1} process, in the QDs where the processes were present neither $\langle N_{CaI} \rangle$ nor the rate constants trended in a QD size dependent manner. Rather, QD properties other than size appear to modulate $\langle N_{CaI} \rangle$ here. We measured photochemical H_2 production in three of these QD sizes with CaI, finding that the quantum yield (QY) did not trend with the quantum efficiency of ET (QEET) as calculated from the CaI-induced excited state lifetime shortening of the QDs. This may indicate that some QDs differ greatly in other aspects of the photochemical system, such as the efficiency of the hole scavenger or back-electron transfer processes, or that not all of the observed excited state lifetime shortening is a result of ET processes that contribute towards H_2 production.

2.2 Experimental Methods

2.2.1 Hydrogenase Expression, Purification, and Characterization

The CaI hydrogenase expression and purification were carried out using an adaptation of a previously described method.[9] The protein was expressed heterologously in E. coli (BL21(DE3) ΔiscR cell line). Inoculation of cultures was carried out with fresh transformants and grown overnight in terrific broth (TB) media with 0.4% glycerol, at 37 °C, 250 rpm for 15 h. In a 2 L flask, 1 L of TB was inoculated with 10 mL of overnight culture, which was then grown to an

A600 of 0.22 to 0.35. For induction, the following components were added for final concentrations of 1.5 mM IPTG, 2 mM cysteine, 4 mM ferric ammonium citrate, 25 mM fumarate, and 0.5% glucose. Two 1 L cultures were mixed together into a 2 L narrow-neck flask and sparged under Argon gas overnight. All further steps were carried out anaerobically. For harvesting, cells were centrifuged 7 min at 7000 rpm, resuspended in 100 mM Tris, 300 mM NaCl, pH 8.3, 5% glycerol, and 2 mM NaDT and stored at −80 °C. In preparation for purification, cells were thawed and mixed with Roche EDTA-free protease inhibitor, DNAse, and lysozyme. Cells were lysed by passing through a microfluidizer 8 to 10x and lysed cells were then spun for 1 h at 45,000 rpm. The clarified lysate was passed over an IBA column of preequilibrated XT-HC Strep, washed, and eluted with a storage buffer with 20 mM XT 4Flow biotin in 50 mM Tris, 200 mM NaCl, 5% glycerol, 5 mM NaDT pH 8. The CaI was stored anaerobically at 4 °C in an MBraun glovebox until use. SDS-PAGE confirmed CaI expression and purity, and a Bradford assay measured CaI concentration. A methyl viologen dye-based assay measured CaI H_2 production activity.

2.2.2 CdS QD Synthesis and Ligand Exchange

The 3.3 nm CdS QDs were synthesized with a single-injection procedure documented in Chapter 5, in which the same QD batch was used.[10,11] The 4.3 to 5.3 nm CdS QDs were synthesized with a multi-injection procedure described in prior publications, and the 4.5 and 5.0 nm QD batches were also used in experiments described in Chapters 3 and 5, respectively.[10,12] The multi-injection synthesis was performed under inert atmosphere with an argon-filled Schlenk line and purification was carried out in an argon atmosphere MBraun glovebox. Sulfur precursor consisted of 0.025 g sulfur (99.998%) in 5.529 g 1-octadecene (technical grade, 90%) for a 0.1 M solution which was left to dissolve overnight. Cadmium oleate precursor (0.1 M) was made in a 3-necked round bottom flask with a reflux condenser; the precursor starting materials consisted of 0.131 g cadmium oxide

(99.99%), 2.83 oleic acid (90%), and 5.43 g 1-octadecene, which were evacuated at 90°C for 30 minutes. Under argon atmosphere, the precursor was then heated to 250°C. After the precursor solution turned clear, it was cooled to 60°C in preparation for later injections. Meanwhile, the synthesis reaction mixture was set up in a second flask with reflux condenser, to which 2.38 g 1-octadecene was added and evacuated for 30 min at 90°C. Next, 4 mL of cadmium-oleate precursor solution was transferred to the synthesis reaction flask, which was then heated to 260°C, followed by a 2 mL injection of 0.1 M sulfur precursor. The reaction mixture temperature was kept at 220°C for the injections remaining. The first sulfur injection was followed three minutes later by 0.5 mL of cadmium oleate precursor. Thereafter, injections were spaced 1 minute apart, alternating sulfur and cadmium oleate injections. Aliquots were taken in-between injections and their UV-vis absorbance spectrum measured, and injections were halted when the desired band edge peak wavelength was achieved. After the last injection, the mixture was left to grow at 220°C for one more minute prior to quenching in a mineral oil bath to cool the solution. Once cooled to a safe handling temperature <70°C, the reaction solution was placed in an argon-filled rubber septum-capped vial and transferred into an argon atmosphere glovebox for the purification procedure.

The CdS QD purification was carried out as follows: the initial post-synthesis QD solution was precipitated using a 1:3 v/v mixture of methanol:isopropanol and centrifuged. The supernatant was removed, leaving a gel-like QD pellet. The pellet was redissolved in ~1 mL toluene, precipitated with methanol, and centrifuged. The clear supernatant was removed, and the solid QD pellet was redissolved in ~4 mL hexanes, precipitated with a 1:3 v/v mixture of methanol:isopropanol, and centrifuged. The clear supernatant was removed, the solid QD pellet was placed under vacuum to evaporate the remaining solvent, followed by redispersal in ~1 mL toluene. The QD average diameters were determined from previously established calibration

curves based on the first exciton peak wavelength of the absorbance spectrum (**Table 2.2.1**). The first exciton peak absorbance and molar absorptivity were used to determine QD stock concentrations.[13]

Table 2.2.1: CdS QD diameters and other sample designations, band-edge peak wavelengths, and pump wavelengths used in TA experiments.

QD Diameter[13] (nm)	Band Edge Wavelength (nm)	TA Pump Wavelengths (nm)
3.3	396	342
4.3 (#1)	427	342
4.3 (#2)	427	358
4.5	432	358
5.0 (LE-a)	443	380
5.0 (LE-b)	443	378
5.3	450	380

The CdS QD ligand exchanges to 3-mercaptopropionate surface capping ligands were carried out adapted from previously described methods.[14,15] A 71 mM 3-mercaptopropionic acid solution was made with 0.143 g of 3-mercaptopropionic acid (99%), 15.0 g of methanol, and 0.448 g of tetramethylammonium hydroxide (>97%) for adjustment to pH 11. For each CdS QD stock synthesized, the native ligand-capped CdS QDs in toluene were precipitated with methanol, and the mercaptopropionic acid solution was added until the QD solution became optically clear. The ligand exchanged QDs were precipitated with toluene, centrifuged, the colorless supernatant discarded, and the pellet of mercaptopropionate-capped CdS QDs was dried and redissolved in Milli-Q water.

2.2.3 Transient Absorption Spectroscopy

This TA data collection setup has been described previously.[16] The instrumentation consists of a Spectra-Physics Solstice regeneratively amplified Ti:sapphire laser (1 kHz, 800 nm, 3.5 mJ/pulse, 100 fs), a Light Conversion TOPAS-C optical parametric amplifier, an Ultrafast

Systems HELIOS spectrometer for the time window 150 fs – 3 ns, and an Ultrafast Systems EOS spectrometer for the time window 0.3 ns – 400 μs. CdS QD-CaI samples were run under rigorous air-free conditions in 2 mm quartz cuvettes fitted with a Kontes valve in 12.5 mM Tris buffer at pH 7. The CdS QD concentrations were 2 μM, with the exception of the 3.3 nm QD run at 3.5 μM to increase signal quality. Samples with CdS QDs and CaI were mixed at the molar ratios as noted in the text. A magnetic stir bar was used for continuous stirring throughout data collection. Varying pump wavelengths were used as shown in **Table 2.1**, such that for each QD diameter, the pump energy did not approach resonant pumping with the band edge. Pump powers for each QD sample were selected such that the normalized excited state decays were independent of power, a sign of predominantly single excitons contributing to the signal. Experiments were carried out at room temperature, and absorption spectra taken at intervals during the experiment were used to monitor sample consistency.

2.2.4 Photochemical Hydrogen Production

Mixtures of CdS QDs and CaI at 1:1 QD:CaI ratios were prepared in 50 mM Tris, 5 mM NaCl, 5% glycerol, at pH 7, with 100 mM ascorbate as a hole scavenger. QD and CaI concentrations were at 590, 450, and 320 nM for the 4.3 (#2), 4.5, and 5.0 (LE-b) nm QD samples, respectively, such that all three QD samples had similar absorbance values of ~0.3 at 405 nm. Buffers were sparged under argon prior to use and sample preparation was carried out in an argon-filled MBraun anaerobic chamber. Assay samples prepared were 600 μL in 1.5 mL serum vials sealed with rubber septa. Sample vials were stirred and illuminated 10 min by a 405 nm continuous wave diode laser at 40 mW. After illumination, H_2 was detected by injecting a sample of the vial headspace into an Agilent 7820A gas chromatograph with a 5 Å molecular sieve column.

2.3. Results and Discussion

To investigate the impact of QD size on QD-CaI ET, we took transient absorption spectroscopy measurements on six CdS QDs with varying diameters of 3.3, 4.3, 4.5, 5.0, and 5.3 nm. We also compare two QDs from different batches which are of similar diameter (4.3 nm), but differing intrinsic excited state lifetimes, two QD samples from the same batch of 5.0 nm particles which was ligand exchanged to MPA on two separate occasions, and two batches of CaI stock.

2.3.1 Intrinsic CdS QD Photoexcited Electron Decays

First, we briefly describe the intrinsic QD excited state decays, so that we can address whether any differences between QDs in these properties appear relevant in the later discussion of CaI-induced decay processes (**Figure 2.1a**). We focus on the transient band-edge bleach feature of the CdS QD TA spectrum, which corresponds to the ensemble population of conduction band-edge electrons.[17–19] The excited state decay kinetics of cadmium chalcogenide QDs are complex and the underlying contributions to the kinetics are not yet well-characterized for the full femto- to microsecond time window. As such, here we take a generalized approach and characterize the intrinsic QD decays by their half-lives. The excited state half-lives of all but one of the QD samples lie in a similar range from 5 to 10 ns (**Figure 2.1b**). The longest-lived QD, the first of the two 4.3 nm particles, has a half-life of 18 ± 4 ns, visibly longer than that of the second 4.3 nm QD at 8.4 ± 0.5 ns. Of the two MPA ligand exchange batches of the 5.0 nm QDs, MPA LE-b is slightly longer than MPA LE-a with a half-life of 9.9 ± 0.6 ns versus 6.9 ± 2.6 ns, respectively. These differences may result from varying MPA ligand coverage affecting the number or distribution of surface-localized electron trap states, which serve as one of the pathways of decay of the conduction band electron in CdS nanocrystals.[20–23]

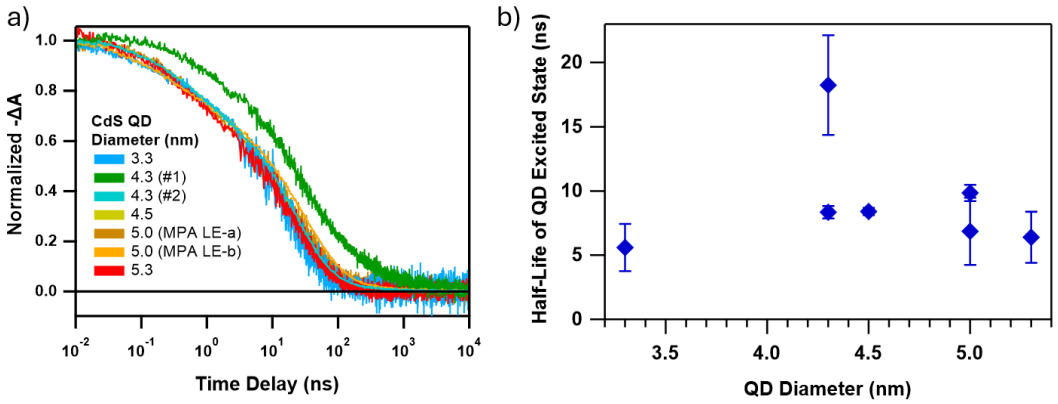

Figure 2.2: a) Excited state decays of the band-edge bleach feature of MPA-capped CdS QDs of varying diameter and **b)** their corresponding half-lives.

3.2 Excited State Decay Kinetics in CdS QD-CaI Complexes

To observe ET from CdS QDs to CaI, the QDs were mixed with CaI at a range of molar ratios. ET should result in lifetime shortening of the QD excited state decay; to analyze the potential ET kinetics we take the quotient as described by Eqn (1):

$$S_{CaI}(t) = \frac{S_{QD-CaI}(t)}{S_{QD}(t)} \tag{1}$$

where $S_{CaI}(t)$ represents the QD excited state decay caused by the addition of CaI, and $S_{QD}(t)$ and $S_{QD-CaI}(t)$ the excited state decays of the QD-only and QD-CaI sample, respectively. **Figure 2.2** shows $S_{CaI}(t)$ for a selection of the data from QD-CaI data taken with QDs of diameters 3.3 to 5.3 nm. Previous work on CdS nanorod-CaI complexes has demonstrated that the number of CaI bound per nanorod can by modeled by a Poisson distribution; given the much more limited surface area of QDs compared to nanorods, we propose that a binomial distribution—which accounts for a limited number of binding sites (N_{max})—is a more appropriate model for the distribution in the number of CaI bound per QD (N_{CaI}), described by an average number bound, $\langle N_{CaI} \rangle$.[5,24–26] Averaging over the distribution of N_{CaI},[26] we may model an QD-CaI ET pathway with rate constant k and normalization factor A using Eqn (2):

$$S_{CaI}(t) = A \cdot \left(1 + \frac{\langle N_{CaI} \rangle}{N_{max}} (e^{-kt} - 1)\right)^{N_{max}} . \quad (2)$$

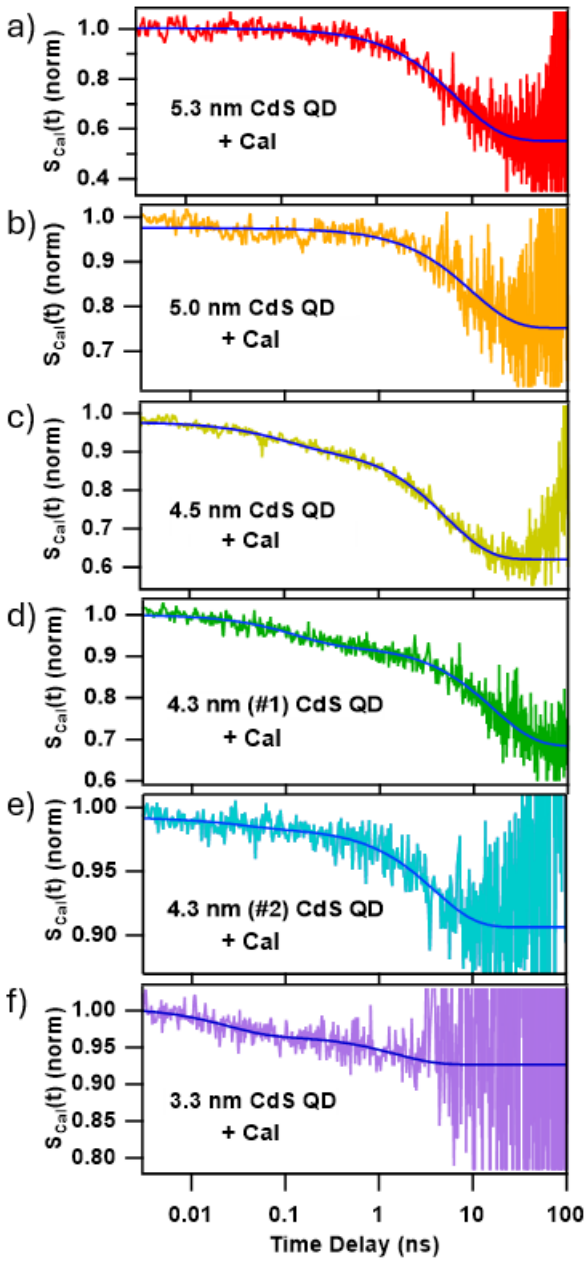

Figure 2.3: Excited state decay kinetics caused by the interaction of CaI with CdS QD ($S_{CaI}(t)$), obtained by taking the quotient of the QD-CaI and QD-only band-edge bleach decay traces for QD diameters **a)** 5.3 nm, **b)** 5.0 nm (MPA LE-a), **c)** 4.5 nm, **d)** 4.3 nm from synthesis batch #1, **e)** 4.3 nm from synthesis batch #2, and **f)** 3.3 nm. The solid dark blue lines correspond to fits to Eqn (2) for QD sizes 5.3 and 5.0, and to Eqn (3) for sizes 4.5, 4.3, 3.3 nm

We find that $S_{CaI}(t)$ of the largest QDs of diameters 5.3 and 5.0 nm can be fit reasonably well to Eqn (2), with similar k values ranging from 1.0 to 1.8 x 10^8 s^{-1} (**Figure 2.2a**, **b**, **Table 2.2**). In all fits, where multiple QD:CaI molar ratios were available, a global fit was performed such that k was set as a linked parameter while $\langle N_{CaI} \rangle$ was allowed to vary between QD:CaI ratios. The value of N_{max} does not have a strong impact on the fit—for $N_{max} \geq 1$, the variation in the other fit parameters was negligible, likely a result of the low $\langle N_{CaI} \rangle$ of these samples, whose highest value was 0.51 ± 0.01 for the 3:1 QD:CaI ratio of the 5.3 nm QD. For the smaller sizes 3.3, 4.3, and 4.5 nm, however, Eqn (2) is not sufficient to describe the $S_{CaI}(t)$ kinetics due to the presence of an additional decay occurring at faster times <1 ns.

To fit the full time window of $S_{CaI}(t)$ behavior from the picosecond to tens of nanosecond range in the 3.3 to 4.5 nm QDs, we consider whether QD-CaI binding may involve more than one distinct binding orientation of the QD on the CaI surface, with its own separate k and $\langle N_{CaI} \rangle$. Adding another ET pathway with a binomial distribution of N_{CaI} results in Eqn (3):

$$S_{CaI}(t) = A \cdot \left(1 + \frac{\langle N_{CaI} \rangle_1}{N_{max}} (e^{-k_1 t} - 1)\right)^{N_{max}} \left(1 + \frac{\langle N_{CaI} \rangle_2}{N_{max}} (e^{-k_2 t} - 1)\right)^{N_{max}}. \quad (3)$$

Eqn (3) assumes the same N_{max} for both QD-CaI binding orientations, as the number of available binding sites on the QD is unlikely to change drastically with CaI orientation, and the fits to the data with Eqn (2) already showed that N_{max} has minimal impact on the fit since the relative concentration of CaI is low.

Eqn (3) fits well to the $S_{CaI}(t)$ decay traces of the 3.3 to 4.5 nm QDs (**Figure 2.2c-e**). The fits result in a k_1 in the same 10^8 s^{-1} order of magnitude to the k values found for the 5.0 and 5.3 nm QDs (**Table 2.2**). It should be noted that the fit results from the 3.3 nm QD kinetics have a much greater uncertainty, because of particularly low signal-to-noise at late times which prevents fitting the kinetics > 3 ns. Compared to the fit results from the other QDs, the value of k_1 for the

4.3 nm #1 is somewhat lower at 0.6 x 10^8 s^{-1}. This may be related to the fact that this was the QD with the longer intrinsic excited state lifetime (**Figure 2.1**), as this allowed for better signal to noise of $S_{CaI}(t)$ at later delay times >30 ns and therefore to be fit to a wider time window than was possible for the other QDs. The fit of Eqn (3) to the 3.3 to 4.5 nm QDs is also able to describe the faster decay component with the value of k_2 ranging from 0.8 to 4.1 10^{10} s^{-1} (**Table 2**).

Table 2.2: Rate constants of $S_{CaI}(t)$ decay kinetics.

QD Diameter (nm)	k_1 (10^8 s^{-1})	k_2 (10^{10} s^{-1})
5.3	**1.3** ± 0.06	-
5.0 (LE-a)	**1.0** ± 0.1	-
5.0 (LE-b)	**1.8** ± 0.4	-
4.5	**1.8** ± 0.1	**1.3** ± 0.4
4.3 (#1)	**0.6** ± 0.05	**0.8** ± 0.2
4.3 (#2)	**2.5** ± 0.3	**3.1** ± 2.5
3.3	**6.6** ± 4.5	**4.1** ± 1.0

Overall, the fit results of the $S_{CaI}(t)$ kinetics indicate two excited state decay processes induced by CaI, with rate constants k_1 ~10^8 and k_2 ~10^{10} s^{-1}. The values of k_1 and k_2 do not appear to be QD size dependent (**Figure 2.3a**). The 10^8 s^{-1} process appears to be present in all the QDs tested, though with higher uncertainty in the 3.3 nm QD due to low signal-to-noise ratio. The 10^{10} s^{-1} decay, meanwhile, only appears in the smaller end of the QD size range 3.3 to 4.5 nm. (**Figure 2.3a**).

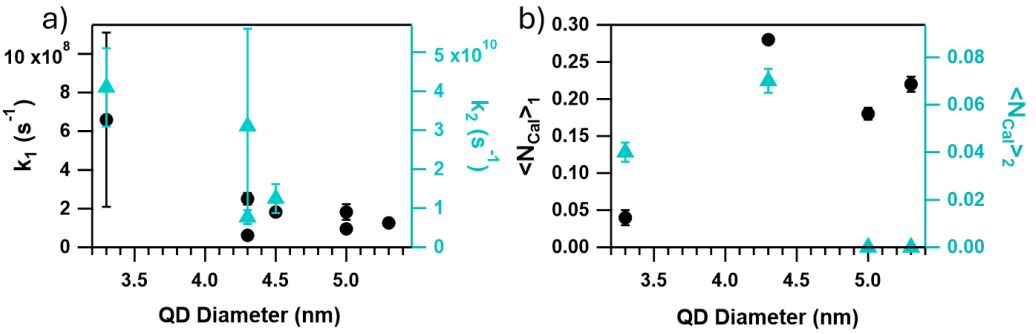

Figure 2.4: a) Rate constants k_1 (black circles) and k_2 (teal triangles) of $S_{CaI}(t)$ decay versus QD diameter, b) $\langle N_{CaI}\rangle_1$ and $\langle N_{CaI}\rangle_2$ versus QD diameter at a 6:1 QD:CaI ratio with CaI batch #1.

To observe trends in QD-CaI binding, we look to the $\langle N_{CaI} \rangle$ fit parameter. The resulting $\langle N_{CaI} \rangle$ values for each QD and QD:CaI ratio are listed in **Table 2.3**. As two different batches of CaI were used in this data set, to examine trends in $\langle N_{CaI} \rangle$ we will compare only data which was taken at the same QD:CaI ratio and with the same CaI batch, as there may be differences in the iron-sulfur cluster loading and therefore the fraction of CaI capable of accepting electrons. First, **Figure 2.3b** shows the trends for $\langle N_{CaI} \rangle_1$ and $\langle N_{CaI} \rangle_2$ at a 6:1 QD:CaI ratio for CaI batch #1. In this data set, $\langle N_{CaI} \rangle_1$ is distinctly lower for the 3.3 nm compared to the 4.3 to 5.3 nm QDs, which do not appear to follow a clear trend with QD size. $\langle N_{CaI} \rangle_2$, meanwhile, is higher with the 4.3 nm than the 3.3 nm, though with only two data points we cannot determine whether this is due to QD size or other factors.

Table 2.3: $\langle N_{CaI} \rangle$ values from kinetic fits to $S_{CaI}(t)$ kinetics.

QD Diameter (nm)	CaI Batch	QD:CaI Ratio	$\langle N_{CaI} \rangle_1$	$\langle N_{CaI} \rangle_2$
3.3	#1	6:1	**0.04** ± 0.01	**0.04** ± 0.004
4.3 (#1)	#1	10:1	**0.22** ± 0.006	**0.05** ± 0.006
4.3 (#1)	#1	6:1	**0.28** ± 0.004	**0.07** ± 0.05
5.0 (LE-a)	#1	6:1	**0.18** ± 0.008	-
5.0 (LE-a)	#1	3:1	**0.25** ± 0.008	-
5.3	#1	6:1	**0.22** ± 0.01	-
5.3	#1	3:1	**0.51** ± 0.01	-
4.3 (#2)	#2	3:1	**0.08** ± 0.004	**0.008** ± 0.003
4.5	#2	2:1	**0.21** ± 0.005	**0.05** ± 0.005
4.5	#2	1:1	**0.35** ± 0.003	**0.07** ± 0.003
5.0 (LE-b)	#2	3:1	**0.04** ± 0.001	-
5.0 (LE-b)	#2	1:1	**0.11** ± 0.001	-

In the data taken on CaI batch #2, there is no single ratio at which data on all three QD sizes was obtained (**Table 2.3**). Nevertheless, a notable result can be seen in that the 4.5 nm QD has significantly higher $\langle N_{CaI} \rangle$ values than the other QDs with CaI batch #2. While the 4.3 and 5.0

nm QD have comparable $\langle N_{CaI} \rangle_1$ (3:1 QD:CaI) the 4.5 nm QD has a markedly higher $\langle N_{CaI} \rangle_1$ at 0.35, over 3x higher than 0.11 for the 5.0 nm QD (1:1 QD:CaI). This is different from the trend seen with the CaI batch #1 data from **Figure 2.3b**, in which $\langle N_{CaI} \rangle_1$ for the QDs in the 4.3 to 5.3 nm range did not vary to the same extent. From these comparisons from both CaI batches, it does appear that some characteristic of the QD other than size alone has an impact on the strength of QD-CpII binding.

2.3.4 Photochemical H_2 Production with Varying CdS QD Size

We measured photochemical H_2 production from three of the above QDs, 4.3 nm (#2), 4.5 nm, and 5.0 nm (LE-b). All three QD sizes were run at a 1:1 QD:CaI ratio, under the same illumination conditions with a 405 nm continuous wave diode laser in the presence of a sacrificial hole scavenger, ascorbate. Illumination of QDs in the absence of CaI did not produce any detectable H_2. **Figure 2.4** shows the relative QY, obtained by dividing the QY of each sample by that of the 4.3 nm QD sample. The 4.3 nm and 5.0 nm QD-CaI samples produced similar QY within error of each other, followed by the 4.5 nm QD whose QY was more than 4x lower.

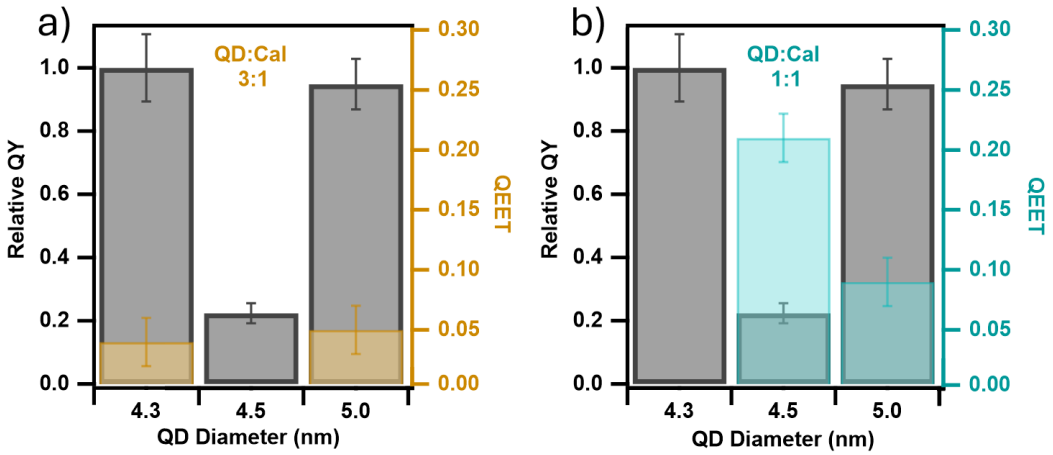

Figure 2.5: Relative QY of photochemical H_2 production from CdS QD-CaI samples from three QD sizes, compared to the trends in QEET (as calculated using Eqn (4)) at QD:CaI ratios of **a)** 3:1 and **b)** 1:1, for the QD sizes at which TA data was taken at those ratios.

We use an established method to calculate the quantum efficiency of ET (QEET)—defined as the percentage of photoexcited electrons in the sample which undergo ET to CaI instead of decaying through other pathways such as electron-hole recombination or localization to surface trap sites on the QD—from the TA decay traces directly.[26] Under the assumption that the QD excited state lifetime shortening caused by the addition of CaI is attributed to ET, we calculate QEET following Eqn (4):

$$QEET = 1 - \int_0^\infty dt \left(-\frac{dS_{QD}(t)}{dt}\right)\left(\frac{S_{QD-CaI}(t)}{S_{QD}(t)}\right) \quad (4)$$

Figure 2.4a shows the QEET values at a QD:CaI ratio 3:1 for the 4.3 and 5.0 nm, and **Figure 2.4b** for the QD:CaI ratio of 1:1 for the 4.5 and 5.0 nm, compared with the relative QY for each QD size. From the 3:1 ratio in **Figure 2.4a**, we see that the 4.3 and 5.0 nm QDs have similar QEET, and their resulting QY are similar to each other, as we might expect. However, from the 1:1 ratio in **Figure 2.4b** we see that while the 4.5 nm sample QEET is over 2x higher than that of the 5.0 nm QD, its QY is over 4x lower than the 5.0 nm sample.

How could the QD-CaI sample with the highest QEET have the lowest QY of H_2 production? There are several possible causes of this result. One possibility is that the rate of hole transfer to the ascorbate varies with different QDs, possibly due to a difference in surface faceting or surface ligand coverage; if the 4.5 nm QD is experiencing a lower hole transfer rate, this would correspondingly lower the QY even if the QEET is larger than that of the other QD sizes. A second possibility is a differing rate of back-electron transfer between different QDs, which would similarly cause QY to no longer trend with QEET. The third possibility is that the fundamental assumption of our QEET calculation—that all of the excited state lifetime shortening induced by CaI is the result of ET—is incorrect. Given that we observe two separate decay processes in

$S_{CaI}(t)$, perhaps one of these processes is not an ET pathway—or at least, not an ET pathway productive for catalysis.

For example, if the addition of CaI modulates the QD surface in such a way that the rate or amount of electron trapping is increased, this would manifest in excited state lifetime shortening in the same manner as ET. Alternatively, if one of the two $S_{CaI}(t)$ decay pathways represents QD binding the alternate positively charged CaI surface patch and ET to the [2Fe-2S] cluster, this may simply not be an ET pathway which contributes to catalysis, particularly since prior work has hypothesized that the [2Fe-2S] cluster is not a direct participant in the ferredoxin-driven electron transport chain of CaI.[7]

If this is the case, then which of the two $S_{CaI}(t)$ decays might represent the catalysis-productive ET process? Given that the 5.0 nm QD-CaI sample demonstrated photochemical H_2 production but did not show any indication of the k_2 ~10^{10} s^{-1} decay process (**Table 2.2**, **Figure 2.3**), it seems likely that the k_1 ~10^8 s^{-1} decay process represents the catalysis-productive ET process. This would also track with past work with CdS nanorod-CaI samples, which measured rate constants of ET on similar timescales of 10^7 to 10^8 s^{-1}.[6,24–26] The apparent absence of a QD size dependence of the value of k_1 is interesting, as it implies that neither the driving force for ET, nor the nanocrystal size alone have a strong impact on the rate constant of ET—at least in the CdS QD size range from 3.3 to 5.3 nm. Prior studies of ET in CdTe QD-CaI complexes reached a similar conclusion, proposing that the presence of proton-coupled ET may result in the lack of a driving force dependence. However, the fact that we do see large deviations in $\langle N_{CaI} \rangle$ for select QDs—the significantly lower $\langle N_{CaI} \rangle$ with the 3.3 nm QD, and the markedly higher $\langle N_{CaI} \rangle$ with the 4.5 nm—suggests that some quality of the QDs other than size does play a large role in QD-CaI interaction. Differences in QD surface properties are a likely culprit, such as the distribution of

facets and ligand coverage, impacting the strength and nature of the QD-CaI binding. Further understanding of QD characteristics related to surface structure could be key to tuning nanocrystal-hydrogenase interaction.

2.4. Summary and Conclusions

In this work, we examined interfacial ET and photochemical H_2 production in CdS QD-CaI complexes in a range of QD diameters from 3.3 to 5.3 nm. We found that all the QDs sizes showed a CaI-induced excited state decay process with rate constant k_1 ~10^8 s^{-1}, and QDs with diameters 3.3 to 4.5 nm showed an additional, faster process with rate constant k_2 ~10^{10} s^{-1}. $\langle N_{CaI} \rangle$ did vary for select QDs, showing that factors other than QD size play an important role in QD-CaI binding affinity. $\langle N_{CaI} \rangle$ did vary for select QDs, but also did not appear to trend with QD size, demonstrating that QD properties other than size play an important role in QD-CaI binding affinity. We measured photochemical H_2 production in QD-CaI samples with three QD sizes, finding that the QD with the largest calculated QEET resulted in the lowest QY of H_2 production. This may be an indication of differences in hole or back-electron transfer between this and the other two QDs, or that not all of the CaI-induced excited state lifetime shortening is associated with a catalysis-productive ET pathway. If this is the case, we find that the catalytically-productive ET pathway is likely associated with k_1 ~10^8 s-1 decay process, while the k_2 ~10^{10} s^{-1} decay may be the result of either an CaI-induced change to the intrinsic QD excited state decay, or a separate QD-CaI binding orientation leading to an unproductive ET pathway; in either case, the ~10^{10} s^{-1} decay is not present in CdS QD sizes ≥ 5.0 nm. Overall, we find that CdS QD properties other than size—such as differences in surface faceting and ligand passivation—are a powerful factor in determining the nature of QD-CaI binding, and that more work is needed to understand the processes contributing to the excited state lifetime shortening of CdS QDs induced by CaI.

2.5. Future Work and Outlook

An emerging future opportunity for this work will be to incorporate independent measurements of QD-CaI binding, as well as kinetic Monte Carlo simulation to probe the factors contributing to the differences in H_2 production QY between CdS QD-CaI samples. Microscale thermophoresis (MST) is a technique which has been used to quantify the strength and cooperativity of protein-protein binding interactions using fluorescent-tagging. Recent work has established the use of this method for characterizing electrostatic CdS QD-nitrogenase enzyme binding interactions, demonstrating the promise of MST as a measure of QD-enzyme binding which does not rely on interpretation of ET and photochemical product formation. Correlating QD-CaI MST with the results from TA spectroscopy and photochemical H_2 production experiments will enable us to begin piecing together how QD-CaI binding properties contribute to observed differences in H_2 production.

To investigate how differences in other pathways in the photochemical system play a role, a promising avenue is the use of kinetic Monte Carlo simulations of QD-CaI H_2 production, which we have already developed for CdS nanorod-CaI studies as will be discussed in Chapter 4. For example, if the k_2 ~10^{10} s^{-1} CaI-induced decay pathway observed in TA experiments is a non-catalytically productive ET pathway, using the rate constants obtained from TA data fits and QD-CaI binding information from MST as inputs, we can simulate this possibility and observe whether this or other hypotheses are capable of explaining the experimental trends.

Finally, knowing that the QD surface likely plays a significant role in QD-CaI interactions, it would be insightful to test the impact of different post-synthesis QD treatments on QD-CaI binding, ET, and H_2 production. Prior work has shown that successive precipitation of Cd chalcogenide nanocrystals with methanol modifies the nanocrystal surface stoichiometry.

Differences in the MPA ligand exchange procedure are also capable of producing changes to QD surface ligand passivation, as demonstrated by the slight differences in excited state decay kinetics seen in our two 5.0 nm CdS QDs in **Figure 2.1**. Such experiments could shed light on the extent to which post-synthetic handling of CdS QDs impacts binding, ET, and catalysis in these systems, and lead to better understanding of how their interactions with external components could be better controlled.

Chapter 3
Kinetics of Redox Intermediates of a [FeFe]-Hydrogenase Photoreduced by CdS Quantum Dots

3.1. Abstract

Protein structure and cofactor properties are key to the control of electron transfer (ET) and catalytic bias in redox enzymes. We examine these factors in [FeFe] hydrogenase II from *Clostridium pasteurianum* (CpII), which catalyzes the reversible activation of H_2 with large bias toward H_2 oxidation. CpII is a metalloprotein consisting of two iron-sulfur clusters (F-clusters) which enable ET to and from the active site (H-cluster). We photoreduce CpII via coupling with colloidal cadmium sulfide quantum dots (CdS QDs), measuring the change in CpII redox species as a function of illumination time with electron paramagnetic resonance (EPR) spectroscopy. Through kinetic modeling of the photochemical EPR data we extract relative rate constants of ET between the metalloclusters. We find the results support a pathway of photoexcited ET from the QD into CpII through the distal F-cluster, in the same manner as the native ferredoxin redox partner. The resulting relative ET rates between clusters suggest highly directional electron flow, such that ET away from the H-cluster toward the proximal F-cluster is strongly favored by three orders of magnitude. This relative rate resembles the previously measured magnitude of CpII catalytic bias for H_2 oxidation, and supports the prior proposed model for the thermodynamic landscape of the intraprotein CpII ET pathway. We also detect signal resembling the two-electron reduced H_{sred} H-cluster state; the favored stabilization of H_{sred} over H_{hyd} may be another key element in the catalytic bias of CpII toward H_2 oxidation.

3.2. Introduction

Hydrogenase enzymes are essential biological catalysts for H_2 oxidation and proton reduction, comprising a family of enzymes with a wide range in catalytic bias.[1,2] An ongoing area of interest lies in how protein structure controls this bias, and how the underlying principles learned from these systems may be applied to the control of electron transport in increasingly complex redox chemistries.[3–7] The H_2 activation reaction in [FeFe]-hydrogenases is catalyzed at a metallocluster known as the H-cluster; electrons can be funneled to and from the H-cluster via a series of iron sulfur clusters (F-clusters), which in turn are oxidized or reduced by external redox shuttles such as a ferredoxin protein.[7–9] The structural, thermodynamic, and electronic properties of these clusters are all key to the resulting rate and directionality of intraprotein electron flow.[7,8]

Our hydrogenase of interest in this work is [FeFe]-hydrogenase II from *Clostridium pasteurianum* (CpII), which consists of an H-cluster and two F-clusters in its electron transport chain (**Figure 3.1a**).[7,10,11] CpII is nearly 1000 fold biased towards H_2 oxidation, but how the F-cluster arrangement and thermodynamic and electronic properties impact this catalytic bias in CpII is still under investigation.[7,10] The F-clusters of CpII demonstrate significantly different reduction potentials, most recently measured as -406 mV $\pm$ 12 and -140 mV $\pm$ 18 *versus* NHE.[10,11] Recent work has demonstrated evidence of spin-spin coupling between the two F-clusters of CpII, and proposes that that the higher potential F-cluster is located proximal to the H-cluster.[10] This arrangement would favor the flow of electrons in the H_2 oxidation direction from H-cluster to the proximal F-cluster, with spin-spin coupling compensating for the otherwise thermodynamically unfavorable electron transfer from proximal to the lower potential distal F-cluster for eventual reduction of a ferredoxin. However, further work is required to confirm this thermodynamic landscape and F-cluster arrangement. In addition, little is known about the catalytic mechanism of

H_2 oxidation and reduction in CpII. **Figure 3.1b** provides an example of a [FeFe]-hydrogenase catalytic cycle and possible intermediates,[7] however higher reduced H-cluster states such as H_{sred} or H_{hyd} have yet to be definitively observed in CpII. Identification of the relevant H-cluster redox species could provide further insight addressing the question of whether the H-cluster of CpII is tuned for H_2 oxidation.

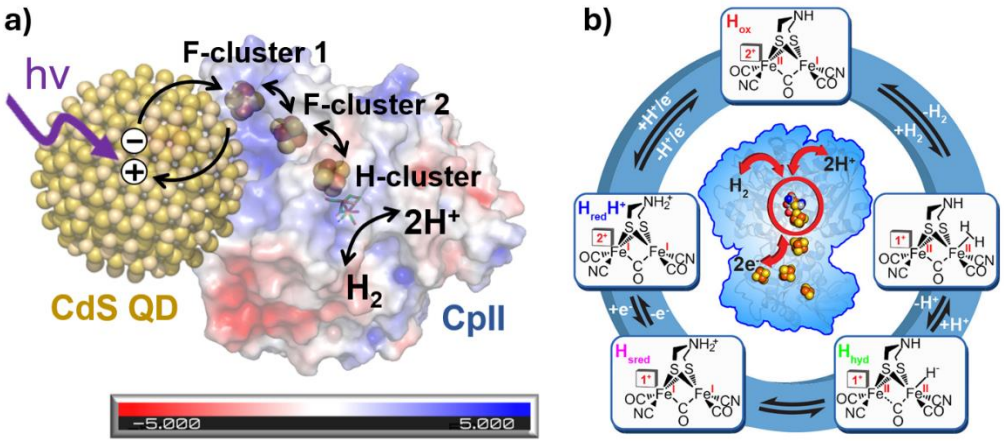

Figure 3.1: a) Scheme of CdS QD coupled to [FeFe]-hydrogenase CpII for photochemical H_2 production. **b)** One example of a proposed [FeFe] hydrogenase catalytic mechanism of H_2 production and oxidation occurring at the H-cluster active site and the cycle of H-cluster intermediates, reprinted with permission from Artz et al. J. Am. Chem. Soc. **2020**, 142, 3, 1227–1235, copyright © 2019 American Chemical Society. The reduced F-clusters, as well as several H-cluster intermediates (including H_{ox}, H_{sred}, and H_{hyd}) are EPR active.

In this work, we investigated the electron transfer pathways and redox intermediates of CpII by interfacing CpII with colloidal cadmium sulfide quantum dots (CdS QDs) to reduce the enzyme via the native electron injection pathway in a light-controlled manner. Previous work with other [FeFe] hydrogenases coupled with cadmium chalcogenide nanocrystals has shown that functionalization of the nanocrystal surface with negatively charged mercaptopropionate ligands allows for electrostatic binding to the hydrogenase in mimicry of the native ferredoxin-hydrogenase interaction.[12–14] Using this approach, we monitored the redox changes in the CpII F-clusters and H-cluster in the QD-CpII biohybrids as a function of illumination time with electron paramagnetic resonance (EPR) spectroscopy. We identified the relative light-dependent

accumulation and decay of the paramagnetic F- and H-cluster states by EPR-active signatures, developed a kinetic model of photoinduced electron transfer, and fit the model to the changes in EPR signals of redox species to extract relative rate constants of electron transfer between the metalloclusters. From these relative rates, we discuss the implications of the two different thermodynamic landscapes of the F-cluster relay, the catalytic mechanism of CpII, and how these results support previous proposed models of CpII electron transfer directionality.

3.3. Experimental Methods

3.3.1 [FeFe]-Hydrogenase Expression, Purification, and Characterization

The [FeFe]-hydrogenase CpII enzyme expression and purification were carried out as has been described previously.[7,10] Cultures were inoculated with fresh transformants and grown overnight in terrific broth (TB) media (all TB media used contained 0.4% glycerol), at 37 °C, 250 rpm for 14 to 16 h. In a 2 L flask, 1 L of TB media was inoculated with 10 mL of the overnight culture, which were then grown to an A600 of 0.22 to 0.35. For induction, the following components were added in sequence for final concentrations of: 1.5 mM IPTG, 2 mM cysteine, 4 mM ferric ammonium citrate, 25 mM fumarate, and 0.5% glucose. Two 1 L cultures were transferred into a 2 L Kimble Kimax narrow-neck flask and sparged with Argon gas overnight. Thereafter, all steps were carried out under anaerobic conditions. For harvesting, cells were centrifuged for 5 to 7 min at 6000 to 7000 rpm, resuspended in 100 mM Tris, 300 mM NaCl, pH 8.3, 5% glycerol, and 2 mM NaDT buffer and stored at −80 °C. In preparation for purification, cells were thawed and Roche EDTA-free protease inhibitor, lysozyme, and DNAse were added. Cells were lysed by passing through a microfluidizer 8 to 10x and lysed cells were then spun for 1 h at 45,000 rpm. The clarified lysate was passed over an IBA column of preequilibrated XT-HC Strep, washed, and then eluted with a 50 mM Tris, 300 mM NaCl, 5% glycerol, pH 8 storage buffer

containing 20 mM XT 4Flow biotin. Protein was stored at 4 °C in an MBraun anaerobic chamber until use. SDS-PAGE was used to confirm CpII expression and purification, and a Bradford assay was used to measure CpII concentration. A methyl viologen dye-based biochemical assay was used to measure the specific activity of H_2 production of purified CpII.

3.3.2 CdS QD Synthesis and Ligand Exchange

CdS QDs were synthesized with a multi-injection procedure described in prior work.[15] The synthesis was performed under inert atmosphere with an argon-filled Schlenk line and purification was carried out in an argon atmosphere MBraun glovebox. Sulfur precursor consisted of 0.025 g sulfur (99.998%) in 5.529 g 1-octadecene (technical grade, 90%) for a 0.1 M solution which was left to dissolve overnight. Cadmium oleate precursor (0.1 M) was made in a 3-necked round bottom flask with a reflux condenser; the precursor starting materials consisted of 0.131 g cadmium oxide (99.99%), 2.83 oleic acid (90%), and 5.43 g 1-octadecene, which were evacuated at 90°C for 30 minutes. Under argon atmosphere, the precursor was then heated to 250°C. After the precursor solution turned clear, it was cooled to 60°C in preparation for later injections. Meanwhile, the synthesis reaction mixture was set up in a second flask with reflux condenser, to which 2.38 g 1-octadecene was added and evacuated for 30 min at 90°C. Next, 4 mL of cadmium-oleate precursor solution was transferred to the synthesis reaction flask, which was then heated to 260°C, followed by a 2 mL injection of 0.1 M sulfur precursor. The reaction mixture temperature was kept at 220°C for the injections remaining. The first sulfur injection was followed three minutes later by 0.5 mL of cadmium oleate precursor, one minute later by 0.5 mL sulfur, one minute later by another 0.5 mL cadmium oleate, after which the mixture was left to grow at 220°C for one more minute prior to quenching in a mineral oil bath to cool the solution. Once cooled to a safe handling temperature

<70°C, the reaction solution was placed in an argon-filled rubber septum-capped vial and transferred into an argon atmosphere glovebox to for the purification procedure.

The CdS QD purification was carried out as follows: the initial post-synthesis QD solution was precipitated using a 1:3 v/v mixture of methanol:isopropanol and centrifuged. The supernatant was removed, leaving a gel-like QD pellet. The pellet was redissolved in ~1 mL toluene, precipitated with methanol, and centrifuged. The clear supernatant was removed, and the solid QD pellet was redissolved in ~4 mL hexanes, precipitated with a 1:3 v/v mixture of methanol:isopropanol, and centrifuged. The clear supernatant was removed, the solid QD pellet was placed under vacuum to evaporate the remaining solvent, followed by redispersal in ~1 mL toluene. The QD average diameter of 4.5 nm and molar absorptivity of 6.9×10^5 $M^{-1}cm^{-1}$ was determined from previously established calibration curves based on the 432 nm first exciton peak wavelength of the absorbance spectrum.[16] The first exciton peak absorbance and molar absorptivity were used to determine QD stock concentrations.

The CdS QD ligand exchange to 3-mercaptopropionate surface capping ligands was carried out using an adaptation of previously described methods.[17,18] A 71 mM 3-mercaptopropionic acid solution was made with 0.143 g of 3-mercaptopropionic acid (99%), 15.0 g of methanol, and 0.448 g of tetramethylammonium hydroxide (>97%) for adjustment to pH 11. First, the QDs were precipitated out of the toluene stock solution using methanol, and centrifuged. The clear supernatant was removed, and the solid QD pellet dried under vacuum then redispersed in 1 mL hexanes. 1 mL of the 71 mM 3-mercaptopropionic acid solution was added to the QD stock, mixed, and left to sit until phase separation occurred leaving a bottom layer of optically clear QD solution and a colorless top layer. The top layer was removed, toluene was used to precipitate the QDs, and

the solution was centrifuged. The colorless supernatant was removed, the QDs were dried under vacuum followed by redispersal in water.

3.3.3 Photochemical Hydrogen Production

Photochemical hydrogen production assays were used to assess the success of nanocrystal-hydrogenase coupling for photoreduction (**Figure 3.2**). Mixtures of CdS QDs (500 nM) and CpII (0, 250, 500, 2000 nM) were prepared in 50 mM Tris, 5 mM NaCl, 5% glycerol, at pH 7, with 100 mM ascorbate as a hole scavenger. Buffers were degassed under vacuum prior to use and sample preparation was carried out in an MBraun anaerobic chamber filled with N_2. Assay samples prepared were 600 µL in 1.5 mL serum vials sealed with rubber septa. Sample vials were stirred and illuminated 10 min by a 405 nm light emitting diode set to 8 mW. After illumination, H_2 was detected by injecting a sample of the vial headspace into an Agilent 7890A gas chromatograph with a 5 Å molecular sieve column.

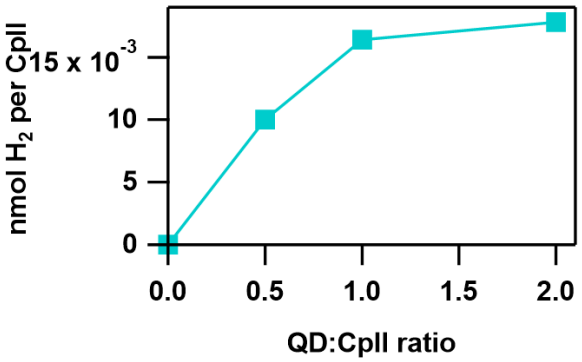

Figure 3.2: Photochemical H_2 production per CpII as a function of CdS QD:CpII ratio.

3.3.4 CdS QD-CpII EPR Sample Preparation

All samples were prepared under a N_2 atmosphere in an MBraun anaerobic chamber and all buffers were degassed under vacuum and transferred to the anaerobic chamber prior to use. Oxidized CpII was prepared by incubation of as-purified CpII for one minute in a 0.5 mM thionin acetate salt (≥ 85%) solution. The oxidized CpII was buffer exchanged into the final desired EPR

sample buffer contents and mixed with CdS QDs for final sample concentrations of 100 µM CdS QDs and 100 or 300 µM CpII in 50 mM Tris, 5% glycerol by volume, and 70 mM NaCl. The buffer exchange of oxidized CpII was carried out using a 30 kDa Millipore centrifugal filter for a minimum of six cycles at 9000 to 12,000 x g for 5 to 10 min each. CpII-only samples were prepared using the same procedure, but without the addition of CdS QDs. After being loaded into the EPR tube, a rubber septum was used to cap the sample which was then transferred out of the anaerobic chamber and frozen immediately in liquid nitrogen. Once frozen, samples were stored uncapped in the dark in a liquid nitrogen dewar while not in use.

3.3.5 CdS QD-CpII Sample Illumination and EPR Spectroscopy

Steady state illumination of samples was carried out in a Thor Labs integrating sphere fitted with two Thor Labs 1 W, 405 nm light emitting diodes and a Bruker liquid nitrogen cryostat (ER 4131 VT). Calibration of the cryostat temperature was carried out using a thermocouple probe placed inside a buffer solution. The EPR sample was placed in the sphere and allowed one minute to equilibrate to the set temperature of 233K in the dark and then illuminated at 405 nm, 2 W for the desired time interval. After each illumination period, the sample was immediately removed from the sphere, placed in liquid nitrogen, and then transferred to the EPR spectrometer for data collection at that illumination time point. The illumination and EPR data collection procedure was repeated to obtain the illumination time dependent spectra. EPR spectra (continuous wave, X-band—9.38 GHz) were acquired using a Bruker Elexsys E-500 with a super high-Q resonator, ColdEdge Technologies cryogen-free helium setup, and Oxford Instruments MercuryiTC temperature controller. Data was collected with modulation frequency at 100 kHz, modulation amplitude at 10 G, and several temperatures and microwave powers: 3.8K (0.1, 1, 10 mW), 10K (1 mW), 20K (1 mW), and 40K (1 mW). EPR spectra under these same conditions were also

collected for buffer and blank samples to assist with background correction. Simulations of the EPR spectra of previously characterized CpII redox species were generated using the EasySpin package in MATLAB.

3.4 Results and Discussion

3.4.1 CpII Redox Species Pre- and Post-Illumination

Photochemical reduction of CpII by CdS QDs was monitored via EPR spectroscopy at two QD:CpII ratios, 1:1 and 3:1. The EPR experimental parameters were guided by previously established temperature and power dependences of known EPR-active CpII redox species; the most relevant species and g-values can be found in **Table 3.1**.[10,11] **Figure 3.3** shows a selection of the QD-CpII EPR data, displaying the redox species visible in the pre- versus post-illuminated sample spectra measured at 3.8K. Pre-illumination, the EPR spectra across the temperature range of 3.8 to 40 K are primarily composed of the oxidized H-cluster (H_{ox}) signal. This is consistent with CpII being in a pre-reaction resting state. After 1970 s of illumination—which supports the formation and transfer of photo-excited electrons from CdS to CpII—we observed the appearance of features of reduced F-clusters ($F_{2.061}$ and $F_{2.058}$). There is also a loss of H_{ox} and appearance of an axial signal with g-values around 2.11 and 1.87, similar to the features of a doubly reduced H-cluster state known as H_{sred}. Although characterized in in other [FeFe] hydrogenases such as HydA1 from *Chlamydomonas reinhardtii*, H_{sred} has not yet been definitively identified in CpII.[10,19]

Table 3.1: CpII redox species, their EPR signal type and g-values. $F_{2.061}$, $F_{2.058}$, H_{ox}, and H_{ox}-CO g-values were determined in previous work, the possible H_{sred} g-values were obtained from simulations of EPR spectra at 3.8K, 10 mW.[10,11]

CpII Redox Species, EPR signal	g-values
$F_{2.061}$, rhombic	2.061, 1.920, 1.887
$F_{2.058}$, rhombic	2.058, 1.931, 1.891
H_{ox}, rhombic	2.0795, 2.0284, 2.000
H_{sred}, axial	2.11, 1.87
H_{ox}-CO, rhombic	2.032, 2.017, 1.998

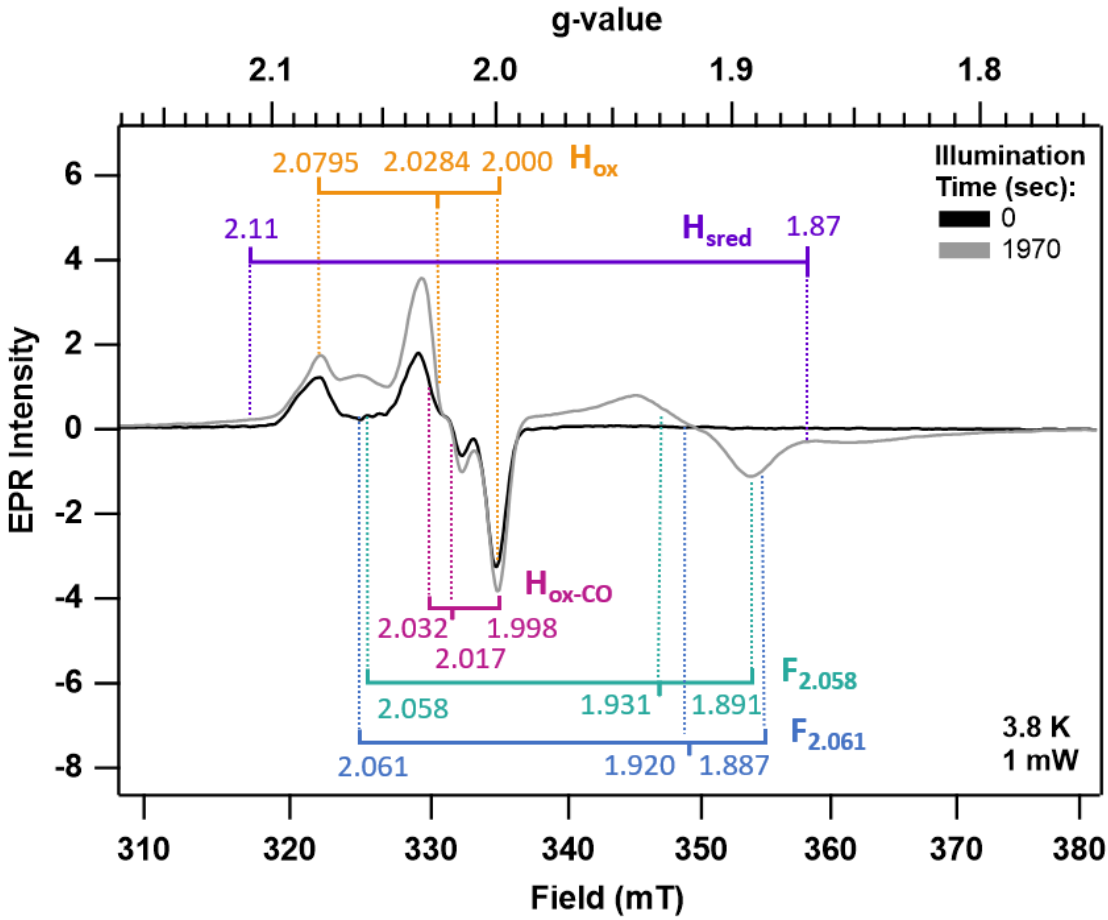

Figure 3.3: Selected EPR spectra of the QD-CpII sample at a 1:1 QD:CpII ratio at 3.8K, 1 mW, before and at one of the post-illumination time points to demonstrate the EPR-active CpII redox species present.

A control rection of illumination of CpII without QD present did not demonstrate any of the aforementioned CpII reduced states, but did reveal an additional photoinduced species present at g ~ 2.032, 2.017, 1.998 that was also present in the QD-CpII samples. This signal may be attributed to H_{ox}-CO—a catalytically inactive H-cluster state with an extrinsic CO bound.[11] Alongside the growth of this possible H_{ox}-CO feature, the CpII-only sample also exhibited decay of H_{ox} with increasing illumination time (**Figure 3.5**). Previous work has shown that in certain hydrogenase species, illumination may cause degradation of H_{ox} due to a photolytic release of CO from the H-cluster; this free CO can bind to neighboring intact H-clusters, forming the H_{ox}-CO state.[20] This separate photoinduced H_{ox} decay pathway will be accounted for in the kinetic analysis below.

3.4.2 Time Dependent Trends of Photochemically-Generated CpII Redox Species

The rise and decay kinetics of the CpII redox species as a function of illumination time with the QD provide insight into this photoinduced electron transfer pathway. Here, we observe these kinetics for three of the identified species—$F_{2.058}$, H_{ox}, and the possible H_{sred} signal—from the magnitude of the EPR signal at select g-values and measurement temperatures at which only one redox species is the primary contributor to the signal, as listed in **Table 3.2**, and simulations of the EPR spectra under these conditions and parameters are shown in **Figure 3.4**. We will begin by examining the general trends exhibited by the time-dependence of each species, before moving on to a more detailed look via kinetic modeling in Section 3.4.3.

Table 3.2: The g-values and measurement conditions selected for evaluation of photoinduced changes in CpII redox species.

CpII Redox Species	g-value	Temperature	Microwave Power
H_{ox}	2.079	40 K	1 mW
$F_{2.058}$	1.943	20 K	1 mW
H_{sred}	1.820	3.8 K	10 mW

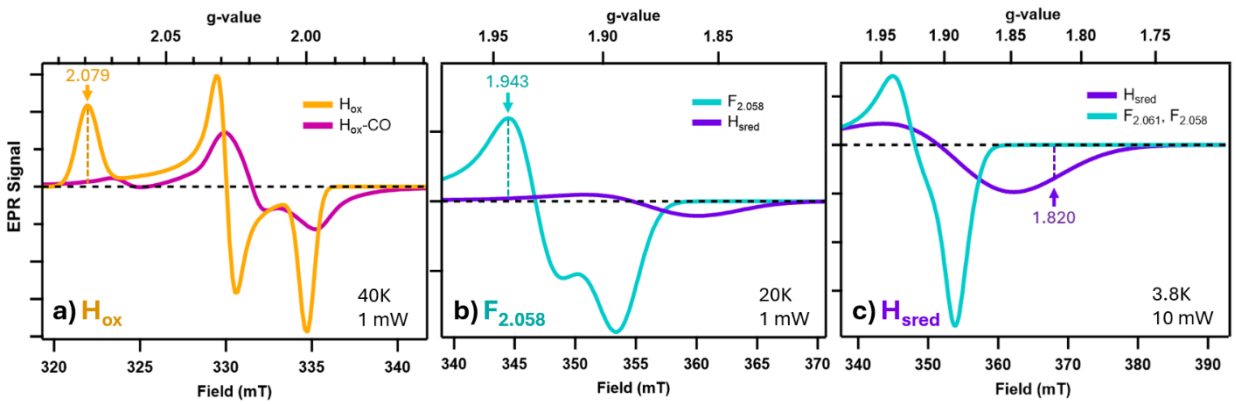

Figure 3.4: Simulated EPR spectra at the temperature and microwave power conditions at which the illumination time dependence of the CpII redox species a) H_{ox}, b) $F_{2.058}$, and c) possible H_{sred} were monitored. The simulations shown represent the relative intensities of the species at a sufficiently late illumination time (2200 s) for the photoinduced CpII states (reduced F-clusters, H_{sred}, and H_{ox}-CO) to have grown in. The Hox-CO signal shown in a) was obtained from EPR spectra of CpII samples with added CO.

First, we address the H_{ox} kinetics; as mentioned above, in addition to the reductive conversion of H_{ox} due to photoexcited electron transfer from the QD, the H_{ox} signal was subject to a photoinduced decay. This is hypothesized to be a result of photolytic loss of H-cluster CO ligands. **Figure 3.5a** shows the illumination-dependent H_{ox} decay and of the CpII-only sample alongside that of the two QD-CpII samples, normalized at time zero. The CpII-only H_{ox} decay fit well to a single exponential decay with rate constant $k_{hox,hv} = 4 \pm 0.2 \times 10^{-5}$ s^{-1}. While we do not necessarily expect the rate of this process to be the same in the QD-CpII samples, qualitative comparison of the slope of the H_{ox} decay in QD-CpII samples (**Figure 3.5a**) suggests that at least part of the photoinduced H_{ox} decay at late times >200 s is caused by this proposed photolytic CO

ligand loss. This may indicate that the H_{ox} decay caused by QD photoreduction does not continue indefinitely, but eventually slows and saturates.

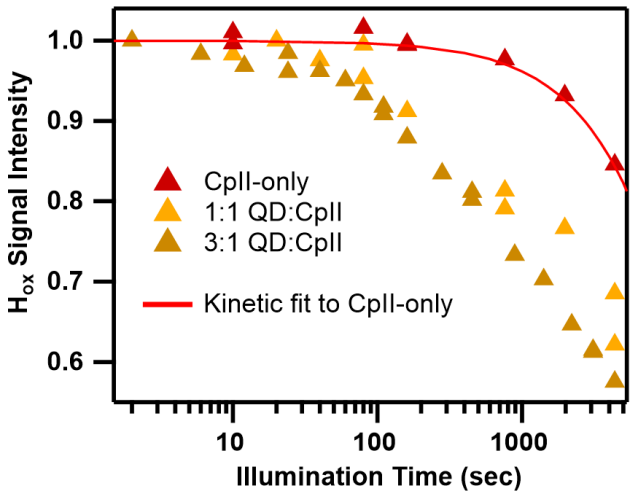

Figure 3.5: Illumination time-dependence of the decay of H_{ox} of the CpII-only sample versus the QD-CpII samples, H_{ox} signal normalized at t = 0. The CpII-only H_{ox} kinetics were fit to a single exponential decay.

We continue by examining the illumination time-dependences of the H_{ox}, $F_{2.058}$ and H_{sred} signal in relation to each other (**Figure 3.6**). The $F_{2.058}$ and H_{sred} signals were background subtracted to zero at time zero, and normalized at the final illumination time shown at 4370 s. The 1:1 and 3:1 QD:CpII ratios demonstrated the same kinetics for the $F_{2.058}$ and H_{sred} species, while the 3:1 sample demonstrated slightly more decay of the H_{ox} signal than in the 1:1 sample. At early illumination times <40 sec, we observe the rise in the $F_{2.058}$ signal. While H_{ox} species also decays slightly (~5%) in this window, the majority of the photoreduction-induced decay in H_{ox} occurs at later times >100 sec illumination, after the rise of $F_{2.058}$ has begun to saturate. The rise of the possible H_{sred} feature similarly begins in this later time window.

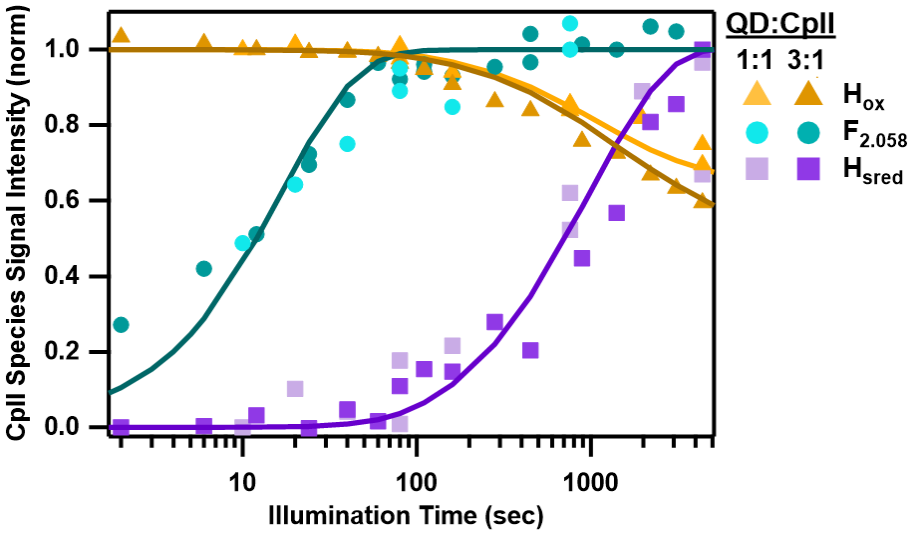

Figure 3.6: Illumination time-dependence of three CpII redox species, H_{ox}, $F_{2.058}$, and possible H_{sred} signal. H_{ox} signal was normalized to 1 at time zero, while $F_{2.058}$ and H_{sred} signal intensities were normalized at the final illumination time point shown. Fits to the kinetic model depicted in **Figure 3.7** are overlaid; the H_{ox} kinetics differed slightly between the two QD:CpII ratios, while $F_{2.058}$ and H_{sred} kinetics were the same for both ratios.

Qualitatively, these observations support the proposed model of photoreduction of CpII by the QD as depicted in **Figure 3.1a**, in which the photoexcited QD injects electrons into CpII via the native charge transfer pathway, namely in a sequential manner from the F-clusters to the H-cluster active site. This is similar to the results observed previously in photochemical QD-hydrogenase EPR, except that in the previous work—which involved QDs paired with [FeFe] Hydrogenase I from *Clostridium acetobutylicum* (CaI)—the H_{ox} signal decayed almost completely by the end of the illumination period. One possibility is that some of the remaining H_{ox} signal is due to a percentage of CpII in the sample which does not have a QD bound, and therefore cannot be photoreduced. However, the CpII concentration dependence of photochemical H_2 production showed saturation of H_2 production at QD:CpII ratios >1 (**Figure 3.2**). Correspondingly, an increase in the QD:CpII ratio from 1:1 to 3:1 in the EPR experiments resulted in a minimal change to the percentage of photoreduced H_{ox} signal decay, from ~25% to 35% in the 1:1 and 3:1 samples, respectively (**Figure 3.5b**).

Alternatively, the high fraction of H_{ox} remaining in CpII at late times may be a result of CpII's differing intraprotein electron transfer directionality compared to CaI; it has been demonstrated prior that the thermodynamic landscape of the F- and H-clusters of CpII allow for greater stabilization of H_{ox} compared to its reduced states.[7] The fact that we see possible signal from the two-electron reduced state H_{sred} indicates that despite CpII's bias toward H_2 oxidation, paired with QDs we are able to sufficiently reduce the CpII active site to accumulate a redox intermediate from the later stages of the H_2 reduction reaction direction. The apparent accumulation of H_{sred} may also lend insight into how the catalytic mechanism of CpII is uniquely tuned for H_2 oxidation by passing through this particular two-electron reduced state. As depicted in **Figure 3.1b**, in the proton reduction direction of catalysis after H_{sred}, the H-cluster passes through another state, H_{hyd}, before H_2 is released. If the equilibrium between these two states favors H_{sred}, this would presumably favor catalytic bias in H_2 oxidation direction since the H-cluster would therefore spend less time in the H_{hyd} state needed for H_2 evolution. That we see evidence of the H_{sred} signal but no visible signs of H_{hyd} may suggest that we are indeed seeing selective stabilization of H_{sred} as one of the means through which the catalytic bias of CpII is tuned.

3.4.3 Modeling of Photoreduced CpII Electron Transfer Kinetics

To delve further into these remaining questions regarding the picture of CpII electron transfer pathways, we turn to kinetic analysis of the illumination time dependence of the $F_{2.058}$, H_{ox}, and possible H_{sred} signals. Our kinetic model is depicted in **Figure 3.7** below. Assuming electron injection from the QD to occur via the native electron transfer pathway for the H_2 reduction direction, the distal F-cluster (F_1) is the first to be reduced (k_1), followed by electron transfer (k_2) from F_1 to the proximal F-cluster (F_2). Electron transfer from F_2 to the H-cluster (k_3) converts H_{ox} into the one-electron reduced state, H_{red}—this step may or may not also involve

proton binding. Transfer of a second electron through the F-cluster relay to H_{red} (k_3) results in the two-electron reduced state, H_{sred}; this model assumes that the rate constant electron transfer from F_2 to H-cluster is the same regardless of the redox state of the active site. Finally, proton transfer and H_2 release (k_4) restore the H_{ox} resting state. Electron transfer between each of the F- and H-clusters is reversible (k_{-2}, k_{-3}). In principle, back-electron transfer from F_1 to the QD is also possible (k_{-1}), but fitting to the experimental data resulted in low to negligible k_{-1} values, so was therefore not included in the final model. Binding of H_2 to H_{ox} to form H_{sred} (k_{-4}) was also not included, as the H_2 produced by CpII turnover would be negligible and the sample contained no other source of H_2.

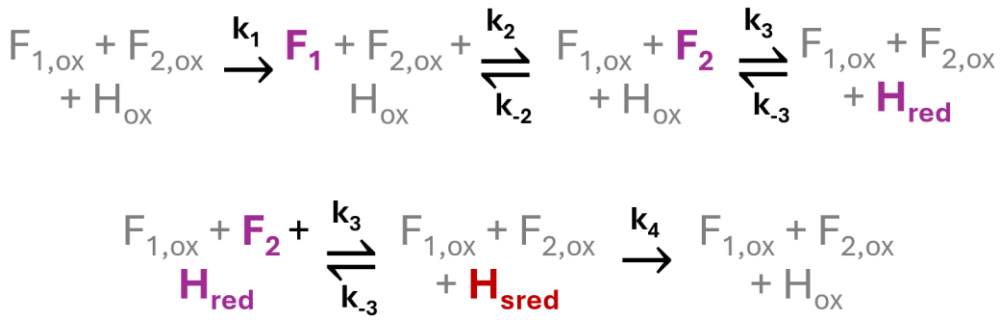

Figure 3.7: Kinetic model of photoreduction of CpII in a CpII-CdS QD system. Oxidized states are in grey, one-electron reduced states in magenta, and the two-electron reduced state in red. Also included in the model but not depicted here is the previously discussed photoinduced decay of H_{ox} with rate constant $k_{hox,hv}$.

The differential equations for each CpII redox species as determined by the kinetic model in **Figure 3.7** are shown in **Table 3.3**. The EPR-active states are F_1, F_2, H_{ox}, and H_{sred}, while H_{red} and the oxidized F-cluster states $F_{1,ox}$ and $F_{2,ox}$ are EPR silent. The coupled differential equations were solved numerically using an ordinary differential equation solver in MATLAB and fit simultaneously to all three of the experimental redox species kinetics—H_{ox}, $F_{2.058}$, and H_{sred}—in **Figure 3.6** using pyABC, a Python-based parameter inference package. For fitting to the $F_{2.058}$ kinetics, fitting to F_1 and F_2 signal were both tested.

Table 3.3: Differential equations for each redox species in CpII and EPR status.

Redox Species	Differential Equation	EPR signal
F_1	$\frac{d[F_1]}{dt} = k_1[F_{1,ox}] - k_2[F_1][F_{2,ox}] + k_{-2}[F_{1,ox}][F_2]$	active
F_2	$\frac{d[F_2]}{dt} = k_2[F_1][F_{2,ox}] - k_{-2}[F_{1,ox}][F_2] - k_3[H_{ox}][F_2] + k_{-3}[H_{red}][F_{2,ox}]$	
H_{ox}	$\frac{d[H_{ox}]}{dt} = -k_3[H_{ox}][F_2] + k_{-3}[H_{red}][F_{2,ox}] + k_5[H_{sred}] - k_{hox,hv}[H_{ox}]$	
H_{sred}	$\frac{d[H_{sred}]}{dt} = +k_4[H_{red}][F_2] - k_{-4}[H_{sred}][F_{2,ox}] - k_5[H_{sred}]$	
H_{red}	$\frac{d[H_{red}]}{dt} = -\left(\frac{d[H_{ox}]}{dt} + \frac{d[H_{sred}]}{dt}\right)$	silent
$F_{1,ox}$	$\frac{d[F_{1,ox}]}{dt} = -\frac{d[F_1]}{dt}$	
$F_{2,ox}$	$\frac{d[F_{2,ox}]}{dt} = -\frac{d[F_2]}{dt}$	

The average rate constants resulting from the best fit to the photoreduction kinetics of $F_{2.058}$, H_{ox}, and H_{sred} are shown in **Table 3.4**. The $k_{hox,hv}$ and k_1 rate constants were allowed to vary between the two QD:CpII ratios, while the others were kept constant. The model fits to all three experimental traces fairly well (**Figure 3.6**), with the exception of the very early time points of the $F_{2.058}$ signal < 12 sec; this may be a result of some of our simplifying assumptions (such as the lack of inclusion of possible differences in rate between the first and second electron transfer to the H-cluster), or simply error due to larger signal to noise in the $F_{2.058}$ signal in the initial illumination time points. Due to the relatively high number of fit parameters, some of the results have large uncertainty, primarily k_2, k_{-2}, and k_4. The best fit results for k_2 and k_{-2} both span a relatively wide

range of values, preventing a definitive discussion of the relative rates of electron transfer between the F-clusters. It should also be noted that while the fits in **Table 3.4** represent fitting the $F_{2.058}$ kinetics to the F_2 signal, similar residuals can be obtained by fitting $F_{2.058}$ to F_1, as the k_2/k_{-2} ratio is a large determining factor in distinguishing the F_1 and F_2 kinetics. The rate of the final step of H_2 release from H_{sred} to restore H_{ox}, k_4, has the highest degree of uncertainty spanning several orders of magnitude. However, the remaining fit parameters demonstrate much higher consistency in their best fit values; we discuss these below.

Table 3.4: Kinetic fit results of the photochemically-induced changes in H_{ox}, $F_{2.058}$, and H_{sred} EPR signal in QD-CpII complexes fit to the model from **Figure 3.7**.

Rate constant	**Average fit value (s^{-1}) QD:CpII ratio**	
	1:1	**3:1**
$k_{hox,hv}$	**0.000015** ± 0.000004	**0.000040** ± 0.000008
k_1	**0.08** ± 0.05	**0.10** ± 0.05
k_2	**100** ± 40	
k_{-2}	**50** ± 30	
k_3	**0.0003** ± 0.00004	
k_{-3}	**0.5** ± 0.2	
k_4	**0.1 to 100**	

The first step—electron injection from QD to F_1, defined by rate constant k_1—is a product of the excitation frequency of the QD and the quantum efficiency of QD-to-CpII electron transfer. The best fit gives an average value of k_1 at least 10 times smaller than k_2.and k_{-2}. Considering that previous work has demonstrated evidence of spin-spin coupling between the two F-clusters of CpII, it is reasonable to expect this inter-cluster electron transfer to be faster than the interfacial transfer from QD to enzyme, particularly considering that k_1 is limited by the photoexcitation rate and QEET. The fit results for the transfer between F_2 and the H-cluster, however, are perhaps the most interesting. The average fit result for k_3 is 10^3 times smaller than the reverse transfer step k_{-3}. This implies highly directional electron flow with a high barrier to transfer from F_2 to the H-

cluster, and correspondingly favored transfer from H-cluster to F_2. These relative rates agree well with the "Model 2" thermodynamic landscape of CpII proposed by Kisgeropoulos et al., in which the F-cluster with the more positive potential ($F_{2.058}$) is the one located proximal to the H-cluster (F_2), with the more negative potential F-cluster ($F_{2.061}$) in the distal position (F_1).[10] The fact that k_{-3}/k_3 reflects the same ~10^3 order of magnitude as the reported H_2 oxidation bias of CpII[7] is also highly suggestive that the directionality of electron transfer between the metalloclusters in CpII is a key contributor to the resulting catalytic bias.

3.5. Summary and Conclusions

The use of light-activated means for electron injection into the CpII hydrogenase enabled tracking of the EPR signals of CpII redox species as a function of illumination time, providing a window into the intraprotein electron transfer kinetics and catalytic mechanism. Upon illumination of CdS QD-CpII biohybrids, EPR signatures of reduced F-clusters grew in, followed by the decay of H_{ox}, both processes eventually reaching saturation. At later illumination times, along with the decay of H_{ox} there was also a rise in features of a possible two-electron reduced H_{sred} species. These results support the proposed model that the QD is injecting photoexcited electrons into CpII through the same pathway as the native ferredoxin redox partner, from distal F-cluster to H-cluster. The presence of a possible H_{sred} signature also lends insight into the catalytic mechanism of CpII and how selective stabilization of H_{sred} over H_{hyd} may contribute to CpII's bias toward H_2 oxidation.

To examine the relative rates of individual steps in the CpII intraprotein electron transfer relay, a kinetic model was proposed and fit to the illumination time dependence of the $F_{2.058}$, H_{ox}, and H_{sred} signals. The fit results imply a large barrier to electron transfer from proximal F-cluster to H-cluster, as k_3 is three orders of magnitude smaller relative to k_{-3}. This supports the previously

proposed model for the thermodynamic landscape of the CpII electron relay, which places the higher potential F-cluster as most likely to be in the position proximal to the H-cluster active site such that electron transfer away from the H-cluster is strongly favored, enabling bias for the H_2 oxidation direction of catalysis.[10]

Overall, in this work we have used a biohybrid approach to light-controlled electron injection into CpII to address fundamental questions on the intraprotein electron transfer dynamics and functional contribution to catalysis. In doing so we have furthered our understanding of how metallocluster properties, the thermodynamic and electronic landscapes, and catalytic mechanisms of hydrogenases may impact the directionality of electron flow and catalytic bias. Such understanding provides insights towards the improved design of complex chemical conversion processes.

3.6. Future Work and Outlook

Several next steps will strengthen and add to the outcomes from this work. First, simulation of the full temperature and microwave power dependence of the EPR spectra using the EasySpin software package for MATLAB will allow for extracting spectra such as the $F_{2.061}$ signal from other overlapping spectra, as well as quantification of all identifiable F- and H-cluster redox species using a copper standard. In particular, this will enable us to add the time dependence of the $F_{2.061}$ signal to fit to the kinetic model, and spin quantization will enable us to know the percentage change in F-cluster reduction. Both of these additions to our analysis will further reduce the degrees of freedom in the kinetic fit and will provide important support for the assignment of the structural arrangement of the F-clusters and the relative intercluster electron transfer rates. Second, Fourier transform infrared spectroscopy measurements of CdS QD-CpII samples before

and during illumination will assist in more definitive identification of the H-cluster signals observed in the photochemical EPR experiments, such as H_{ox}-CO and H_{sred}.

More broadly, the use of semiconductor nanocrystal-enzyme biohybrids in photochemical EPR experiments as applied here has the potential to answer many further detailed questions regarding redox enzyme electron transfer and catalysis. These experiments provide a complement to data obtained from chemical reduction of redox enzymes, as the light-induced nature of the biohybrid system allows for time-dependent control of electron injection, and the electrostatic surface properties of the nanocrystal can be tuned to mimic the enzyme's binding orientation with its native redox partner, allowing for observation of electron injection targeted through the native pathway.[14] Much exciting work has already been and continues to be conducted with the use of photochemical EPR experiments on nanocrystal-nitrogenase biohybrids to uncover insights into biological ammonia production.[21–24] In the [FeFe] hydrogenase family to which CpII belongs, the various determining factors behind this enzyme family's dramatic range in control over electron transfer directionality are still being comprehensively understood.[7,10] Comparison of photochemical EPR experiments across a range of related hydrogenases, such as Hydrogenases I and III from *Clostridium pasteurianum* (CpI and CpIII), could lend valuable insight into the ways in which F-cluster arrangement and properties as well as the favoring of different H-cluster states contribute to the control of electron transport in these and other biological systems.

Chapter 4

Rate Limiting Regimes in Photochemical H_2 Generation by Complexes of Colloidal CdS Nanorods and Hydrogenase

4.1 Abstract

Driving redox enzyme catalysis with semiconductor nanocrystals has emerged as a compelling approach for new chemical conversion strategies. Tuning catalytic outcomes in these systems requires an understanding of the impacts and interplay of the different chemical steps involved, many of which occur at unknown rates. We reveal the roles of various steps in determining the photochemical H_2 production rates with complexes of colloidal CdS nanorods and [FeFe]-hydrogenase (H_2ase). We developed kinetic Monte Carlo simulations of the overall light-driven catalytic cycle to analyze experimental H_2 production trends. We focused on three critical processes that have been elusive to date: scavenging of photoexcited holes from photoexcited nanorods, back-electron transfer, and H_2 oxidation. Simulations and fitting of experimental H_2 production trends reveal that hole transfer becomes the prominent rate-limiting step at high illumination intensities. Comparison of simulations to experimental H_2 production reveal that both back-electron transfer and H_2 oxidation play an efficiency-limiting role at high catalyst loadings. Our work reveals how experimental parameters can be tuned to minimize the role of energy-wasting pathways and optimize photochemical product formation. More broadly, our approach demonstrates how critical but elusive chemical steps in multi-step photochemical reactions can be probed with a combination of experiments and simulations.

4.2 Introduction

Over the last decade, the concept of driving redox enzyme catalysis with photoexcited colloidal semiconductor nanocrystals has evolved from initial reports of catalysis of H_2 generation with hydrogenases to a wide range of reactions. Examples include N_2 fixation, carbon-carbon bond and CO formation via CO_2 reduction, CO reduction to hydrocarbons, regeneration of biological cofactors, fumarate to succinate reduction, and myristic acid monooxygenation, among others.[1–8] While this approach holds promise for light-driven enzymatic reactions to upcycle low-value chemicals into valuable products, challenges remain in understanding—and therefore controlling—the factors that govern the photochemical outcomes in these systems. Consequently, we do not yet know how to design nanocrystal-enzyme experimental systems to convert photon energy into chemical products with optimal quantum yields (QYs) and minimal losses to unproductive pathways. Here, we address this challenge by examining the kinetics of individual steps involved in light-driven catalysis in a model nanocrystal-enzyme system to identify the reaction regimes under which particular processes become rate-limiting.

We focus on CdS nanorods paired with [FeFe]-hydrogenase I from *Clostridium acetobutylicum* (H_2ase) for photochemical production of H_2 (**Figure 4.1**). H_2ase is a redox enzyme that catalyzes reversible H_2 activation, producing H_2 from reduction of two protons by two electrons or electrons and protons from H_2 oxidation.[9–11] The CdS nanorods, functionalized with negatively-charged mercaptopropionate surface-capping ligands, are thought to adsorb electrostatically to H_2ase at the binding site of the natural ferredoxin electron carrier.[11,12] To produce H_2, CdS nanorods absorb light and transfer the photoexcited electrons to the H_2ase, which in turn uses them to drive catalysis. During this process, photoexcited holes are removed from the nanorod by a sacrificial hole scavenger such as ascorbate (Asc). An important consequence of the

stochastic electrostatic interaction between the nanorods and H_2ase is that it leads to a Poisson distribution in the number of enzymes bound per nanorod (N_{cat}).[11–15] This ensemble distribution of N_{cat} must be taken into account when extracting quantitative kinetic information from experimental data.[13–16]

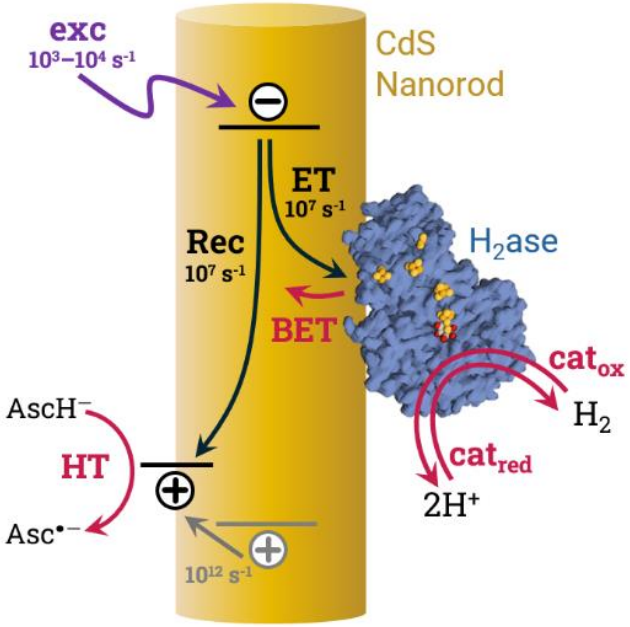

Figure 4.1: Scheme of light-driven H_2 production in a CdS nanorod-H_2ase system, which involves several processes, including photoexcitation (exc), electron transfer (ET), electron-hole recombination (Rec), hole transfer (HT), back-electron transfer (BET), and catalyst turnover (cat_{red}, cat_{ox}). These last three—the processes in red—will be the focus of our discussions.

Previous studies have revealed the kinetics of some critical steps in this photochemical reaction (**Figure 4.1**). Under typical solution conditions with continuous wave excitation comparable with the intensity of the solar spectrum, the photoexcitation rates (R_{exc}) are on the order of 10^3-10^4 s^{-1} $nanorod^{-1}$.[11] In the CdS nanorods, above-bandgap photoexcited electrons and holes cool to the band edges and holes localize (i.e. trap) to undercoordinated surface sites on a sub-picosecond timescale.[17–19] As such, the relevant nanorod excited state for electron transfer (ET) to H_2ase consists of a surface-trapped hole and a conduction band edge electron. Prior transient absorption spectroscopy experiments showed that electron-hole recombination (Rec) and

nanorod-to-H_2ase ET occur with rate constants (k_{Rec}, k_{ET}, respectively) of ~10^7 s^{-1} for nanorods capped with 3-mercaptopropionate surface ligands (there is also a less dominant electron trapping pathway, not shown).[12–14,16]

Prior work has revealed that quantum efficiency of electron transfer (QEET), i.e., the probability that the electron will transfer to H_2ase rather than relax by other means, plays a governing role in the QY of H_2 production, i.e., the number of photochemical H_2 molecules produced per every two photons absorbed.[12,14,16] k_{ET} and the resulting H_2 generation rate (R_{H2}) have been shown to depend strongly on the surface-capping ligands, revealing the critical role of the ET interface.[16] In prior studies, the QY of H_2 production from nanorod-H_2ase complexes remained constant with increasing light intensity, resulting in a linear relationship between the net rate of H_2 production per nanorod (R_{H2}) and R_{exc}.[11] Here, we will refer to this scenario as the "photon-limited" regime.

Considerably less is known about the role of other steps in the overall H_2 production catalysis, shown with red arrows in **Figure 4.1**. Hole transfer (HT) to Asc must keep up with ET to maintain the charge carrier flow in the photochemical cycle. R_{H2} increases linearly with Asc concentration until reaching saturation; the typical H_2 production experiments are done in this regime where H_2 production is not changing with Asc concentration.[11] While these Asc concentrations have previously been sufficient to maintain a photon-limited H_2 production trend, one may imagine that with increasing light intensity, HT may eventually not be able to keep up with the electron injection and thereby become the rate-limiting step. The rates of HT per nanorod (R_{HT}) in these systems have not been reported, presumably due to the experimental challenges associated with the weak spectroscopic signatures of trapped holes.[19–22]

Lastly, perhaps the least-characterized steps in the nanorod-H_2ase system are the processes which reverse the steps of H_2 production. Prior experiments in which R_{H2} and QY decreased at high H_2ase:nanorod ratios raised the possibility of back-electron transfer (BET) pathways.[11] BET here refers to the reversal of ET, in which an electron transferred to H_2ase is lost, either through return to the nanorod or lost to other components in solution. The other potentially relevant back-reaction process is the catalytic oxidation of H_2 by H_2ase, which leads to reduction of the H_2ase, followed by BET.

To minimize the role of non-productive pathways and enhance control of the desired photochemical pathways, more understanding is needed for how each process impacts H_2 production trends and which parameters are key to controlling that impact. Herein, we explore the roles and impacts of these elusive steps—HT, BET and H_2 oxidation pathways—in photochemical H_2 production in complexes of CdS nanorods and H_2ase. To do so, we use a combination of experimental H_2 production data and kinetic Monte Carlo (kMC) simulations of the photochemical cycle. We begin by describing our kMC method and our model of photochemical H_2 production by CdS nanorod-H_2ase complexes. We use the insights from experimental and kMC simulation data to discuss the relevance and impacts of each type of rate-limiting case to reveal new understanding for how to control photochemical product formation in these systems. Our approach that combines experiments and simulations is broadly applicable to a variety of complex photochemical reactions.

4.3 Experimental Methods

4.3.1 [FeFe] Hydrogenase Expression, Purification, and Characterization

CaI was expressed heterologously in *E. coli* by co-transformation of the cell line BL21 (DE3) ΔiscR as described previously with maturase and structural gene constructs (pCaFG,

pCaAE).[23] With a fresh transformation, 5 mL of Terrific Broth (TB) media (EMD Millipore) was supplemented with antibiotics (Streptomycin 50 µg/mL, Carbenicillin 200 µg/mL, and Kanamycin 30 µg/mL), inoculated with several colonies, then cultured overnight at 37 °C and 250 rpm. The following morning, the culture was spun down for 5 min at 4,000 rpm, then washed and resuspended in fresh TB media (Novagen). From this, two 50 mL flasks of TB media with antibiotics were inoculated (1:50) and grown for three to four hours to an OD600 of 0.5. The cultures were used to inoculate (1:100) a 10 L Sartorius Stedim Biotech fermenter with TB media plus antibiotics. The fermenter culture was grown to an OD600 of 0.6 at 37 °C with 250 rpm stirring and 0.9 L/min air bubbling. For induction, 1.5 mM IPTG was added, followed by 4 mM ammonium iron (III) citrate, 1 mM cysteine, 0.5% glucose, and 10 mM sodium fumarate. Stirring was then adjusted to 75 rpm, the temperature to 30 °C, and air bubbling switched to N_2 at 0.3 L/min.

The anaerobic induction continued overnight, and the following morning the cells were harvested with an in-line centrifuge (Eppendorf) at 3000 rpm under N_2. The in-line centrifuge cell was transferred to a Coy Laboratories glovebox (3% H_2 atmosphere), the cells washed with buffer A (50 mM Tris pH 8, 5 mM NaCl, 5% glycerol, 5 mM NaDT), then stored at -80 °C. Purification of Strep-tagged CaI was carried out via modifications to a previously described procedure, incorporating StrepTag-II chromatography and anion exchange steps. All the buffers were stringently degassed for a minimum 12 h under vacuum and transferred to an MBraun anaerobic chamber (N_2 atmosphere) for the purification. Pellets from the equivalent of 5 L of culture were thawed, diluted with lysis buffer containing 20 mg lysozyme, 2 mM DTT, 30 µL Pierce universal nuclease, and 1 table EDTA-free protease inhibitor cocktail from Roche Life Sciences, then passed through a microfluidizer 12 times. After lysis, a heat shock stock (55 °C, 20 min) was incorporated

to help with initial separation of the hydrogenase maturates from CaI. Broken cells were subjected to ultracentrifugation at 45 K rpm for 1 h at 4 °C to pellet the insoluble fraction. The cell-free lysate was initially purified over DEAE resin (GE Healthcare) in an MBraun box, washed with Buffer A, and eluted using a 4 column volume (CV) gradient to buffer B (50 mM Tris pH 8, 1 M NaCl, 5% glycerol, 5 mM NaDT). Fractions were collected and analyzed for protein content by SDS-PAGE and hydrogenase activity assay (10 mM NaDT, 5 mM methyl viologen) for H_2 evolution measured by GC chromatography (Agilent Technologies). The active fractions were combined and concentrated to ~30 mL using 30 kDa MWCO membrane and Amicon concentrator cell (50 psi Argon gas). The concentrated fraction was purified over 25 mL Strep-Tactin Superflow High Capacity resin (IBA) using buffer C (50 mM Tris pH 8, 200 mM NaCl, 5% glycerol, 5 mM NaDT). After washing with buffer C for 2 CVs, pure CaI was eluted by addition of 2.5 mM desthiobiotin and stored at 4 °C. Purity was assessed with SDS-PAGE, protein concentration was determined using Bradford assay (Bio-Rad), and activity by hydrogenase H_2 evolution assays.

4.3.2 CdS Nanorod Synthesis and Ligand Exchange

Materials: tributylphosphine (97%, Aldrich), hexamethyldisilathiane (synthesis grade, Aldrich), octadecylphosphonic acid (99%, PCI), cadmium oxide (99.99%, Aldrich), trioctylphosphine oxide (99%, Aldrich), sulfur (99.998%, Aldrich), tri-n-octylphosphine (97%, Strem), hexylphosphonic acid (99%, PCI). The following solvents were obtained from Sigma-Aldrich: ethanol (200 proof anhydrous >99.5%), hexanes (mixture of isomers, anhydrous, >99%), toluene (anhydrous, 99.8%), isopropanol (anhydrous, 99.5%), methanol (anhydrous, 99.8%), octylamine (99%), chloroform (anhydrous, >99%, containing 0.5-1% ethanol as stabilizer), acetone (HPLC grade, >99.9%), nonanoic acid (96%). For the ligand exchange procedure:

tetramethylammonium hydroxide (>97%, Sigma Life Sciences), 3-mercaptopropronic acid (99%, Alfa Aesar).

The CdS nanorod synthesis procedure was modified from a published method.[1,2,24] A stock of CdS seeds was produced by injection at 321°C of a 3.0 g tributylphosphine + 0.17 g hexamethyldisilathiane sulfur precursor into a Cd-ODPA solution of 0.604 g octadecylphosphonic acid + 0.10 g cadmium oxide + 3.3 g molten trioctylphosphine oxide . Seeds were grown for 1 min and quenched by lowering the reaction flask temperature to 80°C in an oil bath. A 1:1 solution of toluene:methanol was injected into the flask and the particles were transferred under anaerobic conditions to an argon-filled glovebox. Purification of the seeds was carried out by three rounds of precipitation with methanol for the first two rounds and a 2:1 methanol:isopropanol v/v mixture for the third round, redissolving in toluene for the first two rounds and in hexanes for the last round. After 24 hours, the solution was centrifuged and the precipitate discarded. The particles were precipitated with isopropanol and the final product (for subsequent use for the nanorod synthesis) was redispersed in trioctylphosphine. The average seed diameter was determined to be 34 angstroms using the procedure from Yu et al.[25]

The CdS nanorods were produced by injection at 354 °C of the CdS seed solution containing 0.08 μmol CdS seeds + 0.12 g elemental sulfur + 1.5 g tri-n-octylphosphine into a solution of Cd-ODPA containing 0.086 g cadmium oxide + 0.08 g hexylphosphonic acid + 3 g molten trioctylphosphine oxide + 0.29 g octadecylphosphonic acid. After injection of the seeds, the solution temperature dropped to 329° C and was maintained at that temperature for 8 min of growth time. The reaction was quenched by reducing the solution temperature to 80 °C with an oil bath and injecting a 1:1:1 v/v/v mixture of acetone:methanol:toluene. The reaction solution was transferred anaerobically to an argon-filled glovebox and centrifuged. Nanocrystal precipitate

(identifiable by its yellow color) was redispersed in 1:1 v/v toluene:octylamine. The nanorods were precipitated with methanol, centrifuged, then redispersed in chloroform. Another precipitation step was carried out with nonanoic acid and ethanol, centrifuged, and the nanorod precipitate was dried under vacuum before being redispersed in hexanes. After 48 hours, the nanorod stock was centrifuged and the yellow supernatant containing the nanocrystals separated from the white pellet. A size selection was carried out on the nanorods, in which fractions particles were collected by dropwise isopropanol addition followed by centrifugation. Fractions with similar UV-vis absorption spectra were combined and redispersed in toluene.

The CdS nanorods were ligand exchanged to 3-mercaptopropionate ligands using an adaptation of a published method.[11,26] A 62.5 mM 3-mercaptopropionic acid solution was mixed in methanol with 1 g of tetramethylammonium hydroxide pentahydrate. 3 mL of the mercaptopropionic acid solution was added to 7 nmol in 0.4 mL of the as-purified CdS nanorods stock, which became opaque, then optically clear as the ligand exchange occurred. The newly-exchanged nanorods were precipitated with toluene, centrifuged, the clear supernatant discarded, and the particles dried under vacuum and redispersed in 12.5 mM Tris pH 7 buffer.

4.3.3 Nanocrystal Characterization

Nanorod dimensions were 23.6 ± 1.9 nm in length and 4.57 ± 0.35 nm in diameter as determined from measurement of 200 particles from transmission electron microscopy (TEM) images (**Figure 4.2a**). TEM samples were prepared by drop casting the native ligand nanorods from toluene solution onto 300 mesh, Electron Microscopy Sciences carbon-coated copper grids. Images were acquired with an FEI Tecnai 12 Spirit which was operating at 100kV, with a side-mount AMT (2k x 2k) CCD. ImageJ software was used to process the images.[27]

Molar absorptivity of the nanorod stock was determined based on prior work which correlated absorbance measurements with inductively coupled plasma optical emission (ICP-OES) spectroscopy resulting in $\varepsilon_{350} = 1710\ M^{-1}\ cm^{-1}$ per Cd^{2+}.[11] The average nanorod dimensions determined from TEM images as described above was used to calculate the per nanorod molar absorptivity $\varepsilon_{350,nanorod} = 1.33 \times 10^7\ M^{-1}\ cm^{-1}$. This $\varepsilon_{350,nanorod}$ was used to calculate CdS nanorod concentrations from absorbance measurements. A representative absorbance spectrum can be found in **Figure 4.2b**.

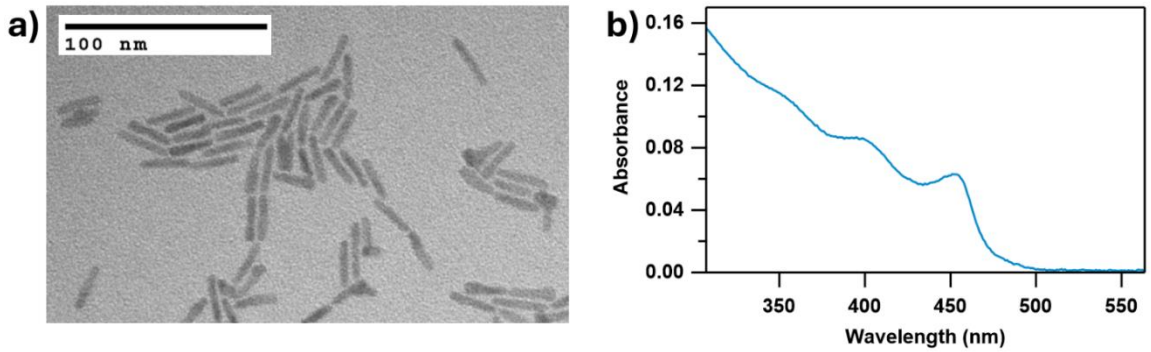

Figure 4.2: a) TEM image of the CdS nanorods used in photochemical H_2 production assay experiments from Figure 3 of the main text. b) Absorbance spectrum of the mercaptopropionate-capped CdS nanorods.

4.3.4 Light-Driven H_2 Production

The photochemical H_2 production data found in Figure 3 of the main text was obtained as follows: Solutions of 40 nM CdS nanorods and 20 nM H_2ase were prepared under anaerobic conditions in an argon-filled glovebox in a buffer containing 50 mM Tris-HCl, 5 mM NaCl, 5% glycerol, at pH 7 with the designated amount of Asc. The CdS nanorod-H_2ase samples were aliquoted into 1.5 mL serum vials, capped with rubber septa, and illuminated with a 447 nm diode laser (Laserglow Technologies, 10 to 148 mW) for 10 min while stirring. H_2 production was measured by taking a sample of the vial headspace to inject into an Agilent Technologies 7820A gas chromatograph (Argon carrier gas, molecular sieve 5A column, TCD detector). The calculation

of excitation rates in experimental photochemical H_2 production assays of CdS nanorod-H_2ase samples is shown in **Tables 4.1** and **4.2** below.

Table 4.1: Values used for R_{exc} calculations.

Wavelength of continuous wave laser	**447 nm**
Path length of assay vial (L)	0.9 cm
Concentration of CdS nanorods (C)	4×10^{-8} M
CdS nanorod molar absorptivity at 447 nm (ε)	7.1×10^{6} $M^{-1}cm^{-1}$
Nanorod absorbance at 447 nm ($A = C \cdot \varepsilon \cdot L$)	0.26
Nanorod sample transmittance at 447 nm ($T = 10^{-A}$)	0.55
Fraction of photons absorbed at 447 nm ($f_{abs} = 1-T$)	0.45
Energy per mol 447 nm photons ($E_p = N_A \cdot h \cdot c/\lambda$)	2.68×10^{5} J
Area of laser beam spot (A)	12.5 mm^2
Volume of laser beam through assay vial ($V = A \cdot L$)	112.5 mm^3
Mol CdS nanorods in laser beam ($n_{cds} = C \cdot V$)	4.5×10^{-12} mol

Table 4.2: Calculated R_{exc} values for experimental photochemical H2 production assay data shown in **Figure 4.4**.

Laser Power x 10^{-3}, P (W)	**[a] R_{exc} x 10^4 (exc/nanorod/s)**
10.5	0.39
20	0.74
35	1.29
50	1.85
80	2.96
110	4.07
145	5.36

$$^{(a)}R_{exc} = \frac{P \cdot f_{abs}}{E_p \cdot n_{Cds}}$$

4.3.5 Kinetic Monte Carlo Simulations and Fitting Experimental H_2 Production Trends

The kinetic Monte Carlo (kMC) simulation code was written using MATLAB 2020b and 2024b, and is available upon request. To estimate R_{HT} values from the experimental H_2 production trends in **Figure 4.4**, we carried out parameter inference with the assistance of the Python software package pyABC, which performs approximate Bayesian computation with sequential Monte Carlo

(ABC-SMC).[28] A simplified description of ABC-SMC as applied to our estimation of R_{HT} values is as follows: 1) for each [Asc], sample R_{HT} values are drawn from a given prior distribution and input into our kMC simulation, 2) the distance (here the sum of the squared residuals) between the resulting simulated and experimental H_2 production versus R_{exc} trends is calculated, 3) this process iterates, sampling from an increasingly smaller distribution of R_{HT} values as determined by which simulation results which produce the best agreement with the experimental data. During this process, for each of the three [Asc] traces the simulated H_2 production traces were normalized relative to the maximum R_{exc} point of the simulated 100 mM Asc trace prior to the distance calculation, such that the relative magnitude of H_2 production between the three [Asc] traces was taken into account in addition to the shape of each trend. The prior distribution of R_{HT} was set as a uniform distribution between 0 and 5.5×10^4 s^{-1}, as R_{HT} values larger than this range resulted in only linear H_2 production with R_{exc} which did not match the experimental trends. The end result of the ABC-SMC algorithm is a probability distribution—termed the posterior distribution—of R_{HT} values for each [Asc].

4.4 Results and Discussion

4.4.1 Simulations of Light-Driven H_2 Production

To identify the rate-limiting regimes in the photochemical cycle of the nanorod-H_2ase complexes, we developed simulations based on the kMC method, a numerical technique also known as a Markov random walk or stochastic simulation.[29] In the simulation of a single nanorod-H_2ase complex (i.e. a nanorod with one or more H_2ase bound), the procedure is as follows (**Figure 4.3**).

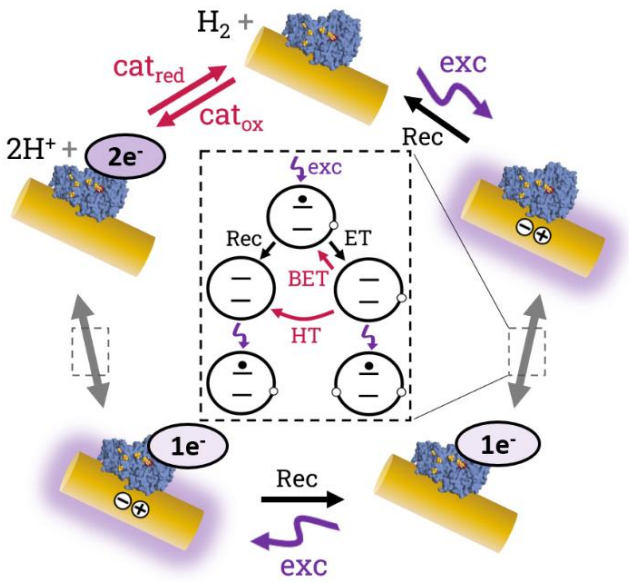

Figure 4.3: Sequence of simulated processes in a CdS nanorod-H_2ase photochemical system.

Each simulated photochemical H_2 production experiment is set to run for a designated length of "illumination time." The simulation is concluded when the total illumination time passed—as determined by the cumulative times of all elapsed excitations—has reached the preset illumination duration. Each excitation generates one photoexcited electron and hole; as mentioned above, this excited state consists of a conduction band electron and a surface-trapped hole. The next process to occur is stochastically determined according to the rates of the relevant processes; the rate of each process depends on the user-input rate constants as well as the current nanorod-H_2ase system conditions. For example, ET can only occur if a photoexcited electron is present in the nanorod. Specifically, we use the standard kMC "direct method" to determine the outcome of the competition between ET, recombination, HT, BET, catalyst turnover (reductive or oxidative direction—cat_{red} and cat_{ox}, respectively), and the next photoexcitation.[20]

In our simulations, we use the rate constants of ET and intrinsic CdS nanorod excited state relaxation pathways obtained previously from CdS nanorod-H_2ase transient absorption experiments: $k_{ET} = 2.4 \times 10^7\ s^{-1}$, $k_{Rec} = 1.5 \times 10^7\ s^{-1}$, the rate constant of electron trapping $k_{tr} = 1.1$

x 10^8 s^{-1} and average number of Poisson-distributed electron traps per nanorod $\langle N_{tr} \rangle$ = 0.59.[13] These parameters contribute to the resulting QEET, which quantifies the probability that the electron will transfer to H_2ase rather than relax by other means. For an individual nanorod, QEET is defined as shown in Eqn (1),

$$QEET(N_{cat}) = \frac{N_{cat} k_{ET}}{N_{cat} k_{ET} + k_{Rec} + N_{tr} k_{tr}}. \quad (1)$$

The primary outcome and role of electron trapping is the same as that of electron-hole recombination—an intrinsic nanocrystal excited state decay pathway which directly competes with ET. The electron-hole recombination rate also depends on the number of photoexcited holes present in the nanorod; under slow HT conditions excess holes will accumulate on the nanorod, as will be discussed below. In our model, each excess photoexcited hole in the nanorod correspondingly multiplies the rate of electron-hole recombination. Once H_2ase(s) begin to accumulate electrons, the catalyst turnover rates become relevant; for $k_{cat,red}$ we use a previously estimated value of 2.1 x 10^4 s^{-1},[10] except where discussed otherwise. Rates of H_2 oxidation and BET will be discussed in the final discussion section below. The rates of catalyst turnover and BET encompass several underlying processes such as intraprotein electron transport, proton transfer, and transitions between catalytic intermediates at the H_2ase active site.[30,31] To calculate the resulting rate of H_2 production from a simulation of a single nanorod-H_2ase complex, we divide the net amount of H_2 produced by the illumination duration. The quantum yield (QY) of H_2 production is similarly determined by dividing the net amount of H_2 produced by the total excitations elapsed, multiplied by two to account for H_2 production as a two-electron process.

Experimental samples of colloidal nanorod-H_2ase complexes consist of a distribution in the number of H_2ase catalysts bound per nanorod. For the CdS nanorod-H_2ase system here, we assume a Poisson distribution of N_{cat} characterized by an average number of H_2ase catalysts bound

per nanorod ($\langle N_{cat} \rangle$), as has been established previously.[11–14,16] The QEET for an ensemble sample with a distribution of nanorod-H_2ase complexes is defined according to Eqn (2),

$$QEET(\langle N_{cat} \rangle) = \sum_{Ncat=0}^{\infty} P(N_{cat}, \langle N_{cat} \rangle) \cdot QEET(N_{cat}) \quad (2)$$

where $\langle N_{cat} \rangle$ is the average N_{cat} for an ensemble of nanorod-H_2ase complexes, and $P(N_{cat}, \langle N_{cat} \rangle)$ is the Poisson distribution of N_{cat} for a given $\langle N_{cat} \rangle$.[14,15] The average rate of ET per nanorod-H_2ase complex (R_{ET}) in the ensemble is a product of the ensemble QEET and R_{exc}, as shown in Eqn (3),

$$R_{ET} = QEET(\langle N_{cat} \rangle) \cdot R_{exc} \,. \quad (3)$$

To simulate H_2 production of the ensemble, we simulate the time-evolution of individual nanorod-H_2ase complexes as described above for N_{cat} = 1 through $N_{cat,max}$ (determined as the N_{cat} at which the probability of occurrence is < 0.001 according to the Poisson distribution for a given $\langle N_{cat} \rangle$). After each excitation, the net cumulative amount of H_2 produced in the ensemble is represented by a Poisson-weighted average of the net H_2 production from each N_{cat} subpopulation. For the simulations that include H_2 oxidation, this ensemble net H_2 production value is then used to weight the rate constant of H_2 oxidation for the next excitation period.

4.4.2 Slow Hole Transfer Regime in Photochemical H_2 Production

Prior work on photochemical H_2 production with CdS nanorods and H_2ase showed that product formation increased linearly with excitation over the range studied at that time, which was carried out at R_{exc} up to ~10^3 excitations/nanorod/sec (s^{-1}).[11] In this regime, QY remains constant. However, as excitation rate increases, we expect that at some point other steps will become slower than R_{exc}; here we explore a regime in which HT becomes the rate-limiting step. To capture this, we performed H_2 production experiments over a wider range of R_{exc}—up to 15x higher than in previous work by varying the intensity of the continuous wave (CW) light source.

Figure 4.4 shows experimentally measured photochemical H_2 production by a 2:1 nanorod:H_2ase molar ratio sample as a function of R_{exc} up to ~5 x 10^4 s^{-1} at three concentrations of the hole scavenger, Asc.[11] The highest Asc concentration shown (100 mM) is the amount used in typical H_2 production experiments with CdS nanorod-H_2ase complexes.[11,18]. In contrast to the linear H_2 production trend observed in prior work at R_{exc} up to ~3 x 10^3 s^{-1},[11] in this broader excitation rate regime we observe a saturation behavior where photochemical H_2 production is no longer linear with excitation rate for all three [Asc]. In other words, the QY decreases with excitation rate and the reaction is no longer in a photon-limited regime. We note that this excitation range is still several orders of magnitude below the R_{exc} at which double excitation and multiexciton recombination becomes relevant.[19,32–34] The lowest [Asc] deviates from linearity at lowest excitation rates, and the saturating amount of H_2 produced increases with increasing [Asc] as one might expect when HT is the rate-limiting step of product formation. Next, we use kMC simulations to guide our understanding of how slow HT impacts photochemical H_2 production, describe how fitting our experimental data with kMC simulations allows us to characterize HT rates, and how $\langle N_{cat} \rangle$ impacts H_2 production as a function of illumination intensity under slow HT conditions.

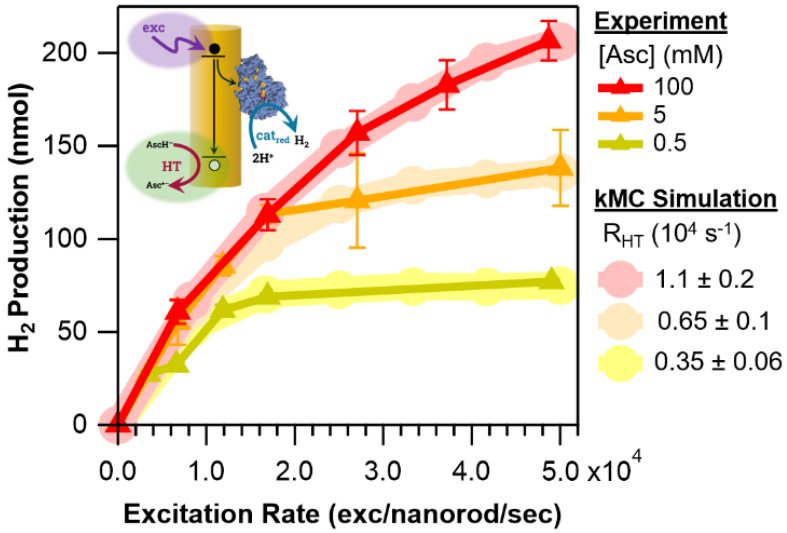

Figure 4.4: Experimental results and simulations of light-driven H_2 production rate of CdS nanorod-H_2ase at varying concentrations of sacrificial electron donor ascorbate (Asc). The two parameters being varied are the excitation rate (inset, purple) and the HT rate, R_{HT} (inset, green).

Figure 4.5 depicts kMC simulations of photochemical nanorod-H_2ase R_{H2} and QY, respectively, as a function of R_{exc} at varying $\langle N_{cat} \rangle$ values. The range of R_{exc} from 0 to 5 x 10^4 s^{-1} was chosen to be comparable to the calculated R_{exc} values for the experimental data from **Figure 4.4**. Let us now consider why slow HT conditions cause a decrease in QY with increasing R_{exc}. To examine the regimes of R_{HT} both faster and slower than R_{exc}, we fixed R_{HT} at 1 x 10^4 s^{-1} (**Figure 4.5,** vertical dashed line), which is 5x slower than the maximum R_{exc} simulated; this R_{HT} value also resembles our estimated R_{HT} at 100 mM Asc (as discussed below). In the low R_{exc} regime where $R_{exc} < R_{HT}$, we observe the photon-limited linear increase in R_{H2} **(Figure 4.5a**), where for each ET event a corresponding HT occurs prior to the next excitation, keeping QEET and thereby QY constant with increasing R_{exc} (**Figure 4.5b**). However, as R_{exc} overtakes R_{HT}, there will be instances where HT fails to remove the photoexcited hole from the nanorod prior to the next excitation, resulting in a photoexcited electron and *two* or more photoexcited holes in the nanorod. As mentioned in our kMC simulation description section above, each additional hole will multiply the probability of electron-hole recombination. This in turn will decrease QEET (Eqns 1 and 2)

and consequently QY (**Figure 4.5b**); this leads to saturation of R_{H2} at high R_{exc} (**Figure 4.5a**) as increasingly higher R_{exc}/R_{HT} ratios increase the steady state population of excess photoexcited holes in the nanorod. The onset of this non-photon-limited regime depends on R_{HT}; QY decreases at $R_{exc} > R_{HT}$ for all $\langle N_{cat} \rangle$ (**Figure 4.5b**). However, the rate of decrease in QY with increasing R_{exc} is influenced by R_{ET}, as evidenced by the H_2 production trends with varying $\langle N_{cat} \rangle$ (**Figure 4.5a**) (recall that increasing $\langle N_{cat} \rangle$ increases R_{ET} (Eqn 3)). Increasing R_{ET} increases the rate of decrease in QY because higher R_{ET}/R_{HT} ratios lead to greater buildup of excess photoexcited holes in the nanorod.

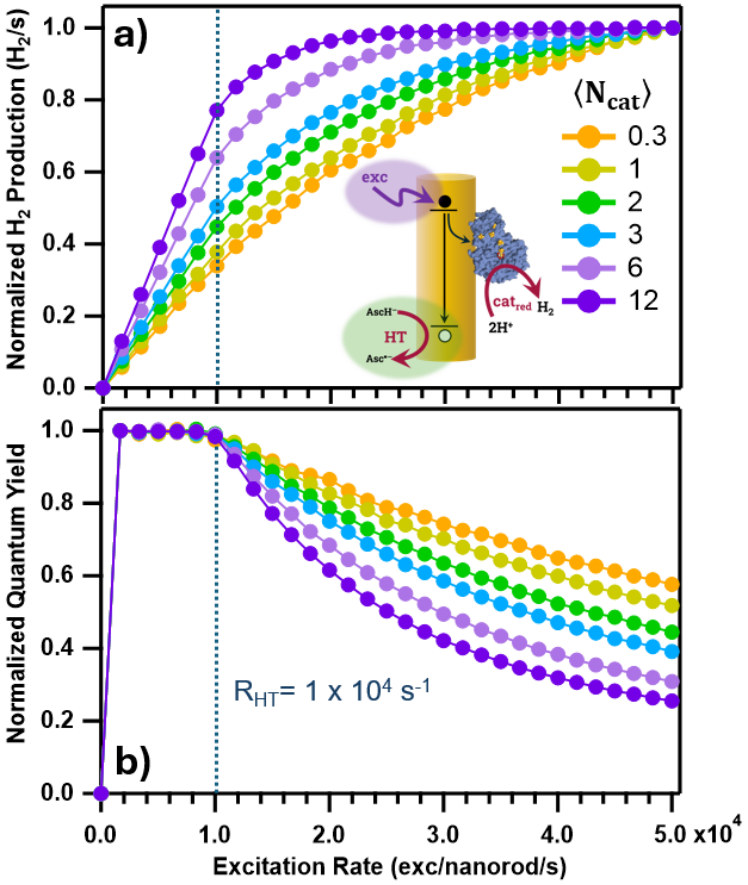

Figure 4.5: Simulation of a) R_{H2} and b) QY (both normalized at their maximum values) versus excitation rate at a range of $\langle N_{cat} \rangle$, at $R_{HT} = 1 \times 10^4\ s^{-1}$.

In principle, R_{HT} values can be determined directly from the data in **Figure 4.4** by finding the R_{exc} value at which the QY begins to decrease (as per **Figure 4.5b**). However, our data points are spaced such that directly reading off this point is somewhat imprecise. We therefore use kMC simulations to fit our experimental R_{exc} and [Asc] dependence of H_2 production from **Figure 4.4**, using the parameter inference software package pyABC as described in the Experimental Methods. The R_{HT} values that fit the data are on the order of 10^3 to 10^4 s^{-1} and higher [Asc] naturally leads to higher R_{HT}. This places us in a regime of R_{HT}/R_{exc} ~ 0.2 at our maximum experimental R_{exc}. Michaelis-Menten kinetic analysis of R_{HT} as a function of [Asc] suggests that by 100 mM Asc the R_{HT} has reached saturation at ~1 x 10^4 s^{-1} (**Figure 4.6**) and higher Asc concentrations would not lead to more H_2, consistent with prior experimental work.[11]

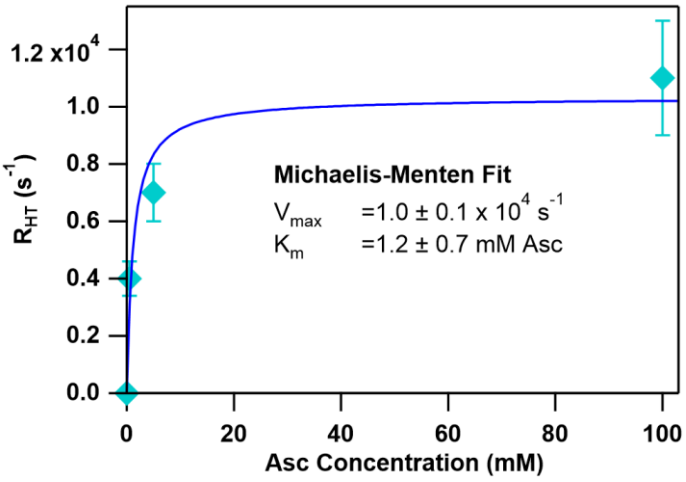

Figure 4.6: R_{HT} values obtained from fits of simulations to the experimental H_2 production data from Figure 3 in the main text, as a function of Asc concentration. The fit to the Michaelis-Menten equation $R_{HT} = V_{max}\cdot[Asc]/(K_m + [Asc])$ results in a V_{max} of 1.0 x 10^4 s^{-1} and K_m of 1.2 mM Asc. This K_m value agrees with prior work on the [Asc] dependence of photochemical H_2 production in CdS nanorod-H_2ase samples; the Km value on the order of ~1 mM is an indication of the high amounts of excess [Asc] needed relative to the 40 nM CdS nanorod concentration to achieve saturation of R_{HT}.[11] The V_{max} fit result suggests that by 100 mM Asc, R_{HT} has saturated.

The fits of the simulations to the data in **Figure 4.4** were fairly insensitive to the rate of catalyst turnover. Upon increasing $k_{cat,red}$ to essentially infinitely large values, the resulting R_{HT} values remained the same within error (**Figure 4.7**). However, the quality of the fit to the 100 mM Asc

data was marginally better at the lower $k_{cat,red}$; this may suggest we are at the precipice of a regime where the H_2ase turnover rate could also become rate-limiting. While the impact of $k_{cat,red}$ here is minimal, future studies or other systems involving enzymes with slower turnover rates may easily achieve a regime in which catalyst turnover is the primary rate-limiting step.

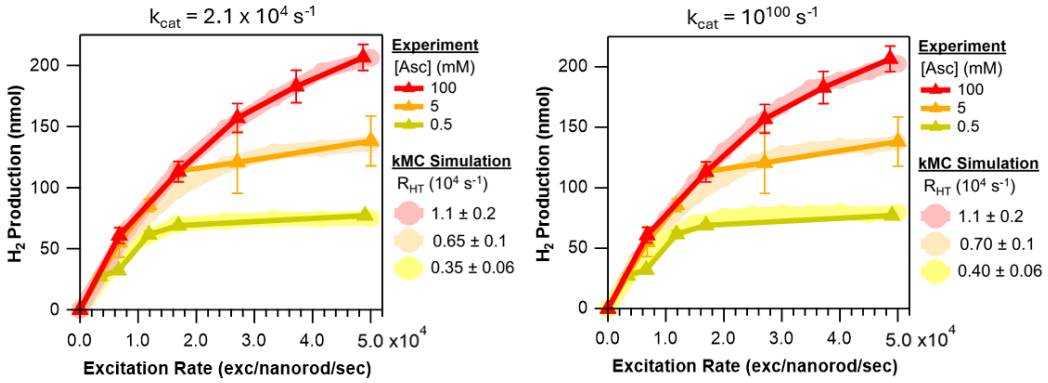

Figure 4.7: Fits of kMC simulations to experimental [Asc] and R_{exc} dependence data, where the value k_{cat} is a) 2.1 x 10^4 s^{-1} (this is the same fit as found in **Figure 4.4**), and b) essentially infinitely fast, set to 10^{100} s^{-1}.

We examine here what we might expect from a regime in which k_{cat} becomes rate-limiting. The analysis shows that low catalyst turnover impacts photochemical H_2 production differently than a slow HT rate. For this discussion it is useful to define R_{cat}, the total catalyst turnover rate per nanorod, as:

$$R_{cat} = \langle N_{cat} \rangle \cdot k_{cat} \quad (4)$$

After an H_2ase accumulates two electrons, if R_{cat} is sufficiently fast with respect to R_{exc}, then turnover (i.e. H_2 production) will occur prior to the next excitation, leaving $\langle N_{cat} \rangle$ and QEET (Eqn 2) unchanged over the duration of the experiment. With increasing R_{exc}, there will be instances where H_2ase turnover fails to happen before the next excitation. As a H_2ase accumulates electrons, eventually the enzyme is saturated and cannot accept further electrons until turnover occurs. The result is a decrease in $\langle N_{cat} \rangle$—and consequently, QEET (Eqn 2) and QY—with increasing R_{exc} (**Figure 4.8**). It should be noted that $\langle N_{cat} \rangle$ is therefore a parameter whose value may change over

the course of an experiment. As a result, it is useful here to define $\langle N_{cat} \rangle_{tot}$, the average number of *total* H_2ase bound—both saturated and unsaturated—which remains constant throughout the illumination duration. $\langle N_{cat} \rangle_{tot}$ then represents the upper limit of $\langle N_{cat} \rangle$, which determines R_{ET} (Eqn 3). In experiments, $\langle N_{cat} \rangle_{tot}$ is a function of the nanorod:H_2ase ratio. We assume here that H_2ase may accumulate up to 5 electrons before becoming saturated, if the active site and all iron-sulfur clusters in the electron transport chain become reduced (**Figure 4.8a, 4.8b**). We also simulated how the H_2 production trends would be affected by an enzyme which could accumulate only 2 electrons before becoming saturated (**Figure 4.8c, 4.8d**).

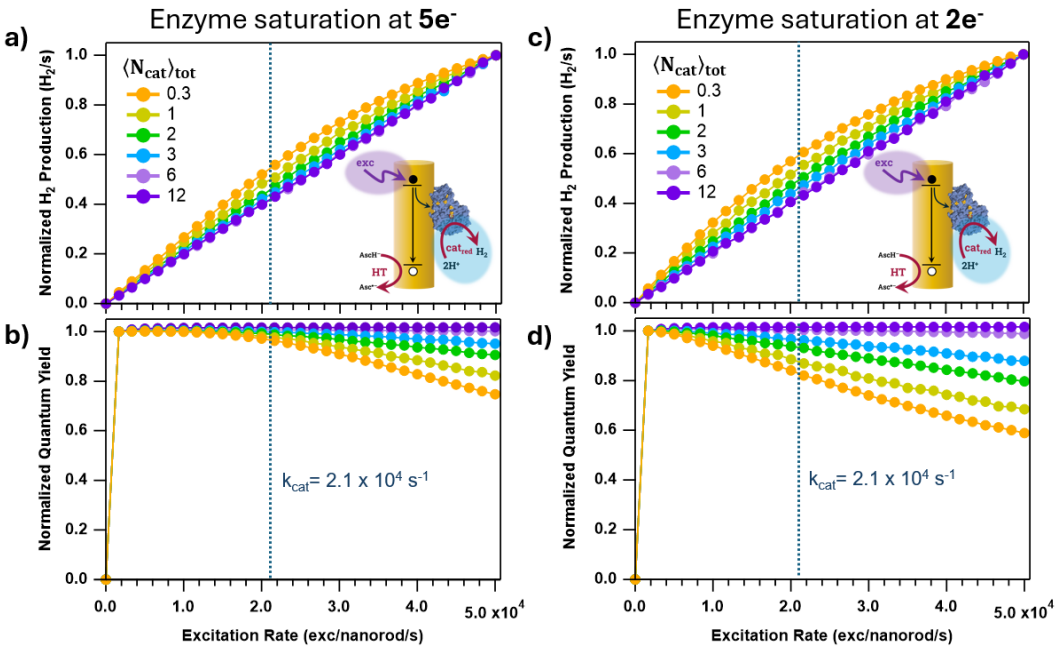

Figure 4.8: Simulations of H_2 production as a function of excitation rate and at varying $\langle N_{cat} \rangle_{tot}$ under conditions of slow catalyst turnover, depicting the resulting a), c) R_{H2} and b), d) QY, normalized at their maximum values. The trends in a) and b) depict the results when the enzyme can accumulate up to 5 electrons before becoming saturated, and the trends in c) and d) depict a system in which the enzyme can accumulate only 2 electrons.

We note that the fitting of the kMC simulation to the experimental data in **Figure 4.4** allows us to quantify HT rates in this system under catalytic turnover conditions, which have thus far proven elusive to measure. Quantifying R_{HT} provides precise information about the extent to

which slow HT impacts the photochemical outputs in this regime; for example, even at low $\langle N_{cat} \rangle$ = 0.3, slow HT would cause QY to decrease by over 40% within our R_{exc} range (**Figure 4.5b**). The significant impact of HT on photochemical H_2 production in this regime highlights the increase in R_{H2} and QY that would be achieved by even a modest increase in R_{HT} of less than an order of magnitude. Obtaining higher R_{HT} values in the experimental system is a nontrivial challenge. Significant changes would be necessary, either to improve the affinity of the hole scavenger for the nanocrystal surface (note the very low affinity of Asc in **Figure 4.6**), or to increase the rate constant of HT, both of which could increase R_{HT}. Strategies could include changes in hole scavenger structure, nanocrystal surface chemistry and electronic structure, solvent pH, ionic strength of the solution, etc. For the current system conditions, **Figure 4.5** demonstrates that $\langle N_{cat} \rangle$ is a readily available handle by which the H_2 production trend with R_{exc} can be controlled in the slow HT regime, as lower $\langle N_{cat} \rangle$ results in a more gradual decrease in QY. The $\langle N_{cat} \rangle$ dependence of the absolute values of R_{H2} and QY also warrant discussion; these trends, however, are complicated by BET and H_2 oxidation processes. We address these next.

4.4.3 Impacts of Back-Electron Transfer and H_2 Oxidation

In this section, we examine how two reverse photochemical pathways manifest in H_2 production trends for the nanorod-H_2ase system. The first is BET: the loss of an electron from H_2ase back to the nanorod or to elsewhere in solution. The second is H_2 oxidation—the reverse reaction of H_2 production—in which H_2ase is reduced by H_2, followed by BET.

When H_2 oxidation and/or BET pathways are present, QY will no longer equal QEET, as not all electrons transferred to the catalyst will contribute to net product formation. We expect that the impact of BET will be most apparent at high N_{cat} due to the multi-electron nature of H_2 production; all the enzymes bound to a single nanorod will compete for the same electrons,

increasing the waiting time between ETs for each enzyme. This increased time between ETs increases the likelihood of BET occurring prior to the next ET, leading to decreased QY at higher N_{cat}. The impact of BET will also depend on R_{exc}, because the waiting time between ET events decreases with increasing R_{exc}. Trends of decreased QY with higher catalyst loading have been experimentally demonstrated in prior nanorod-H_2ase H_2 production measurements and in other photochemical systems, suggesting that BET can play an important role.[11,35] The presence of H_2 oxidation in addition to BET will also decrease QY due to decreasing the net H_2 produced, but how the magnitude of its impact changes with increasing catalyst loading is less intuitive. It is therefore useful to better understand the relevance of BET and H_2 oxidation in our system and the extent to which each of these two processes impact CdS nanorod-H_2ase H_2 production, so that we may gain insight toward controlling the losses from these non-productive pathways.

First, we examine the effect of BET on photochemical H_2 production. To understand the trends in ensemble nanorod-H_2ase samples consisting of a distribution of N_{cat}, it is useful to first examine the H_2 production trends of individual N_{cat} values. Note that in experiments such as these where R_{exc} and illumination duration is kept constant, R_{H2} will exhibit the same normalized trends as the QY because under these conditions all samples absorb the same number of photons, and both R_{H2} and QY are based on the net H_2 produced. **Figure 4.9a** shows the results of a kMC simulation of the QY of photochemical H_2 production with increasing N_{cat} under varying values of the rate constant of BET (k_{BET}) relative to R_{exc}. We see that when BET is comparatively slow ($k_{BET}/R_{exc} < 0.001$), QY equals QEET (Eqn 1) for all values of N_{cat} because all the electrons transferred to H_2ase are used for catalysis. As BET becomes faster relative to excitation, QY decreases below QEET, because no longer do all the electrons transferred to H_2ase contribute to eventual H_2 production. The other key outcome is that the maximum QY shifts to favor lower

catalyst loading, eventually peaking at N_{cat} = 1, best seen in the normalized data (**Figure 4.9b**). This is the outcome predicted from our discussion above; since higher N_{cat} increases the waiting time between ETs for each H_2ase, at sufficiently high k_{BET}/R_{exc} increasing N_{cat} becomes detrimental rather than beneficial to the QY.

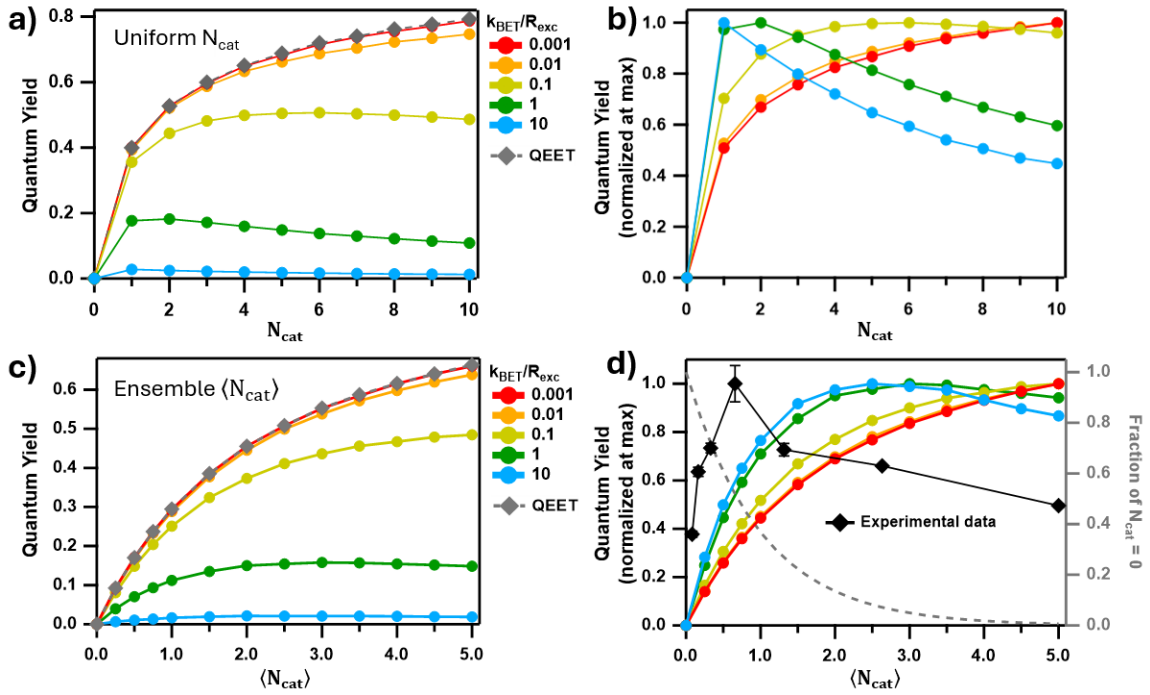

Figure 4.9: Simulated QY and QEET versus catalyst loading at a range of k_{BET}/R_{exc} values. Results from simulations of uniform N_{cat} samples are shown a) unnormalized and b) normalized at maximum N_{cat} for each trace. Results from simulations of ensemble $\langle N_{cat} \rangle$ samples, where N_{cat} follows a Poisson distribution are shown c) unnormalized and d) normalized at maximum $\langle N_{cat} \rangle$ for each trace. Prior experimental data is reprinted here with permission from Ref [11], copyright 2012, American Chemical Society. In d), the right hand axis shows the fraction of N_{cat} = 0 in the Poisson distribution as a function of $\langle N_{cat} \rangle$.

In **Figures 4.9c, 4.9d,** we plot the catalyst loading trends in ensemble samples consisting of a Poisson distribution of N_{cat}, each sample defined by an $\langle N_{cat} \rangle$; this allows us to compare our simulations to previous experimental data of photochemical H_2 production as a function of H_2ase:nanorod molar ratio from Brown et al. (**Figure 4.9d**).[11] We equate the experimental H_2ase:nanorod molar mixing ratio with $\langle N_{cat} \rangle$. BET from H_2ase to the nanorod may occur via two pathways: the electron may transfer back to the nanorod conduction band (BET-CB), or it may

recombine with a trapped hole on the nanorod surface (BET-tr). It is also conceivable that H_2ase might lose an electron to other components in solution (BET-soln)—we include this type of electron loss pathway in our definition of BET here as well. As none of these BET pathways has been previously directly observed nor its rate measured, we explored all three of these possibilities. The simulation results in **Figure 4.9** show the results of incorporating BET-soln, with which the QY peaked at the lowest $\langle N_{cat} \rangle$ of all three possible BET pathways at $\langle N_{cat} \rangle \sim 2$, best seen in the normalized traces (**Figure 4.9d**). When BET-tr or BET-CB were simulated as the BET pathway, the QY peak is shifted towards an even higher $\langle N_{cat} \rangle > 2$ as seen below in **Figure 4.10.** Regardless of which BET pathway is simulated, the ensemble QY does not peak at $\langle N_{cat} \rangle < 2$ because at these low $\langle N_{cat} \rangle$ values the ensemble will contain a significant fraction of nanorods with $N_{cat} = 0$, as per the Poisson distribution (**Figure 4.9d**, dashed line). The fraction of $N_{cat} = 0$ nanorods will contribute zero product formation and consequently lower the ensemble QY at low $\langle N_{cat} \rangle$. As a result, none of our simulated QY versus $\langle N_{cat} \rangle$ results with BET resemble the previously reported experimental results for H_2 production in the CdS nanorod-H_2ase system (**Figure 4.9d, 4.10**).[11] In the experimental trend, QY peaks at $\langle N_{cat} \rangle < 1$, and exhibits a much steeper QY drop off with increasing $\langle N_{cat} \rangle$ after the peak than the simulated results. This suggests that BET alone may not be sufficient to explain the experimentally measured H_2 production as a function of $\langle N_{cat} \rangle$.

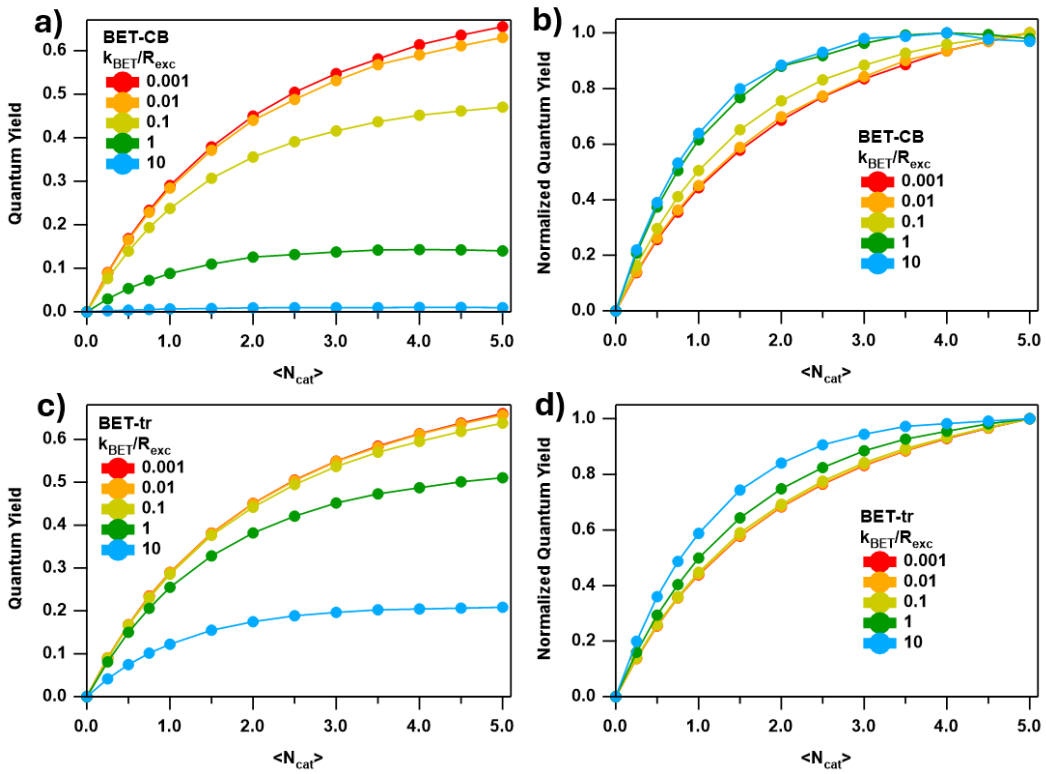

Figure 4.10: Simulated QY versus $\langle N_{cat} \rangle$ with BET-CB (unnormalized and (b) normalized at peak QY, and BET-tr (c) unnormalized and (d) normalized at peak QY.

We therefore turn to consider the additional impact of H_2 oxidation on the catalyst loading trend in H_2 production. The photochemical H_2 production experiments are done in a closed system where H_2 is allowed to accumulate; as such, sufficiently high H_2 production may eventually lead to H_2 oxidation by H_2ase due to its favorable binding affinity for H_2 as evidenced by its reported Michelis-Menten constant K_m = 1.7 mM.[36] Based on previously reported H_2 oxidation rates of this H_2ase using redox dyes as the electron acceptor (19,500 s^{-1}), we estimated the rate of H_2 oxidation under the experimental conditions for the previously reported H_2ase:nanorod molar ratio dependence shown in **Figure 4.9d**.[11,30] The below calculations were done for data from Brown et al. 2012 from Figures 3 and 4c of that work:[11]

Partial pressure of H_2 in assay vial headspace:

H_2 in headspace $= n = 470$ nmol (from the 1:0.67 nanorod:CaI molar ratio sample, Fig 3 Brown et al. JACS 2012)

$$Volume\ of\ headspace = V = 1\ mL$$

$$P_i = \frac{n}{V}RT = \left(\frac{470x10^{-9}mol}{0.001\ L}\right) \cdot \left(0.0821\frac{L \cdot atm}{mol \cdot K}\right) \cdot 295\ K = 0.0114\ atm$$

$$\boldsymbol{P_i = 0.0114\ atm}$$

Concentration of dissolved H_2 in assay solution:

$$C_{H2} = kP_i = \left(\frac{1}{1282}\frac{mol}{L \cdot atm}\right) \cdot 0.0114\ atm = \boldsymbol{8.9\ \mu M\ H_2}$$

Estimated turnover frequency (TOF) of H_2 oxidation by CaI:[30,36]

$$\boldsymbol{TOF_{H2\ oxidation}} = \frac{kcat \cdot [H_2]}{Km + [H_2]} = \frac{19{,}500s^{-1} \cdot 8.9\ \mu M\ H_2}{(1700 + 8.9)\ \mu M\ H_2}$$

$$\boldsymbol{TOF_{H2\ oxidation} = 100\ s^{-1}}$$

Compared to observed net TOF of H_2 production (from Fig 4c Brown et al. JACS 2012):

$$\boldsymbol{TOF_{H2\ production,net} = 120\ s^{-1}}$$

Estimated TOF of H_2 production by CaI:[11]

The net (i.e. experimentally measured) rate of H_2 production is the rate of H_2 produced minus the rate of H_2 oxidized:

$$\boldsymbol{TOF_{H2\ production,net} = TOF_{H2\ production} - TOF_{H2\ oxidation}}$$

$$\boldsymbol{TOF_{H2\ production} = TOF_{H2\ production,net} + TOF_{H2\ oxidation}}$$

$$\boldsymbol{TOF_{H2\ production} = 120\ s^{-1} + 100\ s^{-1}}$$

$$\boldsymbol{TOF_{H2\ production} = 220\ s^{-1}}$$

We found that under these conditions, the concentration of H_2 in solution ($[H_2]$) would be ~9 μM, at which H_2 oxidation could feasibly occur at rates comparable to photochemical H_2 production. To understand the impact of the presence of H_2 oxidation, we simulated photochemical H_2 production as a function of illumination time for different values of $\langle N_{cat} \rangle$ with and without H_2 oxidation, as shown in **Figures 4.11a** and **4.11b**. In **Figure 4.11a** with no H_2 oxidation, we see a constant linear accumulation of H_2 with the number of photons absorbed per nanorod (which is

equivalent to the illumination time). Here, the simulation assumes sufficient excess of all necessary components, such as the hole scavenger; prior work in which H_2 production was measured over longer duration demonstrated this to be a reasonable assumption.[11]

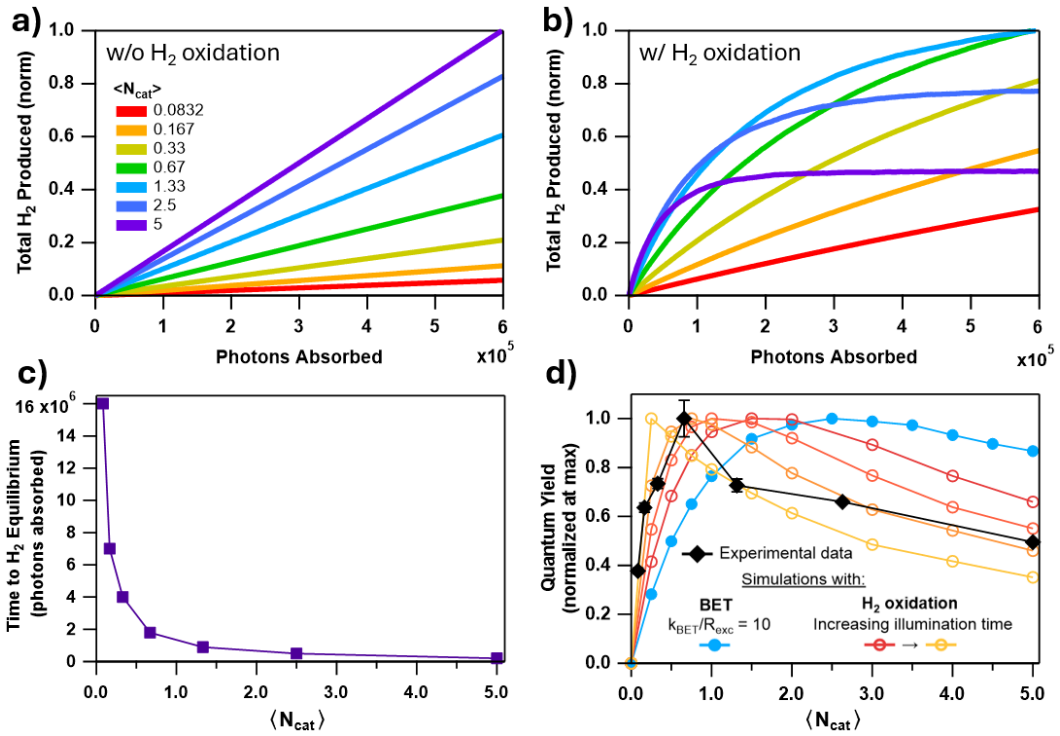

Figure 4.11: Simulated catalytic product formation versus photons absorbed at varying $\langle N_{cat} \rangle$ a) without H_2 oxidation and b) with H_2 oxidation present. c) The illumination time needed to reach H_2 production/oxidation equilibrium versus $\langle N_{cat} \rangle$.d) Comparison of experimental QY trend as a function of H_2ase:nanorod mixing ratio with simulations which include BET (the same k_{BET}/R_{exc} = 10 trace as shown in **Figure 4.9d**) or H_2 oxidation at varying illumination times from short times (red) to long times after H_2 has saturated at all $\langle N_{cat} \rangle$ (yellow). Prior experimental data is reprinted here with permission from Ref [11], copyright 2012, American Chemical Society.

In **Figure 4.11b,** we introduce the H_2 oxidation reaction into the simulation. We start with a relatively slow relative rate constant $k_{cat,ox}$ such that $k_{cat,ox}/R_{exc} = 0.001$, as this relative rate allows us to observe the impact of H_2 oxidation at reasonable simulation runtimes. As we will soon see, while the value of $k_{cat,ox}$ does impact how quickly (in terms of illumination time) H_2 oxidation takes effect, it does not impact the resulting trends with respect to $\langle N_{cat} \rangle$.

As mentioned above, we calculated that prior experimental samples accumulated [H_2] on the order of μM: this is three orders of magnitude smaller than the K_m of 1.7 mM. Following

Michaelis-Menten kinetics, in a regime where [H_2] is much lower than K_m, the rate of H_2 oxidation will be directly proportional to [H_2].[37] The rate of H_2 oxidation per nanorod ($R_{H2,ox}$) will therefore be governed by $k_{cat,ox}$, [H_2], and $\langle N_{cat} \rangle$ as shown by Eqn (5):

$$R_{H2,ox} \propto k_{cat,ox} \cdot [H_2] \cdot \langle N_{cat} \rangle. \quad (5)$$

As H_2 accumulates, the H_2 oxidation rate increases, slowing R_{H2}; eventually H_2 accumulation saturates as the system reaches an equilibrium between forward and back-reactions, after which point no further net H_2 is produced. As a result, although the initial R_{H2} increases with increasing $\langle N_{cat} \rangle$, after a certain illumination time has passed a crossover begins where higher $\langle N_{cat} \rangle$ values lead to less total H_2 accumulated because these samples reached the equilibrium earlier in the experiment (with fewer photons absorbed) and at lower H_2 concentrations. This trend with $\langle N_{cat} \rangle$ results from the fact that $\langle N_{cat} \rangle$ impacts the rates of H_2 production and H_2 oxidation differently; photochemical H_2 production is limited by QEET (Eqn 2), which begins to saturate at high $\langle N_{cat} \rangle$ (**Figure 4.9c**), while the rate of H_2 oxidation increases linearly with respect to $\langle N_{cat} \rangle$ (Eqn 5).

The number of excitations required to reach equilibrium can vary widely; **Figure 4.11c** demonstrates how $\langle N_{cat} \rangle$ in particular can significantly impact the time to equilibrium. This trend with respect to $\langle N_{cat} \rangle$ is the same regardless of the H_2 production and oxidation rates or the R_{exc}; in other words, a $\langle N_{cat} \rangle = 5$ sample will always reach equilibrium 20x faster than a sample at $\langle N_{cat} \rangle = 0.33$. The reaction rates involved will change the absolute times but not these times to equilibrium relative to $\langle N_{cat} \rangle$. Samples with higher $\langle N_{cat} \rangle$—and therefore higher QEET and faster initial R_{H2}—will more quickly accumulate sufficient H_2 for the back-reaction rate to compete against the forward reaction and reach equilibrium. The fact that $\langle N_{cat} \rangle$ can have such a drastic effect on the time to equilibrium demonstrates that even relatively low H_2 oxidation rates such as those simulated here could impact the H_2 versus $\langle N_{cat} \rangle$ trend. Another outcome of the varying

times to equilibrium is that the $\langle N_{cat} \rangle$ at which QY peaks will continue to change with illumination time until equilibrium has been reached for all $\langle N_{cat} \rangle$ (**Figure 4.11d**, red – yellow). As with the time to equilibrium trend with $\langle N_{cat} \rangle$, the same normalized QY versus $\langle N_{cat} \rangle$ trends occur regardless of the H_2 oxidation rate; the value of $k_{cat,ox}$ changes only the illumination duration at which that trend occurs. As **Figure 4.11d** demonstrates, the introduction of H_2 oxidation in the simulation brings the simulation results into closer quantitative agreement with the experimental data in a manner that the simulations with BET alone did not; with H_2 oxidation, the QY peaks at $\langle N_{cat} \rangle < 1$ and more closely resembles the slope of the post-peak QY drop-off in the experimental trend.

Having examined the effect of BET and H_2 oxidation on the CdS nanorod-H_2ase system, we can propose experimental handles by which their impact on photochemical H_2 production may be controlled. As seen in the simulation results in **Figure 4.9**, the effect of BET on H_2 production depends strongly on the relative photoexcitation rate. At $k_{BET}/R_{exc} < 0.001$, the impact of BET (regardless of the choice of BET pathway) on the QY is negligible. This illustrates the benefit of the light-driven system, as R_{exc} is a parameter which can theoretically be increased as high as desired, barring issues with sample stability. The limiting factor at very high R_{exc} would likely come down to the R_{HT}, as was discussed above. The impact of H_2 oxidation, meanwhile, is most effectively controlled by limiting the amount of H_2 that accumulates in solution. With continuous headspace flow, the rate of H_2 oxidation can be rendered insignificant. Alternatively, at low $\langle N_{cat} \rangle$ the time to H_2 equilibrium may be sufficiently long relative to the experiment duration that the impact of H_2 oxidation is negligible. As a result, it is feasible that through a combination of high excitation rates, careful selection of $\langle N_{cat} \rangle$, and continuous collection of the H_2 product as it

accumulates, the detrimental effects of BET and H_2 oxidation processes in CdS nanorod-H_2ase photochemical H_2 production may be effectively eliminated.

4.5 Summary and Conclusions

Many interdependent and competing parameters influence the rate and QY of nanocrystal-driven photochemical reactions; we explored these complex and interdependent kinetic relationships using a combination of kMC simulations and experimental measurements. We examined the trends of photochemical H_2 production of colloidal CdS nanorod-H_2ase complexes under conditions of slow HT, and the presence of BET and H_2 oxidation. Fitting simulations to experimental H_2 production data demonstrated that HT rates are on the order of 10^4 nanorod^{-1}s^{-1} with Asc as the hole scavenger. The saturation of H_2 production we observe at high excitation rates is due to HT that is ~5x slower than excitation; these results demonstrate that future work on improving HT rates could enable significant expansion of the photon-limited regime. If BET or H_2 oxidation are present, QY no longer trends with QEET, and QY peaks at lower catalyst loading. As such, the optimal $\langle N_{cat} \rangle$ for the highest QY depends on the prevalence of BET and H_2 oxidation. The peak and trend of the QY versus $\langle N_{cat} \rangle$ is heavily influenced by the distribution of nanorod-H_2ase complexes in the ensemble sample. Accounting for H_2 oxidation in the simulation generates an even more sharply peaked trend of QY versus catalyst loading which more closely resembles experimental results than with BET alone. The impact of BET and H_2 oxidation on QY can be lessened by use of a high photoexcitation rate, low $\langle N_{cat} \rangle$, and continuous H_2 collection during illumination. Overall, these trends provide a framework for identifying and controlling the limiting reactions under varying experimental conditions in semiconductor nanocrystal-enzyme photochemistry. More broadly, we provide a scaffold for understanding the role of elusive steps in complex photochemical reactions.

Chapter 5

Photocharging of Colloidal CdS Nanocrystals*

*Adapted with permission from Shulenberger, K. E., Keller, H. R., Pellows, L. M. Brown, N. L., Dukovic, G. Photocharging of Colloidal CdS Nanocrystals. J. Phys. Chem. C, 2021, 125 (41), 22650-22659. (Copyright © 2021 American Chemical Society)

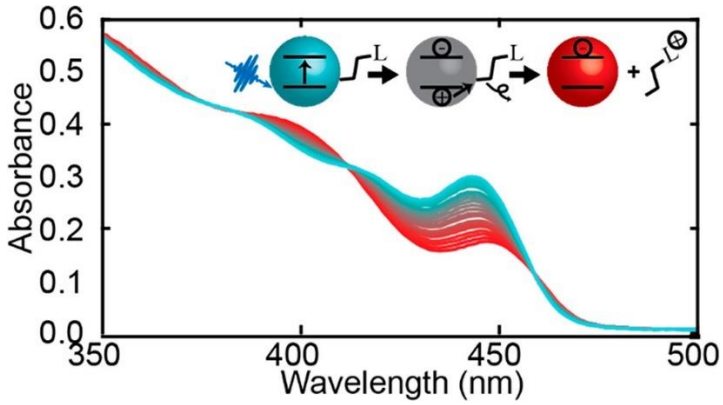

5.1 Abstract

Generation of reduced semiconductor nanocrystals is of interest for a variety of optoelectronic applications. In comparison to other nanocrystalline materials, little work has been reported on reduction of CdS nanocrystals, which are particularly interesting for solar photochemistry applications. Most nanocrystal reduction strategies require electron donors that reduce ground state or photoexcited nanocrystals. In this work, we report the discovery of photocharging of CdS nanocrystals under continuous wave illumination with no added reductants. The long-lived reduced states form under illumination, saturate at high concentrations, and recover over timescales of minutes when illumination stops. This process occurs in CdS nanocrystals of different sizes, morphologies, organic surface capping ligands, and in multiple solvents, but not in CdSe nanocrystals. We propose a charging mechanism in which the photoexcited holes oxidize surface-capping ligands, which then dissociate from the nanocrystal surface. We contrast this

ligand-mediated process with solvent-mediated photoreduction that occurs in CdS nanocrystals with polar ligands, which requires hole scavengers.

5.2 Introduction

The generation, storage, and manipulation of photoexcited charge carriers in semiconductor nanocrystals (NCs) have inspired a range of potential optoelectronic applications.[1–9] From transistors to photovoltaics and solar fuel generation, the understanding of not only bound electron-hole pairs (excitons), but also of isolated charge carriers is crucial for photon energy conversion in NCs. In particular, there has been long-standing interest in adding individual charges to NCs, which have historically been resistant to doping.[10–12] In recent years, charged states have been studied and characterized in a range of NC systems including ZnO,[13–21] CdSe,[22–28] CdSe/CdS,[29–31] PbS,[32] PbSe,[32–34] TiO_2,[35] In_2O_3,[36] InN,[37,38] HgTe,[39] HgS,[40] and Si.[41]

CdS NCs, in particular, have been of interest for applications in solar photochemistry, where photoexcited electrons transfer to catalysts (e.g., metal particles, molecules, enzymes) and holes are removed by electron donors.[42–46] Generation of long-lived reduced states in CdS NCs would enable high-efficiency electron transfer by drastically reducing the rates of competing pathways.[47–49] To date, there has been relatively little work on reducing CdS NCs, though chemical and photochemical methods have been developed to add excess electrons to analogous CdSe NCs.[22–24,27,28] The addition of electrons to CdSe NCs most often requires a chemical reductant, whether to directly reduce a ground state NC,[24,25,28] or to remove a photoexcited hole via electron transfer to the valence band.[22,23,27] Additionally, hot-hole mediated photocharging has been observed in CdSe/CdS core/shell quantum dots (QDs) through ligand oxidation and dissociation[30] and spontaneous photocharging has been observed by dissociation of methyl ligands from surface-modified CdSe QDs.[50] Photoreduction of CdS QDs has been observed using $Li[Et_3BH]$ as the

reductant[22,51] and, to the best of our knowledge, has not been seen without the assistance of external reductants.

In this manuscript, we describe photoreduction of CdS NCs capped with oleate and octadecylphosphonate (ODPA) ligands with no added electron donors, during illumination with a continuous wave (CW) 405 nm laser. The extent of charging is significant, with the majority of the NCs in the sample charged at saturation, but the accumulation of charged particles is reversible. The charged states are long-lived (minutes). The charging and recovery kinetics, as well as the extent of charging, depend on laser power, sample history, NC morphology, the surface-capping ligands, and the solvent. We observe no evidence of photocharging in similarly sized CdSe NCs. We propose a mechanism in which photoexcited holes transfer to surface-capping ligands, which then dissociate, leaving a long-lived negatively charged NC. In contrast, CdS NCs capped with 3-mercaptopropionate (MPA) show the characteristic charging signatures only when a solution electron donor is present, indicating that the ligand-dissociation mechanism is not dominant. We end with the discussion about the impact of the photocharging process described here on photophysics and photochemistry of CdS NCs.

5.3 Experimental Methods

5.3.1 Nanocrystal Sample Preparation

All NCs were synthesized via hot-injection procedures under inert argon atmosphere on a Schlenk line and transferred to an argon-filled glovebox for purification via precipitation by polar solvents such as methanol, ethanol, isopropanol, and acetone. Because alcohols have been shown to act as hole scavengers for CdS NCs,[52–55] albeit at high concentrations, care was taken to minimize alcohol content by drying the samples under vacuum after purification. Surface-capping ligand exchange procedures and sample preparation for spectroscopy experiments were also

carried out under air-free conditions in the same glovebox. Details of each synthesis and a summary of sample information can be found below.

5.3.2 Materials

Selenium (Se, 99.99%), sulfur (S, 99.998%), cadmium oxide (CdO, 99.99%), trioctylphosphine oxide (TOPO, 99%), oleic acid (90%), hexadecane (99%), ethanol (200 proof anhydrous >99.5%), toluene (anhydrous, 99.8%), methanol (anhydrous, 99.8%), isopropanol (anhydrous, 99.5%), hexane (mixture of isomers, anhydrous, >99%), chloroform (anhydrous, >99%, containing 0.5-1% ethanol as stabilizer), octylamine (99%), oleylamine (technical grade, 70%), acetone (HPLC grade, >99.9%), 1-octadecene (ODE, technical grade, 90%), tetrahydrofuran (inhibitor free HPLC grade, >99.9%), hexamethyldisilathiane (synthesis grade), and tributyl phosphine (97%) were obtained from Sigma-Aldrich. Tri-n-octylphosphine (TOP, 97%) was obtained from Strem. Octadecylphosphonic acid (ODPA) and n-hexylphosphonic acid (HPA) was obtained from PCI Synthesis. Tetramethylammonium hydroxide (TMAH, >97%) was obtained from Sigma Life Sciences. 3-mercaptopropronic acid (MPA, 99%) was obtained from Alfa Aesar.

5.3.3 Nanocrystal Syntheses

The table below summarizes the properties of each of the samples utilized in this study. Quantum dot (QD) samples were characterized based on the position of the first exciton peak, using established calibration curves to determine particle diameter.[56] The nanorod sample was characterized by its absorption spectrum and transmission electron microscopy images. Details on the material synthesis and purification for each sample are described in **Table 5.1** below.

Table 5.1: Summary of nanocrystal sample information.

Sample Name	Composition	Morphology	Ligand	First Exciton Peak (nm)	Dimensions[56] (nm)
S1-CdS-OA	CdS	QD	Oleate	443	5.0
S2-CdS-OA	CdS	QD	Oleate	444	5.0
S3-CdS-OA	CdS	QD	Oleate	393	3.2
S4-CdSNR-ODPA	CdS	Nanorod	ODPA	449	3.9 x 14
S5-CdSe-OA	CdSe	QD	Oleate	550	3.0
S6-CdSe-OA	CdSe	QD	Oleate	490	2.3
S7-CdSe-ODPA	CdSe	QD	ODPA	566	3.4
S2-CdS-MPA	CdS	QD	MPA	444	5.0

CdS-oleate QD synthesis

5.0 nm diameter CdS QDs capped with oleate ligands were synthesized using a multi-injection method reported previously.[57] Briefly, all synthesis procedures were performed under inert argon atmosphere either on a Schlenk line or in a glovebox. Two batches of 5.0 nm diameter CdS QDs were produced and used in experiments, designated as S1-CdS-OA and S2-CdS-OA: S1 (depicted in **Figures 5.2, 5.6,** and **5.8**) used ODE while S2 (**Figures 5.12** and **5.13**) used hexadecane as the main solvent in the precursors and reaction mixture. Hexadecane was substituted for ODE in S2 to test whether the possible presence of residual poly-ODE[58] does not change the observed photocharging effect (it does not). The sulfur precursor was prepared by dissolving sulfur (0.029 g) in ODE (7.1 g) or hexadecane (7.0 g) to generate a 0.1 M solution overnight. The 0.1 M Cd-oleate precursor was prepared in a 3-neck round-bottom flask fitted with a reflux condenser. The flask was prepared with CdO (0.128 g), oleic acid (2.82 g) and ODE (5.40 g) or hexadecane (5.27 g) and evacuated at 90°C (S1) or 80°C (S2) for 30 minutes. Under argon,

the precursor solution was then heated to 250°C (S1) or 240°C (S2). After the precursor solution turned clear, it was cooled to 60°C to prepare for injections. The main reaction mixture was prepared in a second flask with reflux condenser, to which 2.37 g ODE or 2.31 g hexadecane was added and evacuated at 90°C (S1) or 80°C (S2) for 30 minutes. Under argon, 4 mL of Cd-oleate precursor solution was transferred to the main reaction flask, and the mixture was heated to 260°C (S1) or 240°C (S2) and 2 mL of the sulfur precursor was injected. The reaction mixture temperature was maintained close to 220°C for the remaining injections. Three minutes after the first sulfur injection, 0.5 mL of Cd-oleate precursor was injected, all subsequent injections were performed at one-minute intervals. The remaining injection procedure for each synthesis was as follows. S1: Eight additional 0.5 mL injections were carried out, alternating sulfur and Cd-oleate, ending with a Cd-oleate injection. The mixture was then given one final minute of growth time before being quenched via cooling in a mineral oil bath and transferred to an argon-filled scintillation vial to be pumped into an argon-atmosphere glovebox for purification steps. S2: Ten additional 0.5 mL injections were carried out, alternating sulfur and Cd-oleate, ending with a Cd-oleate injection. The mixture was then given two final minutes of growth time before being quenched via cooling in a mineral oil bath and transferred to an argon-filled scintillation vial to be pumped into an argon-atmosphere glovebox for purification steps.

S1-CdS-OA purification: The initial crude nanocrystal mixture was precipitated with a 3:1 v/v ratio of methanol:isopropanol by volume and centrifuged. The clear supernatant was discarded, leaving a liquid pellet. Three more washing steps (3:1 v/v isopropanol: methanol, 1:1 v/v isopropanol:methanol, and 3:1 v/v acetone:methanol) were conducted to remove residual ODE until a solid pellet formed. The pellet was redispersed in toluene, and precipitated a final time with

a 5:1 acetone:methanol mixture, centrifuged, the supernatant discarded, and the pellet dried under vacuum and redispersed in toluene.

S2-CdS-OA purification: The initial crude nanocrystal mixture was precipitated with a 1:1 v/v ratio of methanol:isopropanol and centrifuged. Clear supernatant was discarded, the nanocrystal pellet was redispersed in hexanes, and this washing process was repeated multiple times until no more brown, grease-like waste material was observed. Prior to the final precipitation step, the nanocrystal stock was divided into multiple aliquots. The nanocrystal pellet in each aliquot was dried under vacuum and stored under inert argon conditions until the day of its use in photocharging experiments when it was redispersed in the final solvent (hexanes, toluene, tetrahydrofuran, or chloroform).

3.2 nm diameter CdS QDs capped with oleate ligands (S3-CdS-OA; **Figure 5.13a**) were synthesized using a single-injection method adapted from a previously published procedure.[59] All procedures were performed under inert argon atmosphere either on a Schlenk line or in a glovebox. The sulfur precursor was prepared by dissolving sulfur (0.0016 g) in ODE (1.58 g) to generate a 0.02 M solution overnight. The 0.02 M Cd-oleate precursor was prepared in a 3-neck round-bottom flask fitted with a reflux condenser. The flask was prepared with CdO (0.0128 g), Oleic Acid (0.200 g) and ODE (3.84 g) and evacuated at 90°C for 30 minutes. Under argon, the reaction mixture was then heated to 300°C until it turned clear. The mixture was cooled to 260°C, injected with the Cd-oleate precursor, and thereafter the temperature was maintained at 250°C for 3 minutes of growth. The nanocrystal growth was then quenched via cooling the flask in a mineral oil bath and transferred to an argon-filled scintillation vial for pumping into an argon-atmosphere glovebox for purification. The nanocrystals were precipitated with methanol, centrifuged, and the clear supernatant was discarded. The nanocrystal pellet was redispersed in toluene, and these

precipitation/centrifugation steps were repeated using a chloroform/methanol precipitation mixture until the nanocrystal solution was optically clear in toluene. The final CdS-OA-S3 stock solution was redispersed in <1 mL toluene.

CdS-ODPA nanorod synthesis

CdS nanorods capped with ODPA ligands (S4-CdSNR-ODPA; **Figure 5.12d, e, f, Figure 5.1b** were synthesized via an adaptation of previously reported procedures.[60] The synthesis and purification were carried out under an inert argon atmosphere using a Schlenk line or glovebox. The sulfur precursor containing 0.058 g sulfur and 0.89 g TOP was prepared under inert argon atmosphere one day in advance of the synthesis. The reaction mixture containing 0.06 g CdO, 0.280 g ODPA, and 3.01 g TOPO was prepared in a 25 mL 3-neck round-bottom flask fitted with a reflux condenser. The reaction mixture was heated to 150°C and evacuated for one hour. Under argon, the solution was heated to 300°C and 1.5 mL TOP was transferred to the reaction mixture. The mixture was cooled to 290°C before injection of the sulfur precursor. After the first five minutes of growth, the reaction mixture was brought to 300°C for the remaining growth time of approximately 20 minutes. The reaction was finally quenched by cooling the flask in a mineral oil bath. At 60°C, a 1:1 v/v methanol:toluene solution was added to the reaction mixture and the entire solution was transferred via syringe to an argon-filled scintillation vial and brought into an argon-filled glovebox for subsequent purification steps. The mixture was centrifuged, and supernatant discarded while the nanocrystal pellet was redispersed in a 5:2 volume ratio of toluene to octylamine. The nanocrystals were precipitated with methanol, centrifuged, and this redispersal/precipitation step was repeated one additional time. The final CdS nanorod pellet was dried under vacuum before being redispersed in anhydrous toluene (~2.5 mL). The average rod

dimensions of 14 +/- 2.2 nm length and 3.9 +/- 0.5 nm width were determined using transmission electron microscopy (**Figure 5.1**) to measure particles.

CdSe-oleate QD synthesis

3.0 and 2.3 nm diameter CdSe QDs capped with oleate ligands (S5-CdSe-OA, S6-CdSe-OA; **Figure 5.13b, c**) were synthesized via adaptation of a previously reported procedure.[61] The syntheses and purification were performed under inert argon atmosphere on a Schlenk line or glovebox. The 3.0 nm CdSe QDs (designated S6-CdSe-OA) were synthesized using ODE as the main solvent, while the 2.3 nm CdSe QD (designated S7-CdSe-OA) synthesis used hexadecane to avoid the formation of poly-ODE as recommended by a recent study.[58] For both syntheses, the 0.07 M Se precursor was prepared two days in advance of the synthesis, with typical amounts 0.030 g Se, 0.230 g TOP, and 2.696 g hexadecane. The reaction mixture was prepared in a 3-neck round-bottom flask fitted with a reflux condenser, with 0.014 g CdO, 0.55 g oleic acid, and 7.73 g hexadecane. The reaction mixture was evacuated for 40 minutes at 110°C. Under argon, the mixture was heated to 225°C (S6) or 200°C (S7) and 1 mL of Se precursor was injected. After 2.5 minutes (S6) or 10 seconds (S7) of growth, the reaction mixture was quenched by cooling in a mineral oil bath. The crude nanocrystal solution was transferred to an argon-filled scintillation vial containing a 1:2 v/v ratio of hexanes:ethanol by volume and pumped into the glovebox. Additional ethanol and methanol was added to precipitate the nanocrystals, which were then centrifuged. The supernatant was discarded, and the nanocrystal pellet was dried under vacuum before final redispersal in toluene (<1 mL).

CdSe-ODPA QD synthesis

3.4 nm CdSe QDs capped with ODPA ligands (S7-CdSe-ODPA; **Figure 5.16**) were synthesized using an adaptation of a previously reported procedure.[60] The synthesis and

purification were carried out under inert argon atmosphere on a Schlenk line or glovebox. The 1.7 M Se precursor was prepared two days in advance of the synthesis with 0.058 g selenium and 0.36 g TOP. The reaction mixture was prepared in a 3-neck round-bottom flask fitted with a reflux condenser, with 0.06 g CdO, 0.28 g ODPA, and 3.0 g TOPO. The reaction mixture was evacuated at 150°C for one hour. Under argon, the mixture was heated to 300°C and 1.5 mL TOP was injected. The mixture was then heated to 310°C and the Se precursor was injected. After 30 seconds of growth, the reaction was quenched by cooling the flask in a mineral oil bath. At 60°C, a 1:1 v/v methanol:toluene by volume solution was injected to the crude nanocrystal solution and transferred to an argon-filled scintillation vial to be pumped into the glovebox for purification. The mixture was centrifuged, and supernatant discarded while the nanocrystal pellet was redispersed in a 1:1 v/v ratio of hexane to octylamine. The nanocrystals were precipitated with methanol, centrifuged, and this redispersal/precipitation step was repeated one additional time. The final CdSe pellet was dried under vacuum before being redispersed in anhydrous toluene (<1 mL).

Ligand exchange to MPA (S2-CdS-MPA, **Figure 5.17, 5.18**). One S2-CdS-OA aliquot was designated for exchange of the native oleate for MPA ligands using a variation on previously reported method.[52,62] A 71 mM MPA stock solution was prepared with 15.0 g methanol, 0.143 g MPA, and 0.448 g tetramethylammonium hydroxide to adjust the pH to 11. The dried pellet of S2 CdS QD was redispersed in a minimal volume of toluene (<1 mL) and 300 uL of the MPA stock solution was added, causing the nanocrystals to precipitate briefly before quickly turning optically clear as the ligand exchange occurred. The newly-exchanged nanocrystal solution was divided into multiple aliquots, each of which was precipitated with toluene and centrifuged. The supernatants were discarded and each S2 CdS QD-MPA pellet was dried under vacuum and stored under argon

until its use in photocharging experiments when it was redispersed in the final solvent (formamide, ethanol, methanol, or 41 mM pH 6.8 MES-HEPES-TAPS buffer).

5.3.4 Nanocrystal Characterization

Transmission electron micrograph images of CdS QD (**Figure 5.1a**) and nanorod (**Figure 5.1b**) samples were obtained on a Tecnai ST20 at 200 kV with a LaB6 electron gun and 2k x 2k BM-Orius CCD camera mounted underneath. Dilute NC samples were dropped onto an Electron Microscopy Sciences 300 mesh carbon-coated copper grid for the CdS nanorods (S4-CdSNR-ODPA, Table S1), and a Ted Pella Inc. 400 mesh ultrathin carbon film on lacey carbon support film copper grid for the CdS QDs (S1-CdS-OA, Table S1). ImageJ software[63] was used to process the images.

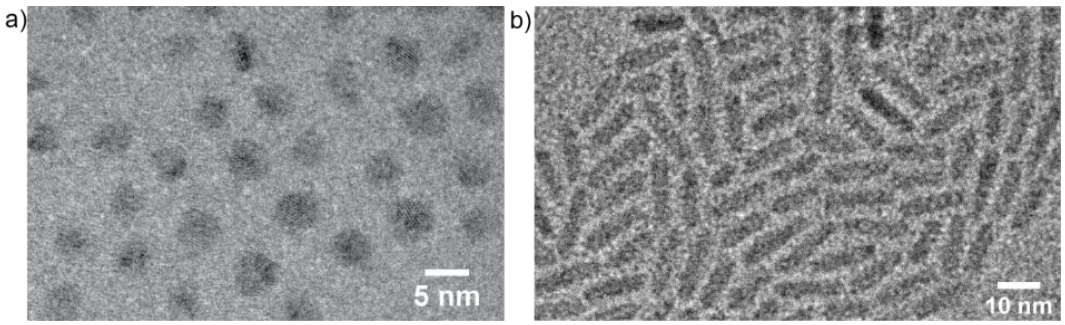

Figure 5.1: Transmission electron micrograph of a) the 5.0 nm CdS QDs (S1-CdS-OA) used to collect data in Figures 1, 2, and 3 and b) the CdS nanorods (S4-CdSNR-ODPA) used to collect data in Figure 5.12d-f.

5.3.5 Spectroscopy Experiments

All spectroscopy experiments were conducted in 1 cm UV-enhanced quartz cuvettes (Spectrocell) retrofitted with Kontes valves to ensure samples remained air-free. Samples were prepared in a glovebox under argon atmosphere with O_2 and water concentrations of less than 10 and 5 ppm, respectively. Photoexcitation of samples was performed using a collimated 405 nm tunable power CW diode laser (Laserglow Technologies, LRD-0405-PFR) with a 1 mm beam diameter. For the experiments presented in main text **Figures 5.2, 5.6, 5.8 and 5.13**, the excitation

power was 2.3 W/cm^2. In **Figures 5.12 and 5.17**, the CdS-oleate and CdS-MPA samples were excited at 1.9 W/cm^2, and the CdSNR-ODPA sample was excited at 1.4 W/cm^2.

UV-vis Absorption: Absorption data were collected using a Cary 60 UV-Vis Spectrophotometer (Agilent) in either spectral or kinetic mode. Experiments were conducted with the photocharging laser at 90° incidence angle during measurement. Samples were stirred continuously during absorption measurements with a magnetic Teflon stir bar.

Steady-State Photoluminescence: Steady-state photoluminescence (PL) spectra were collected using a Fluorolog-3 spectrofluorometer (Horiba Jobin Yvon) excited at 350 nm (3 nm slit width). PL was detected at a 90° angle with respect to excitation from 365-680 nm (3 nm slit width). Illumination for photocharging was performed outside the fluorimeter using the same 405 nm CW excitation source as the absorption measurements and samples were immediately transferred to the fluorimeter (<10 seconds) for the measurement. Samples were stirred with a magnetic Teflon stir bar during illumination.

Time Correlated Single Photon Counting: Time resolved PL data was collected using a DeltaFlex Modular Fluorescence Lifetime System (Horiba Scientific). The sample was excited by a NanoLED (Horiba, 402 nm) operated with a repetition rate of 1 MHz. Data was collected over the first 200 ns at a peak wavelength of 452 ± 16 nm for a total integration time of 5 minutes. Similar to the steady-state PL experiments above, sample excitation for photocharging was performed outside the instrument and samples were transferred immediately to perform measurements.

Both steady-state and time-resolved PL experiments were conducted on sample S1-CdS-OA (Table S1). Since our PL instruments do not allow for concurrent illumination with the 405 nm CW laser during measurement, QD samples with slow post-charging recovery were required

to avoid sample changes during the PL data collection. This was achieved by using "aged" (stored under Argon for 6 days after dilution) samples for the PL measurements, which show slower absorption recovery kinetics than the same samples when freshly diluted, as discussed in Section 3.2. Although the recovery kinetics of this six-day aged sample were slowed, there was no corresponding change in the absorption spectrum between days 1 and 6.

Transient Absorption: The transient absorption data was collected using an instrument described previously.[64] Briefly, both the pump and probe beam were derived from a 1 kHz Ti:sapphire oscillator with ~150 fs temporal width output at 800 nm (Solstice-ACE, Spectra Physics). The output was split with part being directed into an optical parametric amplifier (TOPAS-C, Light Conversion) which was tuned to 342 nm. The probe beam was generated by focusing the rest of the 800nm oscillator output into a sapphire plate. Transient absorption data were collected using a Helios transient absorption instrument (Ultrafast Systems, LLC). Samples were sealed in a 2 mm quartz cuvette fitted with a Kontes valve to remain air-free. Samples were stirred with a magnetic Teflon stir bar throughout data collection.

5.4 Results and Discussion

5.4.1 Photocharging in CdS NCs

We start our discussion by presenting the evidence for photocharging in CdS QDs. **Figure 5.2a** presents the steady state absorption spectrum of a representative sample of colloidal oleate-capped CdS QDs with 5.0 nm diameters. A transmission electron micrograph of these QDs is shown in **Figure 5.1**. The sample was prepared and studied under rigorous air-free conditions, as detailed in the Experimental Methods section. Upon illumination with a 405 nm CW laser, the absorption spectrum undergoes significant changes, most notably a decrease in intensity around the band-edge excitonic feature (**Figure 5.2a**). There is also a red-shift of the band-gap exciton

peak and an increase in intensity around 400 nm. The spectral changes due to illumination are detailed and assigned in the next paragraph. Similar changes were previously seen for CdS QDs when Li[Et_3BH] was used as a reductant.[51] After illumination is halted, we observe a slow recovery of the original band-edge absorbance over ~10 minutes (**Figure 5.2b**). In addition to the transient, light-induced spectral changes that are reversed during the recovery period, there is a ~4% reduction in absorption at all wavelengths in the recovered sample compared to the original sample, which we attribute to precipitation of a small fraction of QDs upon illumination (**Figure 5.3**). This loss is only observed in this sample after the first cycle of charging and recovery and not subsequent ones.

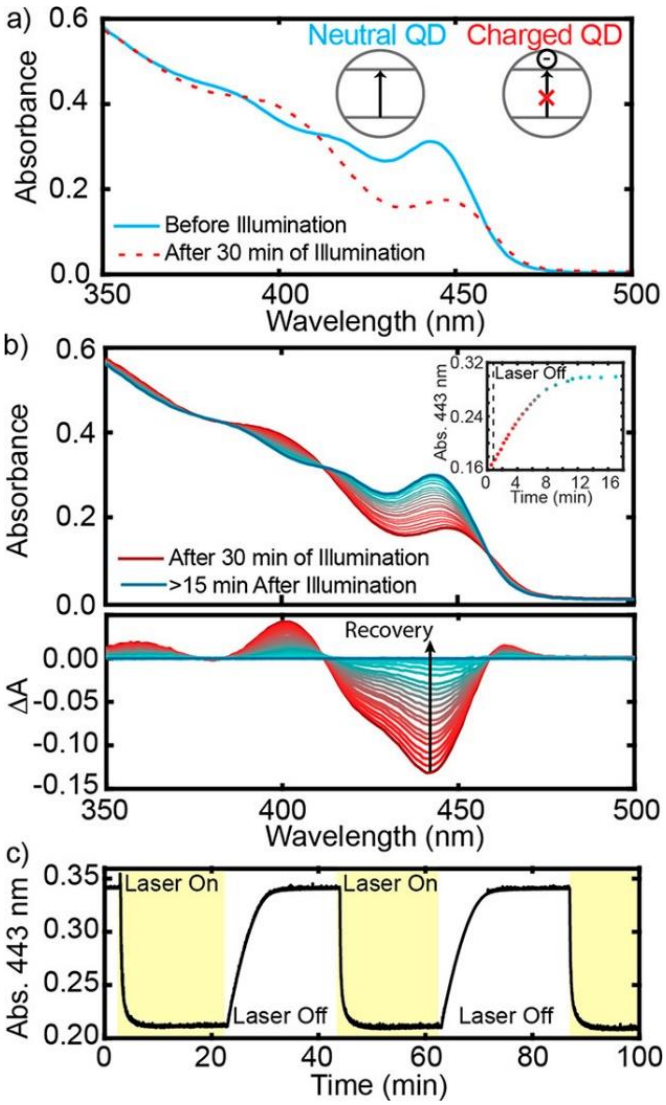

Figure 5.2: a) Absorption spectra of a solution of 5.0 nm oleate-capped CdS QDs in toluene before illumination and after ~30 minutes of illumination. The inset represents the proposed states for the charged and neutral state, in which the arrows represent photon absorption in the QD. **b)** *Top*: Absorption spectra of 5.0 nm oleate-capped CdS QDs during a >15 minute period after the laser is turned off. The inset shows the absorbance at the band-edge (443 nm) of each spectrum, and the corresponding time at which the spectrum was taken. The dashed line corresponds to when illumination was halted. *Bottom:* The corresponding ΔA (absorption minus absorption of the fully recovered sample) spectrum for each steady state spectrum from the panel above. **c)** Kinetic traces of the band-edge absorption (443 nm) through three illumination and recovery cycles. Time periods of sample illumination are highlighted in yellow.

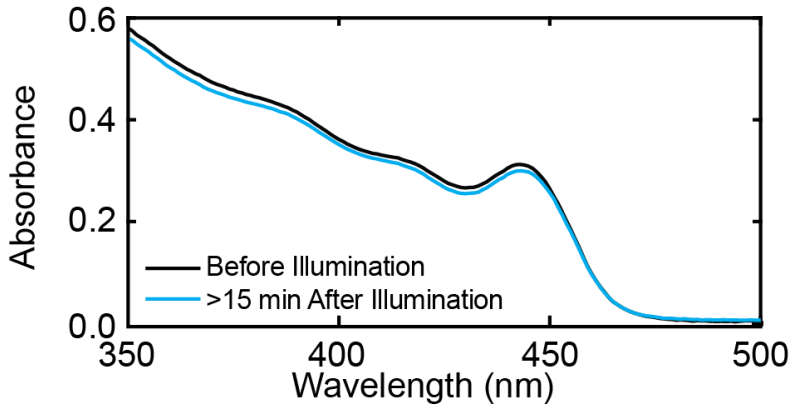

Figure 5.3: Absorption spectra of the QD sample shown in Figure 1 before illumination and >15 minutes after illumination was halted and the absorbance had fully recovered.

To examine the spectral changes due to illumination and recovery, we determine the change in absorbance due to illumination, abbreviated as ΔA, by subtracting the fully recovered spectrum from each spectrum during recovery (**Figure 5.2b, bottom**). This ΔA signal is not to be confused with the ΔA spectra obtained in transient absorption (TA) measurements, although, as we describe below, they happen to overlap in our case. The ΔA spectra in **Figure 5.2b, bottom**, show well-known spectral features of Cd-chalcogenide NCs with one electron in the conduction band. The most prominent is a strong band-edge bleach of two exciton states due to state filling of the $1S_e$ electron state (peaks at 423 and 441 nm). The induced absorption on the red edge (463 nm) is due to the trion binding energy, which shifts the 1S state slightly lower in energy. The presence of an excess electron in the $1S_e$ state also shifts higher energy states (such as the 1P state seen at 400 nm), resulting in absorbance changes at higher energy.[49,65,66] Similarly shaped ΔA spectra have been previously observed for photochemically reduced CdSe QDs.[22,23,50,67] As a clear indication that illumination leads to formation of reduced CdS QDs with electrons at the lowest-energy conduction band state, the ΔA spectra in **Figure 5.2b,** bottom, overlap the TA spectrum of the same NCs at 3 ns after excitation (**Figure 5.4**). At a pump-probe delay of 3 ns, hot carriers have relaxed to the band-edge and all multicarrier states have recombined, leaving a single exciton

at the band-edge.[68–70] Since TA spectra of core-only CdS QDs report only on the presence of photoexcited electrons,[71–73] the correspondence between the ΔA spectra from the steady state absorbance data and the TA spectrum confirms that the changes in the steady state absorption spectra of CdS QDs upon illumination (**Figure 5.2a**) are due to one-electron reduced QDs. Furthermore, when the ΔA spectra are normalized at the band-edge bleach peak, the spectral shape appears unchanged throughout recovery (**Figure 5.5**), suggesting there is only one (singly-charged) type of photogenerated state, rather than a range of (multiply-charged) states.

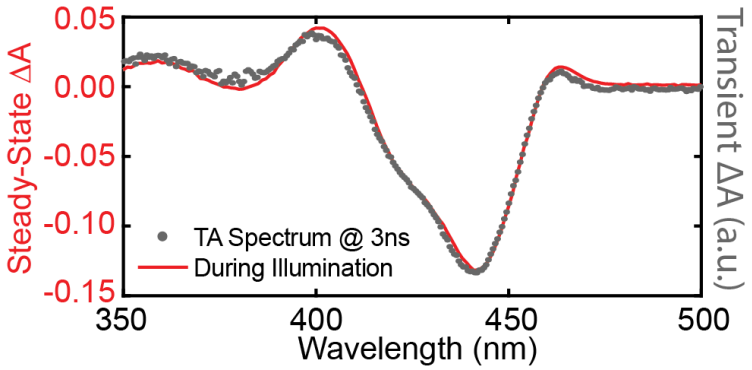

Figure 5.4: Comparison of the steady state difference spectrum between the fully charged (saturated) and fully recovered with a transient absorption spectrum taken 3 ns after excitation of the same 5.0 nm CdS QD sample (S1-CdS-OA).

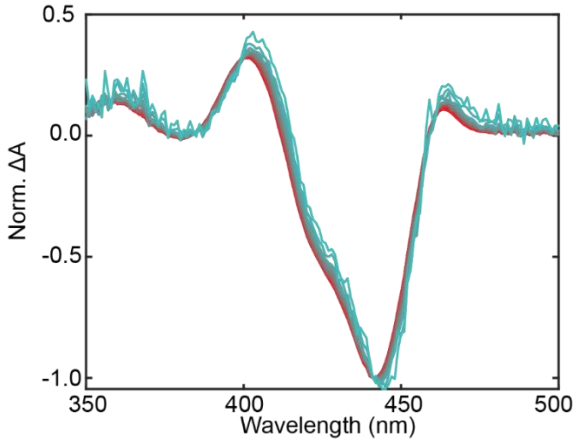

Figure 5.5: The same ΔA data as plotted in **Figure 5.2b**, but normalized at the bleach maximum at 448 nm. Magenta represents the fully charged spectrum, and blue the fully recovered. The last few spectra are omitted for clarity due to low signal to noise ratio of ΔA for nearly fully recovered QDs. The normalized spectra show that the spectral shape remains the same throughout recovery.

The photoreduction that we observe in CdS QDs is reversible over multiple cycles without the use of chemical electron scavengers. In **Figure 5.2c,** we show the kinetics of photocharging and recovery measured by monitoring the absorption at the lowest-energy absorption peak (443 nm). During laser illumination, this absorption rapidly decreases as the sample builds up negatively charged particles and, within a few minutes, saturates. After illumination is halted, the absorption recovers over the course of a few minutes, indicating that the reduced QDs are long-lived.

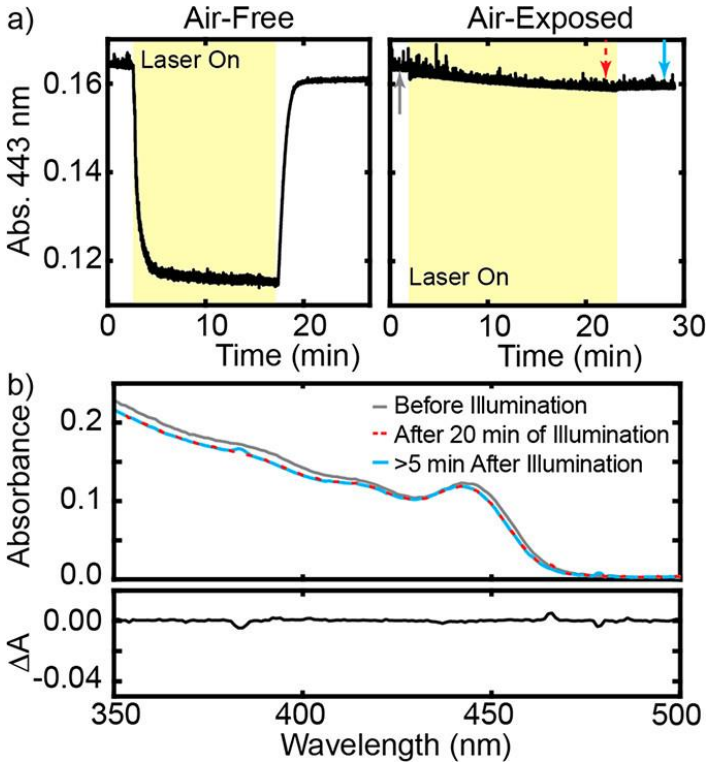

Figure 5.6: a) Kinetics of the band-edge absorbance of 5.0 nm QDs under air-free conditions (left) and exposed to air (right) through one illumination cycle. The highlighted regions correspond to the times the sample was illuminated. The arrows in the kinetic trace mark times at which steady state absorbance spectra were collected. **b)** *Top:* The absorbance spectrum from the air-exposed sample at the approximate times marked on the kinetic trace before, during, and after illumination. *Bottom:* The difference between the blue and red traces. These data show that the absorption spectra of the QDs do not reversibly change with illumination under air.

The observation of photocharging in CdS QDs requires rigorous air-free conditions. Previous reports have shown that oxygen is an effective quenching agent for negatively charged CdSe NC

systems.[22,24,25,67] **Figures 5.6a** and **5.6b** show that upon exposure to air, the same CdS QDs show none of the photoinduced absorbance changes—neither the characteristic ΔA nor the reversibility of the band edge absorbance loss—that were observed under air-free conditions (**Figure 5.2a-c**). We conclude that the O_2 in the air rapidly scavenges the electrons from photocharged CdS QDs, leading to no accumulation of the charged state.

We determine the maximum fraction of charged QDs from UV-vis absorption spectra using previously established methods[22,25,26,74] where

$$< n >_{max} = \frac{2(A_0 - A_S)}{A_0}. \quad (1)$$

Here $<n>_{max}$ represents the fraction of charged particles at saturation, A_0 is the absorbance at the band-edge (443 nm for the sample in **Figure 5.2**) of a solution of uncharged QDs, and A_S is the absorbance at the band-edge when photocharging saturates. For the sample shown in **Figure 5.2**, $<n>_{max}$ is 0.75; at saturation, the majority of QDs have an excess band-edge electron. The quantum yield (QY) of charging, defined as charging rate divided by photon absorption rate, is <0.1%. The vast majority of photon absorption events do not lead to charging. However, as long as the charging rate is faster than recovery rate, there is an accumulation of charged NCs. Both the value of $<n>_{max}$ and the rate of charging increase with laser power (**Figure 5.7**), suggesting that the saturation point represents an equilibrium point defined by the rates of charging and recovery.[74]

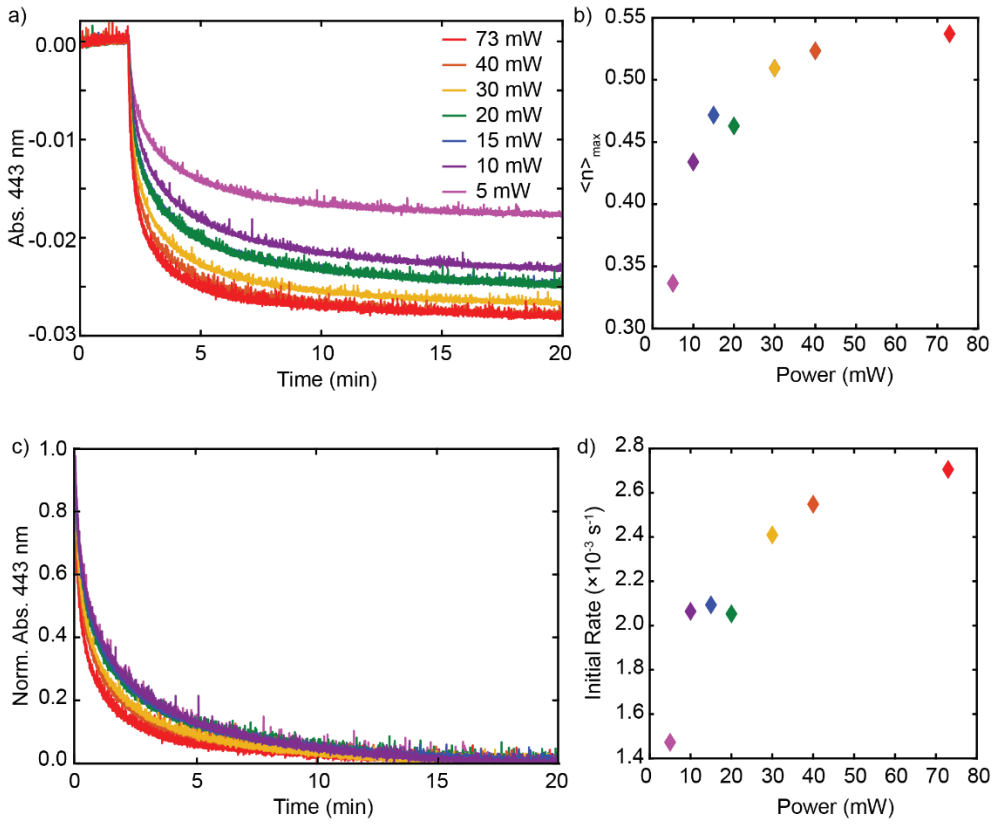

Figure 5.7: a) Power dependence of photocharging kinetics for 5.0 nm CdS QDs (S1-CdS-OA). The starting kinetics have been shifted to start at the same relative absorbance to eliminate the minor effects due to sample precipitation. The decrease in absorbance at saturation increases with the laser power. **b)** Maximum fraction of charged QDs as a function of laser power. These data suggest that the charged QDs are in equilibrium with uncharged QDs, which depends on the rates of charging and recovery, which, in turn, depend on excitation rate. **c)** Normalized power dependence of photocharging kinetics shown in a. **d)** The initial rate of photocharging as a function of laser power. Rates were calculated by fitting the first minute of illumination with an exponential..

Photocharging of CdS QDs changes their PL properties in a manner consistent with previous studies of Cd-chalcogenide NCs with excess band-edge electrons.[22,25,67] **Figure 5.8a** compares the PL spectra of 5.0 nm CdS QDs before illumination with the 405 nm laser, after 30 min of illumination, and after letting the sample recover in the dark for approximately two hours. The samples were aged before illumination to slow the recovery kinetics sufficiently to minimize sample changes during the PL experiment, as described in the Methods section. We observe a drastic quenching of the PL after illumination. Normalizing the spectra (**Figure 5.8a**, inset) shows

that after illumination the band-edge emission redshifts from 454 nm to 458 nm. This corresponds to a shift of 24 meV, which is in the range of trion binding energies in similar Cd-chalcogenide NC systems.[75–78] The peak shift reflects the formation of a trion upon excitation of the already-reduced CdS QD by the fluorimeter light source. After recovery, the band-edge PL returns to the original spectral position. Notably, while the absorption spectrum returns to its pre-illumination shape and intensity after the recovery period (**Figure 5.9**), the recovery of the PL intensity is incomplete and the trap-state emission (>500 nm) is enhanced relative to the exciton emission (**Figure 5.8a**).

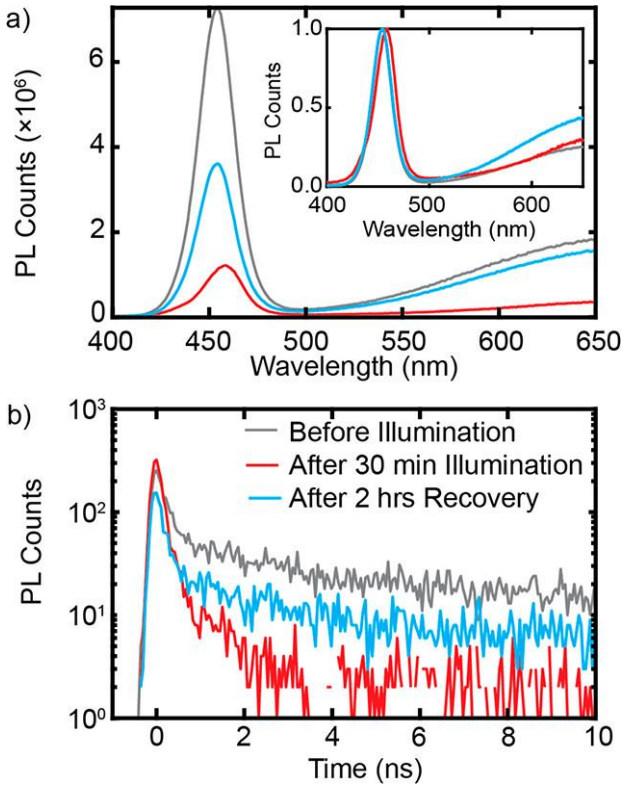

Figure 5.8: a) Steady-state PL spectra and **b)** PL decays at 452 ± 16 nm for 5.0 nm oleate-capped CdS QDs before illumination, immediately after illumination while the band-edge bleach feature of the photocharged state remained, and after full recovery of the absorbance spectrum. The Inset to panel **a** shows the PL spectra normalized at the band-edge peak.

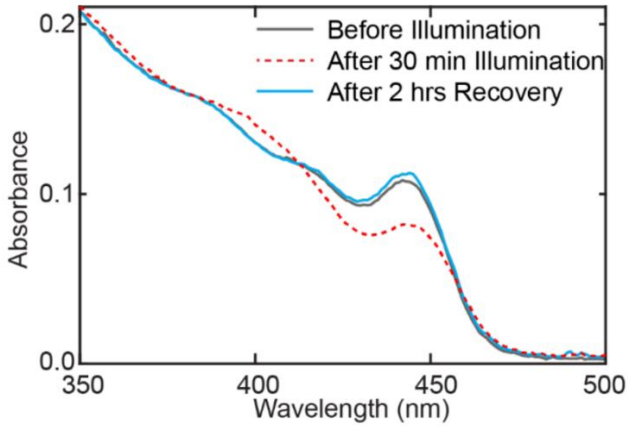

Figure 5.9: Absorption spectrum of the oleate-capped CdS QD sample in **Figure 5.2** (S1-CdS-OA) before illumination, immediately after 30 minutes illumination, and after 2 hours recovery. The absorbance after recovery is almost identical to that before illumination, showing no major spectral changes after a cycle of charging and recovery. The small increase in the first exciton peak intensity for the sample after recovery compared to the sample before illumination is attributed to exposure to room lights before illumination (the recovery was carried out in the dark).

We also examine the kinetics of band-edge PL emission (452 ± 16 nm) decay of CdS QDs before illumination, immediately after 30 minutes of illumination with the 405 nm CW laser, and after the same two-hour recovery period (**Figure 5.8b**). Before illumination, the decay contains a fast (~200 ps) and a slow (~ 8 ns) decay component. Due to the illumination with a 405 nm pulsed laser during data collection, some photocharging may have already occurred during the measurement in the "before illumination" sample. After 30 minutes of illumination with the 405 nm CW laser, there is enhancement of the fast component and near elimination of the slow component in the PL decay (**Figures 5.8b and 5.10**, **Table 5.2**). Such changes to the PL decay are characteristic of charged states, such as trions, which can undergo rapid, non-radiative Auger recombination, and have been previously observed in charged CdSe NCs.[22,25,67] After two hours in the dark, the PL decay recovers to the pre-illumination kinetic form, as can be seen by normalizing the decays (**Figure 5.11**), but with reduced intensity. As in the PL spectra above, the process of charging and recovery leads to reduction in the PL intensity without changing the

absorption spectra (**Figure 5.9**). This incomplete PL recovery suggests changes at the particle surface. Previous reports have documented that loss of PL intensity and relative increase in intensity of trap emission correlate with diminished surface passivation in Cd-chalcogenide NCs.[70,79–82]

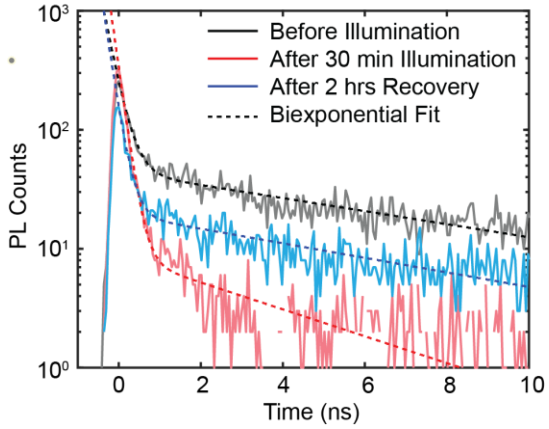

Figure 5.10: PL decays from **Figure 5.8b** overlaid with biexponential fits (PL Counts = $A_1 e^{(-t/\tau 1)} + A_2 e^{(-t/\tau 2)}$ The fit parameters are included in **Table 5.2** below.

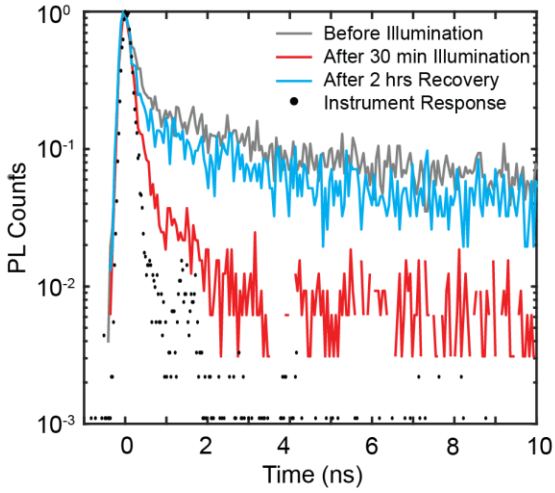

Figure 5.11: The same PL decays as depicted in **Figures 5.8** and **5.10**, normalized to the maximum number of counts. The dotted decay represents the instrument response as measured from scattered laser light.

Table 5.2: Parameters for the biexponential fit to the PL lifetimes. The values for τ1 are instrument response limited.

	A_1	τ_1 (ps)	A_2	τ_2 (ns)
Before Illumination	212±8	242±17	44±3	7.9±0.9
Immediately After Illumination	324±5	174±5	9±2	3.9±1.1
After 2 hrs Recovery	138±6	188±14	19±2	7.1±1.1

5.4.2 Photocharging with different surface-capping ligands, solvents, and NCs

The data presented thus far show that 5.0 nm CdS QDs passivated with oleate ligands in toluene undergo reversible photocharging, specifically photoreduction with 405 nm illumination, and this process leads to NC surface changes as detected by PL. To advance towards a mechanism for this photocharging process, we explore the conditions under which it occurs. We observe photoreduction in CdS NCs with two non-polar ligands, each in two solvents: 5.0 nm CdS QD samples with oleate surface capping-ligands (**Figure 5.12a-c**) and 3.9 by 14 nm CdS nanorods with ODPA ligands (**Figure 5.12d-f**), both in toluene and hexanes. We also observe photocharging in tetrahydrofuran and chloroform for both NCs, but particle degradation in these solvents rendered quantitative analysis unreliable. In both toluene and hexane solvents, ODPA-capped nanorods show lower $\langle n \rangle_{max}$ values (0.24 and 0.06, respectively) than oleate-capped QDs (0.62 and 0.35, respectively) (**Figure 5.12c, 5.12f**), despite a 3.1 times higher per-particle excitation rate in the ODPA-capped nanorods. Earlier experiments demonstrated that higher excitation rates result in a more significant degree of photocharging (**Figure 5.7**), and therefore the degree of charging disparity due to ligand (oleate vs. ODPA) is likely even more significant than what we observe in

Figure 5.12. Meanwhile, both CdS NC samples have a larger $\langle n \rangle_{max}$ in toluene than in hexanes (**Figure 5.12c, 5.12f**). The changes in PL spectra and intensity upon charging and recovery discussed above already suggest that the NC surface plays an important role in the charging mechanism. The dependence of $\langle n \rangle_{max}$ on surface-capping ligand as well as solvent suggests that both ligand and ligand solubility are relevant parameters.[83]

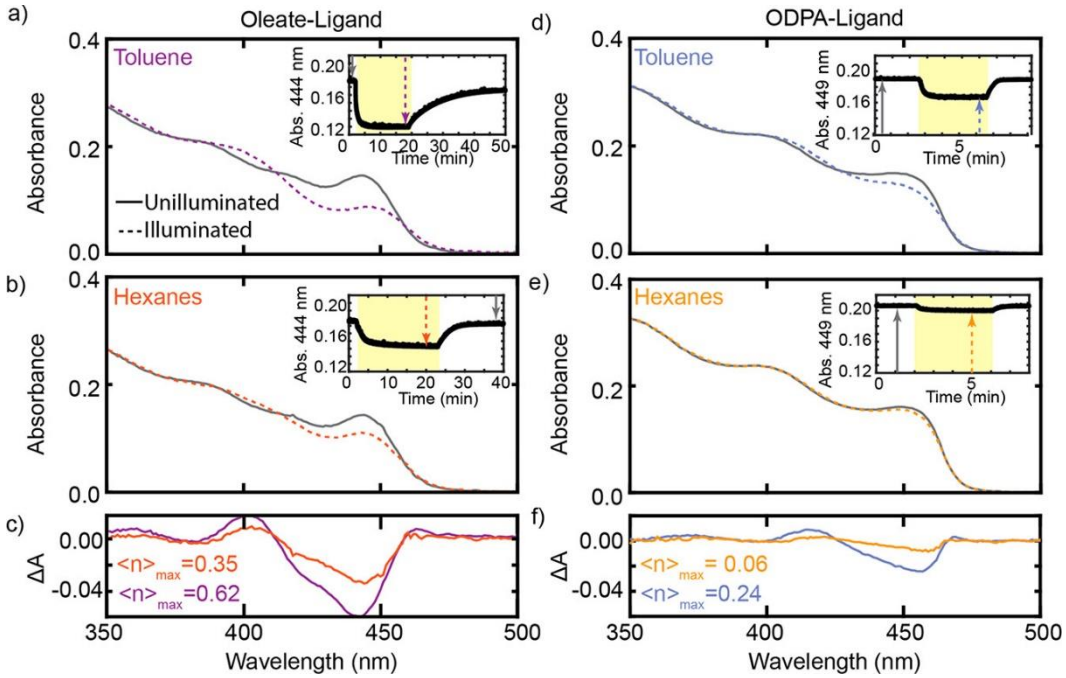

Figure 5.12: Absorbance spectra of CdS NCs in toluene (a,d) and hexanes (b,e), and ΔA spectra (c,f) for: a-c) oleate-capped QDs and d-f) ODPA-capped nanorods. Illuminated and unilluminated samples are depicted, with arrows in the kinetic data insets indicating when each spectrum was taken.photocharging. Notably, the 405 nm excitation source is resonant with the 3.2 nm CdS QD bandgap. Therefore, hot carriers are not necessary for the generation of the photocharged state. This is in contrast to previous reports of photocharging by ligand dissociation in CdSe/CdS core/shell QDs which required Auger-generated hot carriers to facilitate hole removal.[30] Furthermore, based on the CW illumination power and sample absorption cross section, we do not generate a significant fraction of multiexciton states (<0.01), and, therefore, Auger-generated hot holes are unlikely to be responsible for the observed photocharging. It remains to be seen whether hot carriers enhance the rate and extent of photocharging, which would manifest in a wavelength dependence of the value of $\langle n \rangle_{max}$.

In addition to changing PL properties, the CdS QD samples exhibit changes in the kinetics of charging and recovery that have no corresponding changes in the shape of the QD absorption spectrum, even after multiple days and illumination cycles. The CdS QD samples that we have

studied commonly show a permanent increase in the rate of charging kinetics after the first illumination cycle (**Figure 5.14a**), as well as a continuous deceleration of recovery kinetics over multiple repeated photocharging cycles even after charging kinetics have stopped varying (**Figure 5.14b**). Additionally, sample age affects charging: days after initial preparation, QD samples often show slower photocharging kinetics than freshly diluted particles (**Figure 5.15**). We emphasize that neither kinetic hysteresis nor sample age have a correlated change in the shape of the absorption spectrum, pointing to a root cause of photocharging in which the NC surface plays a major role regardless of ligand or solvent type.

In contrast to the significant degree of photocharging observed for CdS NCs of different sizes, morphologies, and surface-capping ligands, CdSe QDs do not show changes in absorption spectra upon illumination. Neither 3.0 nm (**Figure 5.13b**) nor 2.3 nm diameter (**Figure 5.13c**) oleate-capped, nor 3.4 nm ODPA-capped CdSe QDs (**Figure 5.16**) show any evidence of the characteristic ΔA under 405 nm CW illumination. We therefore conclude that the photoreduction we observe is specific to CdS, and hot carriers (of 810 meV and 530 meV excess energy in 3.0 and 2.3 nm CdSe QDs, respectively) are not sufficient to mediate the photocharging in CdSe QDs with either oleate or ODPA surface passivation.

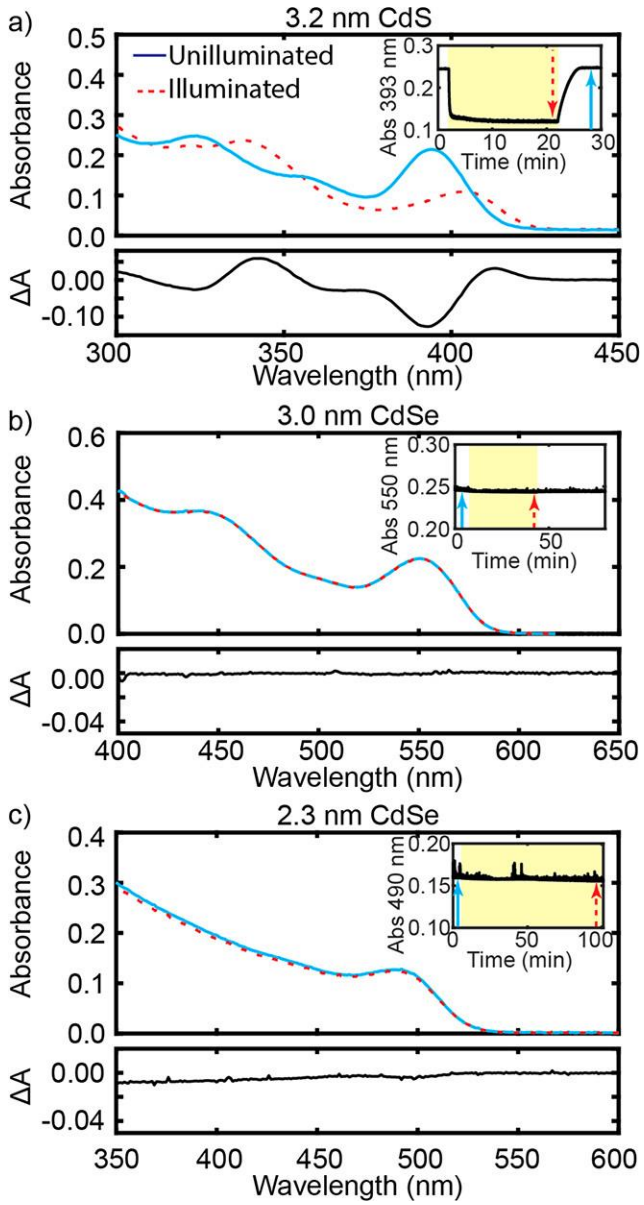

Figure 5.13: Absorption spectra of an unilluminated and illuminated sample (above) and the ΔA spectrum (below) for a sample of oleate-capped **a)** 3.2 nm CdS QDs, **b)** 3.0 nm CdSe QDs, and **c)** 2.3 nm CdSe QDs. Insets show kinetics of the band-edge absorption through illumination cycles (yellow). The approximate times when absorption spectra were recorded are marked with corresponding color-coded arrows in each inset.

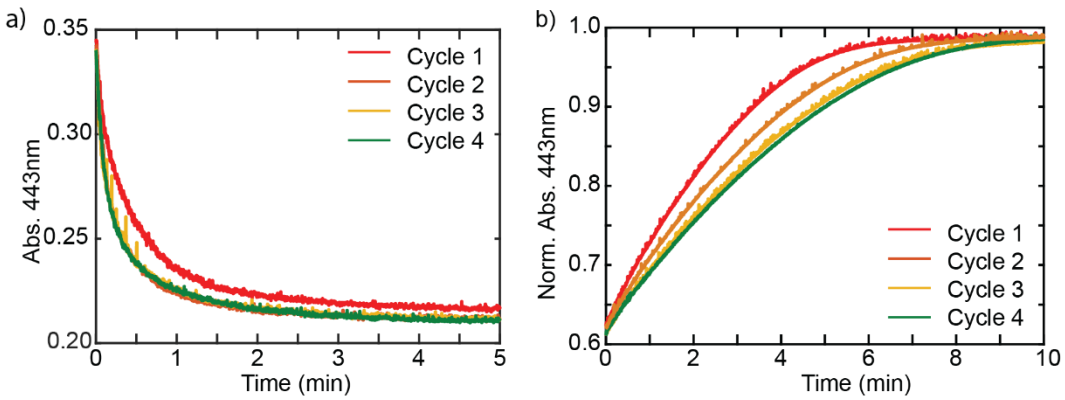

Figure 5.14: a) Kinetics of band-edge absorbance from photocharging over multiple successive illumination cycles of 5.0 nm oleate-capped CdS QDs (S1-CdS-OA). **b)** Normalized kinetics of recovery of band-edge absorbance from photocharging for the same successive illumination cycles as **14a**. The data presented in this figure is the same kinetic data as **Figure 2c,** with each illumination cycle shifted in time to allow more direct comparison.

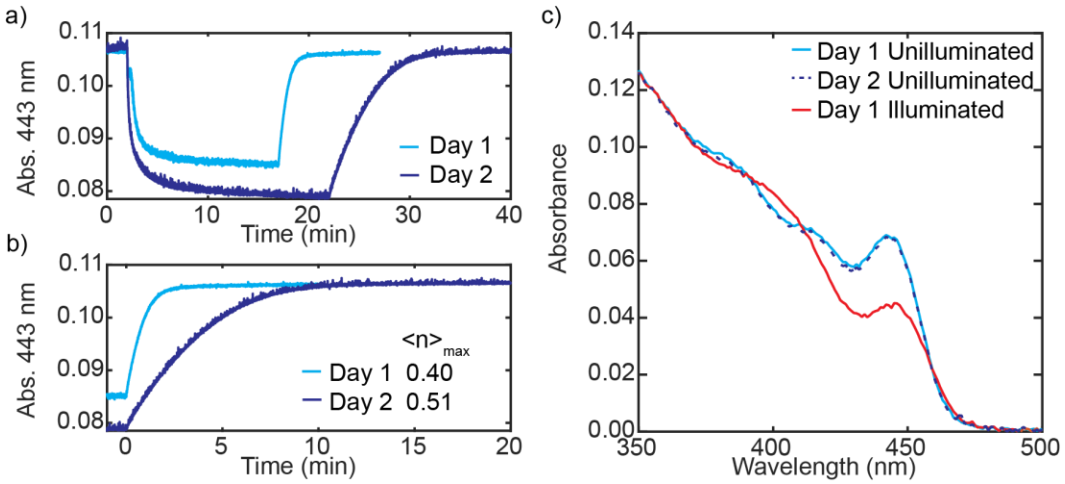

Figure 5.15: a) Photocharging kinetics of 5.0 nm oleate-capped CdS (S1-CdS-OA) on the day of sample preparation (day 1), and the subsequent day (day 2). **b)** The same charging kinetics as in a, x-shifted to show the drastic change in recovery kinetics. **c)** Absorption spectra of the unilluminated sample on day 1 and day 2, and the illuminated sample on day 1.

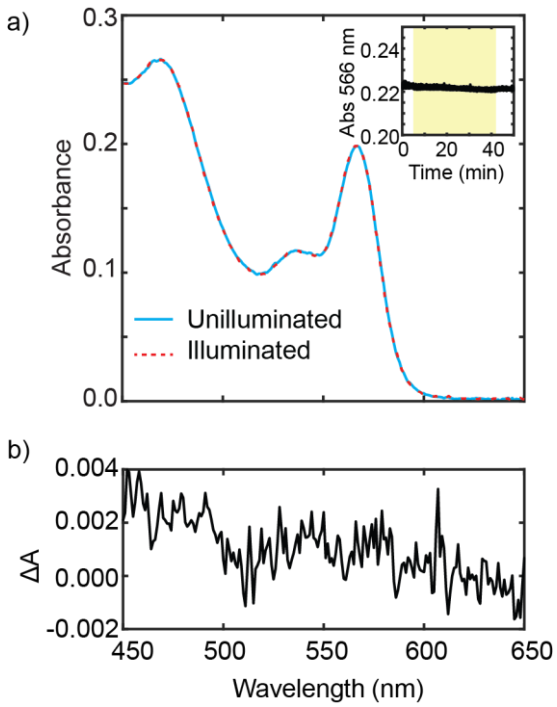

Figure 5.16: a) Absorbance spectrum of a 3.4 nm CdSe QD capped with ODPA ligands (S7-CdSe-ODPA) during illumination after kinetic changes had saturated and after recovery. The absorbance at the band-edge peak (566 nm) over one illumination and recovery cycle is inset. **b)** The change in absorbance between the unilluminated and illuminated spectra shown in **a**.

5.4.3 Proposed mechanism of photocharging in CdS NCs

In order to generate a long-lived negatively charged CdS NC from a photoexcited state, a hole must be removed from the NC. The incomplete recovery of the original PL spectra and intensity after the recovery of the absorption spectrum (**Figure 5.8**) and the varying kinetics of charging and recovery over multiple cycles (**Figure 5.14**) suggest that the hole removal changes the particle surface. The dependence of $\langle n \rangle_{max}$ on the ligand, nanocrystal morphology, and solvent (**Figure 5.12**) suggests that these parameters impact the probability of hole removal. A mechanism of hole removal by oleate ligand oxidation has been proposed previously for CdSe/CdS core-shell NCs[30] and dissociation of methyl ligands has led to a photoreduction of CdSe QDs.[50] We hypothesize that such a ligand-dissociation mechanism is responsible for the photocharging observed here (**Scheme 5.1**). The mechanism involves photoexcited hole transfer to the surface-

capping ligand and subsequent ligand dissociation. Each reduction event requires transfer of one hole, and therefore oxidation of one ligand molecule.

Scheme 5.1: Proposed mechanism of ligand-mediated photocharging in which a photoexcited hole is transferred from the QD to a surface-capping ligand, which dissociates from the QD.

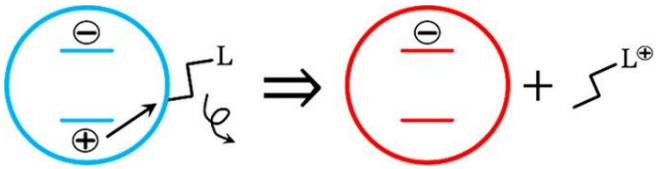

The evidence supporting the mechanism in **Scheme 5.1** is as follows: (a) Previous work has shown that oleic acid can readily accept holes of roughly the same electrochemical potential as the CdS valence band[84–86] and oleate surface-capping ligands have been oxidized by photoexcited CdSe/CdS QDs.[30] (b) The PL changes reported in **Figure 5.8** are consistent with a process in which ligand dissociation from the surface reveals an underpassivated surface atom, generating an additional surface trap, enhancing trap emission, and reducing the PL quantum yield.[70,79–82] While each reduction leads to oxidation of only one ligand, leaving macroscopic properties like colloidal stability relatively unperturbed, over the course of charging and recovery cycles, the changes in ligation are not entirely reversed, leading to variations in charging and recovery kinetics over time (**Figure 5.14**). (c) The long-lived nature of the charged state is consistent with a dissociative mechanism in which recovery relies on a diffusive process that brings a hole back to the QD. (d) NCs capped with ODPA photocharge to a lesser degree than oleate-capped QDs in both solvents. This may be because ODPA binds more strongly to the NC surface[87] so it is less likely to oxidize and dissociate. (e) Since bulk CdSe has a more negative valence band potential than CdS by ~0.4 V,[85,86] photoexcited holes in CdSe QDs lack the requisite driving force for transfer to oleate or ODPA, resulting in no photocharging (**Figure 5.13**, **Figure**

5.16). This is consistent with the observation that photoexcitation of oleate-capped CdSe QDs functionalized with methyl ligands led to dissociation of the methyl but not oleate ligands.[50]

5.4.4 Photocharging of CdS QDs with MPA ligand

In our exploration of conditions that lead to photocharging in CdS NCs, we found a scenario in which this process does not occur without added reductants. In **Figure 5.17**, we compare the photocharging behavior of 5.0 nm CdS QDs with a polar surface-capping ligand 3-mercaptopropionate (MPA) in two solvents, formamide and ethanol. In the formamide, no evidence of photocharging is observed (**Figure 5.17a**). However, when the same QDs are in a solvent that is a known hole scavenger, such as ethanol (**Figure 5.17b)**,[14,16,19,55] as well as methanol and hole scavenging buffers (**Figure 5.18**), photocharging is observed. The photocharging mechanism here is different than the ligand-dissociation mechanism described above. Instead, the hole scavengers in solution are oxidized to generate the charged state, similar to prior work where chemical hole scavengers were used to accumulate electrons in ZnO[16–18,21,88] and CdSe NCs.[22,23,27] Experiments show that Cd-S bonds with the MPA ligands are stronger than the Cd-O bonds with oleate and ODPA,[87] making the MPA harder to dissociate. This may explain why we do not observe photocharging with MPA ligands without an added hole scavenger. It is also possible that the likelihood of MPA dissociation varies with solvent, contributing to variation in the extent of photocharging. It is worth noting that the spectral signatures of the photocharging of MPA-capped CdS QDs with added hole scavengers are identical to those for photocharging of ODPA- and oleate-capped CdS NCs with no added electron donors.

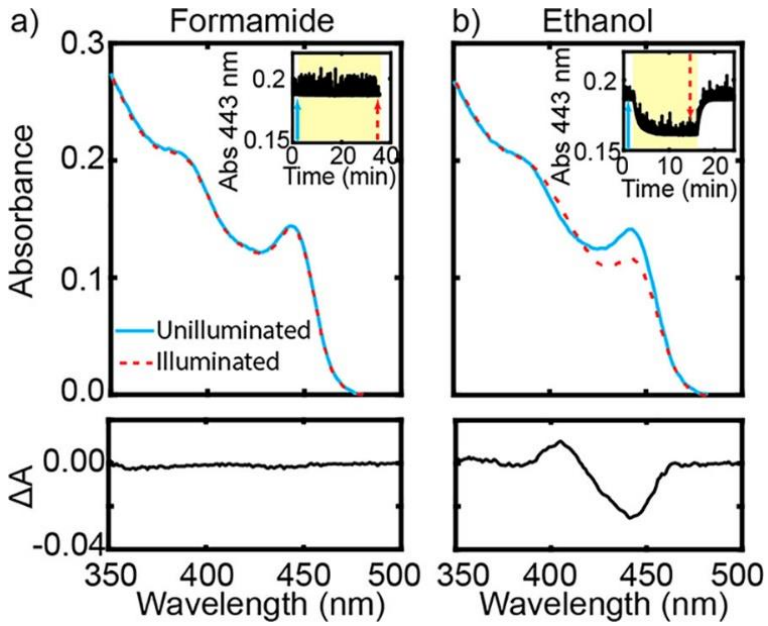

Figure 5.17: Photocharging results for 5.0 nm MPA-capped CdS QDs in **a)** formamide and **b)** ethanol. Absorption spectra of an unilluminated and illuminated sample (above) and the ΔA spectrum (below). Insets show kinetics of the band-edge absorption through illumination cycles (yellow). The approximate times of steady-state absorption spectra are marked with corresponding arrows in each inset.

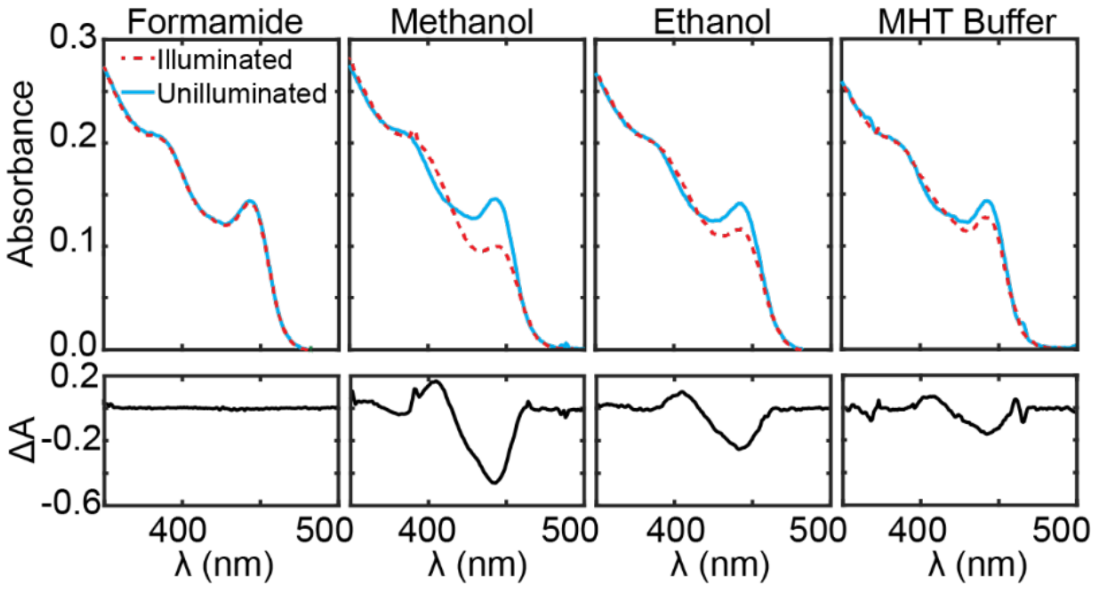

Figure 5.18: Results of photocharging experiments on 5.0 nm CdS QDs capped with MPA ligands (S2-CdS-MPA) in four polar solvents tested (formamide, methanol, ethanol, and 41 mM pH 6.8 MES-HEPES-TAPS buffer). The steady-state absorption spectrum of unilluminated and illuminated QDs is plotted above the difference between the two spectra. The illuminated spectra were taken after light-induced changes had saturated. Each sample is 164 nM and was excited by a 405 nm CW diode laser at 1.9 W/cm^2.

5.4.5 Implications of photocharging in CdS NCs

The results described in this manuscript indicate that care must be taken in studying the optical properties of CdS NCs. Conditions common in various spectroscopy experiments can readily generate photoreduced particles. Although the QY of generation of charged particles is <0.1%, they can accumulate to comprise a significant fraction of the sample, even if the sample is stirred. Furthermore, depending on sample age and concentration, even room lights can be sufficient to generate a moderate fraction of charged QDs (**Figure 5.19**). While exposure to air does quench the process, it also does irreversible damage to the NC surface, potentially altering the photophysical properties of interest.[89,90] Therefore, the possibility of photocharging should be taken into account when studying CdS NC photophysics.

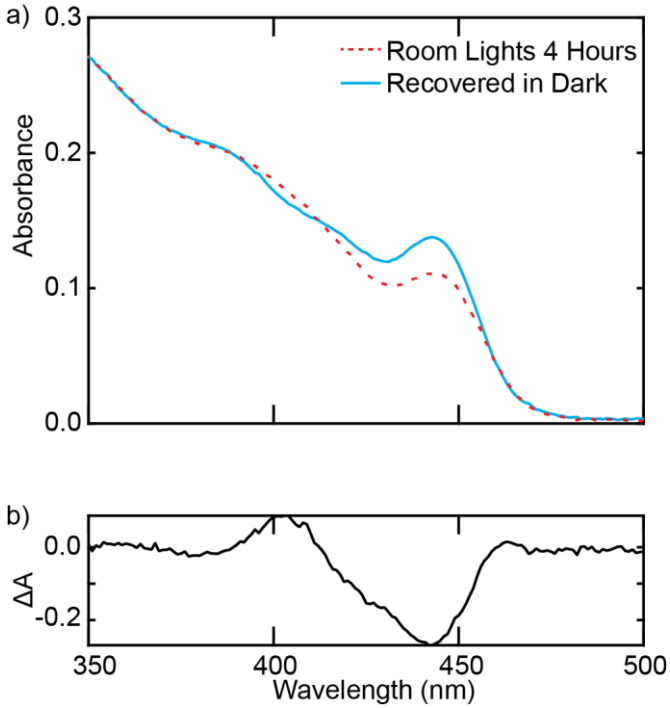

Figure 5.19: a) Charging of 5.0 nm oleate-capped CdS QDs (S1-CdS-OA) using room lights as the sole illumination source. The sample was placed in the dark while stirring until fully recovered then left on the bench under room lights for four hours. There was no laser exposure between the blue and red scans. **b)** The change in absorbance between the red and blue spectra.

These caveats notwithstanding, the long-lived nature, ease of generation, and considerable stability even after repeated excitation cycles of photocharging in CdS NCs provide a potential avenue for high efficiency of electron transfer. CdS NCs have been widely used for solar photochemistry applications, where photoexcited electrons are used as reducing agents.[42–46] Electron transfer (i.e., reduction) processes are limited by competition with electron-hole recombination.[49,91] However, in the charged states the recombination pathway is eliminated by the removal of the hole from the NC. This dramatically increases the electron lifetime, potentially enabling near-unity electron transfer efficiencies. It is possible that some of the remarkable photochemical results achieved with CdS NCs[92–94] could be attributed to previously undetected long-lived charged states. In addition, it is interesting to compare photocharging in CdS NCs with well-known photoreduction of ZnO NCs, which have a valence band that is ~1 eV deeper and therefore far more oxidizing, sufficiently so to oxidize alkylamine ligands.[95] The shallower valence band of CdS NC holes presumably makes photocharging particularly sensitive to variation in ligand and solvent conditions. With further inquiry and sufficient level of understanding, this sensitivity may translate into improved control of photocharging. Overall, the discovery of photocharging in CdS NCs without added electron donors provides some reasons for experimental caution and simultaneously opens up possibilities for future uses of colloidal NC systems for optoelectronic applications.

5.5 Conclusions

We demonstrated light-driven generation of reduced colloidal oleate and ODPA-capped CdS NCs under air-free conditions, which does not require external electron donors and is readily reversible. Post-illumination return to the neutral NC state occurs on the order of several minutes, suggesting that recovery is a diffusion-limited process. Photocharging induces lasting alterations to the NC surface, as seen through the changing PL quantum yield and the rates of photocharging and recovery despite an unchanging NC absorption spectrum. In addition, the dependence of the extent of photocharging on NC surface ligand and solvent implies that ligand properties play an important role in the photoreduction mechanism. In light of these observations, we hypothesize that photocharging of CdS QDs is caused by transfer of the photoexcited hole to the surface-capping ligand, followed by ligand dissociation from the QD. The lack of observed photocharging in CdSe QDs suggests that excited CdSe holes have insufficient driving force for transfer to the ligands. We also observe conditions under which CdS QDs do not exhibit photocharging with no added electron donors; when MPA surface-capping ligands are used, CdS QD photoreduction occurs only in the presence of hole-scavenging solvents. The photoreduction described here generates additional considerations in studies of CdS NC photophysics, and also provides new avenues of exploring optoelectronic properties and applications of these materials.

Bibliography

Chapter 1

(1) Threatt, S. D.; Rees, D. C. Biological Nitrogen Fixation in Theory, Practice, and Reality: A Perspective on the Molybdenum Nitrogenase System. *FEBS Lett.* **2023**, *597* (1), 45–58.

(2) Olah, G. A.; Molnár, Á.; Prakash, G. K. S. *Hydrocarbon Chemistry, 2 Volume Set*; John Wiley & Sons, 2017.

(3) Zhang, W.; Hu, Y.; Ma, L.; Zhu, G.; Wang, Y.; Xue, X.; Chen, R.; Yang, S.; Jin, Z. Progress and Perspective of Electrocatalytic CO2 Reduction for Renewable Carbonaceous Fuels and Chemicals. *Adv. Sci.* **2018**, *5* (1), 1700275.

(4) Ertl, G. Reactions at Surfaces: From Atoms to Complexity (Nobel Lecture). *Angew. Chemie Int. Ed.* **2008**, *47* (19), 3524–3535.

(5) Tvaronavičienė, M.; Baublys, J.; Raudeliūnienė, J.; Jatautaitė, D. Chapter 1 - Global Energy Consumption Peculiarities and Energy Sources: Role of Renewables; Tvaronavičienė, M., Ślusarczyk, B. B. T.-E. T. T. S., Eds.; Elsevier, 2020; pp 1–49.

(6) Höök, M.; Tang, X. Depletion of Fossil Fuels and Anthropogenic Climate Change—A Review. *Energy Policy* **2013**, *52*, 797–809.

(7) (IPCC), I. P. on C. C. *Climate Change 2021 – The Physical Science Basis: Working Group I Contribution to the Sixth Assessment Report of the Intergovernmental Panel on Climate Change*; Cambridge University Press: Cambridge, 2023.

(8) Kampa, M.; Castanas, E. Human Health Effects of Air Pollution. *Environ. Pollut.* **2008**, *151* (2), 362–367.

(9) Sanderson, R. *Chemical Bonds and Bonds Energy*; Elsevier, 2012; Vol. 21.

(10) Marcus, R. A. On the Theory of Oxidation-Reduction Reactions Involving Electron Transfer. III. Applications to Data on the Rates of Organic Redox Reactions. *J. Chem. Phys.* **1957**, *26* (4), 872–877.

(11) Gladysz, J. A. Introduction: Recoverable Catalysts and Reagents - Perspective and Prospective. *Chem. Rev.* **2002**, *102* (10), 3215–3216.

(12) Greeley, J. Theoretical Heterogeneous Catalysis: Scaling Relationships and Computational Catalyst Design. *Annu. Rev. Chem. Biomol. Eng.* **2016**, *7* (Volume 7, 2016), 605–635.

(13) Spencer, M. S.; Twigg, M. V. METAL CATALYST DESIGN AND PREPARATION IN CONTROL OF DEACTIVATION. *Annu. Rev. Mater. Res.* **2005**, *35* (Volume 35, 2005),

427–464.

(14) Morbidelli, M.; Gavriilidis, A.; Varma, A. *Catalyst Design*; Cambridge University Press Cambridge, 2001.

(15) Foley, H. C. Catalyst Preparation–Design and Synthesis. *Catal. today* **1994**, *22* (2), 235–259.

(16) Durand, D. J.; Fey, N. Computational Ligand Descriptors for Catalyst Design. *Chem. Rev.* **2019**, *119* (11), 6561–6594.

(17) Bhatia, S.; Bhatia, S. Introduction to Enzymes and Their Applications. *Introd. to Pharm. Biotechnol.* **2018**, *2*, 1–29.

(18) Copeland, R. A. *Enzymes: A Practical Introduction to Structure, Mechanism, and Data Analysis*; John Wiley & Sons, 2023.

(19) Borovik, A. S. Bioinspired Hydrogen Bond Motifs in Ligand Design: The Role of Noncovalent Interactions in Metal Ion Mediated Activation of Dioxygen. *Acc. Chem. Res.* **2005**, *38* (1), 54–61.

(20) Leveson-Gower, R. B.; Mayer, C.; Roelfes, G. The Importance of Catalytic Promiscuity for Enzyme Design and Evolution. *Nat. Rev. Chem.* **2019**, *3* (12), 687–705.

(21) Zhou, S.; Liu, D.; Fan, K.; Liu, H.; Zhang, X.-D. Atomic-Level Design of Biomimetic Iron–Sulfur Clusters for Biocatalysis. *Nanoscale* **2024**.

(22) Klinman, J. P. Dynamically Achieved Active Site Precision in Enzyme Catalysis. *Acc. Chem. Res.* **2015**, *48* (2), 449–456.

(23) Gerlt, J. A. Relationships between Enzymatic Catalysis and Active Site Structure Revealed by Applications of Site-Directed Mutagenesis. *Chem. Rev.* **1987**, *87* (5), 1079–1105.

(24) Johnson, D. C.; Dean, D. R.; Smith, A. D.; Johnson, M. K. STRUCTURE, FUNCTION, AND FORMATION OF BIOLOGICAL IRON-SULFUR CLUSTERS. *Annu. Rev. Biochem.* **2005**, *74* (Volume 74, 2005), 247–281.

(25) Fontecilla-Camps, J. C.; Amara, P.; Cavazza, C.; Nicolet, Y.; Volbeda, A. Structure–Function Relationships of Anaerobic Gas-Processing Metalloenzymes. *Nature* **2009**, *460* (7257), 814–822.

(26) Vanoni, M. A. Iron-Sulfur Flavoenzymes: The Added Value of Making the Most Ancient Redox Cofactors and the Versatile Flavins Work Together. *Open Biol.* **2021**, *11* (5), 210010.

(27) Blank, L. M.; Ebert, B. E.; Buehler, K.; Bühler, B. Redox Biocatalysis and Metabolism: Molecular Mechanisms and Metabolic Network Analysis. *Antioxid. Redox Signal.* **2010**, *13*

(3), 349–394.

(28) Desage-El Murr, M. Nature Is the Cure: Engineering Natural Redox Cofactors for Biomimetic and Bioinspired Catalysis. *ChemCatChem* **2020**, *12* (1), 53–62.

(29) Stripp, S. T.; Duffus, B. R.; Fourmond, V.; Léger, C.; Leimkühler, S.; Hirota, S.; Hu, Y.; Jasniewski, A.; Ogata, H.; Ribbe, M. W. Second and Outer Coordination Sphere Effects in Nitrogenase, Hydrogenase, Formate Dehydrogenase, and CO Dehydrogenase. *Chem. Rev.* **2022**, *122* (14), 11900–11973.

(30) Lewis, K. Symposium on Bioelectrochemistry of Microorganisms. IV. Biochemical Fuel Cells. *Bacteriol. Rev.* **1966**, *30* (1), 101.

(31) Lee, S. H.; Choi, D. S.; Kuk, S. K.; Park, C. B. Photobiocatalysis: Activating Redox Enzymes by Direct or Indirect Transfer of Photoinduced Electrons. *Angew. Chemie Int. Ed.* **2018**, *57* (27), 7958–7985.

(32) Cadoux, C.; Milton, R. D. Recent Enzymatic Electrochemistry for Reductive Reactions. *ChemElectroChem* **2020**, *7* (9), 1974–1986.

(33) Maciá-Agulló, J. A.; Corma, A.; Garcia, H. Photobiocatalysis: The Power of Combining Photocatalysis and Enzymes. *Chem. – A Eur. J.* **2015**, *21* (31), 10940–10959.

(34) Utterback, J. K.; Ruzicka, J. L.; Keller, H. R.; Pellows, L. M.; Dukovic, G. Electron Transfer from Semiconductor Nanocrystals to Redox Enzymes. *Annu. Rev. Phys. Chem.* **2020**, *71* (1), 335–359.

(35) Brus, L. Electronic Wave Functions in Semiconductor Clusters: Experiment and Theory. *J. Phys. Chem.* **1986**, *90* (12), 2555–2560.

(36) Bawendi, M. G.; Steigerwald, M. L.; Brus, L. E. The Quantum Mechanics of Larger Semiconductor Clusters ("Quantum Dots"). *Annu. Rev. Phys. Chem.* **1990**, *41* (1), 477–496.

(37) Burda, C.; Chen, X.; Narayanan, R.; El-Sayed, M. A. Chemistry and Properties of Nanocrystals of Different Shapes. *Chem. Rev.* **2005**, *105* (4), 1025–1102.

(38) Donegá, C. de M. Synthesis and Properties of Colloidal Heteronanocrystals. *Chem. Soc. Rev.* **2011**, *40* (3), 1512–1546.

(39) Nogueira, A. E.; Ribeiro, L. S.; Nogueira, F. G. E.; Torres, J. A. Semiconductors: An Introduction. In *Handbook of Semiconductors*; CRC Press, 2025; pp 1–11.

(40) Dimmock, J. O. Chapter 7 Introduction to the Theory of Exciton States in Semiconductors. In *Semiconductors and Semimetals*; Willardson, R. K., Beer, A. C. B. T.-S. and S., Eds.; Elsevier, 1967; Vol. 3, pp 259–319.

(41) Chiang, W.; Morshed, O.; D. Krauss, T. *Quantum Confined Semiconductor Nanocrystals*; American Chemical Society, 2023.

(42) A. Hines, D.; V. Kamat, P. Recent Advances in Quantum Dot Surface Chemistry. *ACS Appl. Mater. & Interfaces* **2014**, *6* (5), 3041–3057.

(43) Boles, M. A.; Ling, D.; Hyeon, T.; Talapin, D. V. The Surface Science of Nanocrystals. *Nature Materials*. Nature Publishing Group January 22, 2016, pp 141–153.

(44) Krause, M. M.; Kambhampati, P. Linking Surface Chemistry to Optical Properties of Semiconductor Nanocrystals. *Phys. Chem. Chem. Phys.* **2015**, *17* (29), 18882–18894.

(45) Zito, J.; Infante, I. The Future of Ligand Engineering in Colloidal Semiconductor Nanocrystals. *Acc. Chem. Res.* **2021**, *54* (7), 1555–1564.

(46) De Roo, J. The Surface Chemistry of Colloidal Nanocrystals Capped by Organic Ligands. *Chem. Mater.* **2023**, *35* (10), 3781–3792.

(47) Shulenberger, K.; Keller, H.; Pellows, L.; Brown, N.; Dukovic, G. Photocharging of Colloidal CdS Nanocrystals. *J. Phys. Chem. C 125* (41), 22650–22659.

(48) Kambhampati, P. On the Kinetics and Thermodynamics of Excitons at the Surface of Semiconductor Nanocrystals: Are There Surface Excitons? *Chem. Phys.* **2015**, *446*, 92–107.

(49) Utterback, J. K.; Cline, R. P.; Shulenberger, K. E.; Eaves, J. D.; Dukovic, G. The Motion of Trapped Holes on Nanocrystal Surfaces. *Journal of Physical Chemistry Letters*. American Chemical Society November 19, 2020, pp 9876–9885.

(50) Lubitz, W.; Ogata, H.; Rüdiger, O.; Reijerse, E. Hydrogenases. *Chemical Reviews*. American Chemical Society April 23, 2014, pp 4081–4148.

(51) Vignais, P. M.; Billoud, B. Occurrence, Classification, and Biological Function of Hydrogenases: An Overview. *Chem. Rev.* **2007**, *107* (10), 4206–4272.

(52) Peters, J. W.; Schut, G. J.; Boyd, E. S.; Mulder, D. W.; Shepard, E. M.; Broderick, J. B.; King, P. W.; Adams, M. W. W. [FeFe]- and [NiFe]-Hydrogenase Diversity, Mechanism, and Maturation. *Biochim. Biophys. Acta - Mol. Cell Res.* **2015**, *1853* (6), 1350–1369.

(53) Chen, A. Y.; Adamek, R. N.; Dick, B. L.; Credille, C. V; Morrison, C. N.; Cohen, S. M. Targeting Metalloenzymes for Therapeutic Intervention. *Chem. Rev.* **2019**, *119* (2), 1323–1455.

(54) Gauquelin, C.; Baffert, C.; Richaud, P.; Kamionka, E.; Etienne, E.; Guieysse, D.; Girbal, L.; Fourmond, V.; André, I.; Guigliarelli, B.; Léger, C.; Soucaille, P.; Meynial-Salles, I. Roles of the F-Domain in [FeFe] Hydrogenase. *Biochim. Biophys. Acta - Bioenerg.* **2018**, *1859* (2), 69–77.

(55) Lubner, C. E.; Artz, J. H.; Mulder, D. W.; Oza, A.; Ward, R. J.; Williams, S. G.; Jones, A. K.; Peters, J. W.; Smalyukh, I. I.; Bharadwaj, V. S.; King, P. W. A Site-Differentiated [4Fe–4S] Cluster Controls Electron Transfer Reactivity of Clostridium Acetobutylicum [FeFe]-Hydrogenase I. *Chem. Sci.* **2022**, *13* (16), 4581–4588.

(56) Rumpel, S.; Siebel, J. F.; Diallo, M.; Farès, C.; Reijerse, E. J.; Lubitz, W. Structural Insight into the Complex of Ferredoxin and [FeFe] Hydrogenase from Chlamydomonas Reinhardtii. *ChemBioChem* **2015**, *16* (11), 1663–1669.

(57) Artz, J. H.; Zadvornyy, O. A.; Mulder, D. W.; Keable, S. M.; Cohen, A. E.; Ratzloff, M. W.; Williams, S. G.; Ginovska, B.; Kumar, N.; Song, J.; McPhillips, S. E.; Davidson, C. M.; Lyubimov, A. Y.; Pence, N.; Schut, G. J.; Jones, A. K.; Soltis, S. M.; Adams, M. W. W.; Raugei, S.; King, P. W.; Peters, J. W. Tuning Catalytic Bias of Hydrogen Gas Producing Hydrogenases. *J. Am. Chem. Soc.* **2020**, *142* (3), 1227–1235.

(58) Caserta, G.; Papini, C.; Adamska-Venkatesh, A.; Pecqueur, L.; Sommer, C.; Reijerse, E.; Lubitz, W.; Gauquelin, C.; Meynial-Salles, I.; Pramanik, D.; Artero, V.; Atta, M.; del Barrio, M.; Faivre, B.; Fourmond, V.; Léger, C.; Fontecave, M. Engineering an [FeFe]-Hydrogenase: Do Accessory Clusters Influence O2 Resistance and Catalytic Bias? *J. Am. Chem. Soc.* **2018**, *140* (16), 5516–5526.

(59) Birrell, J. A.; Rodríguez-Maciá, P.; Reijerse, E. J.; Martini, M. A.; Lubitz, W. The Catalytic Cycle of [FeFe] Hydrogenase: A Tale of Two Sites. *Coord. Chem. Rev.* **2021**, *449*, 214191.

(60) Fasano, A.; Jacq-Bailly, A.; Wozniak, J.; Fourmond, V.; Léger, C. Catalytic Bias and Redox-Driven Inactivation of the Group B FeFe Hydrogenase CpIII. *ACS Catal.* **2024**, *14* (9), 7001–7010.

(61) Fasano, A.; Fourmond, V.; Léger, C. Outer-Sphere Effects on the O2 Sensitivity, Catalytic Bias and Catalytic Reversibility of Hydrogenases. *Chem. Sci.* **2024**, *15* (15), 5418–5433.

(62) Kisgeropoulos, E. C.; Bharadwaj, V. S.; Mulder, D. W.; King, P. W. The Contribution of Proton-Donor PKa on Reactivity Profiles of [FeFe]-Hydrogenases. *Front. Microbiol.* **2022**, *13*.

(63) Brown, K. A.; Dayal, S.; Ai, X.; Rumbles, G.; King, P. W. Controlled Assembly of Hydrogenase-CdTe Nanocrystal Hybrids for Solar Hydrogen Production. *J. Am. Chem. Soc.* **2010**, *132* (28), 9672–9680.

(64) Brown, K. A.; Song, Q.; Mulder, D. W.; King, P. W. Diameter Dependent Electron Transfer Kinetics in Semiconductor-Enzyme Complexes. *ACS Nano* **2014**, *8* (10), 10790–10798.

(65) Brown, K. A.; Wilker, M. B.; Boehm, M.; Dukovic, G.; King, P. W. Characterization of Photochemical Processes for H2 Production by CdS Nanorod–[FeFe] Hydrogenase Complexes. *J. Am. Chem. Soc.* **2012**, *134* (12), 5627–5636.

(66) Wilker, M. B.; Shinopoulos, K. E.; Brown, K. A.; Mulder, D. W.; King, P. W.; Dukovic, G. Electron Transfer Kinetics in CdS Nanorod–[FeFe]-Hydrogenase Complexes and Implications for Photochemical H2 Generation. *J. Am. Chem. Soc.* **2014**, *136* (11), 4316–4324.

(67) Wilker, M. B.; Utterback, J. K.; Greene, S.; Brown, K. A.; Mulder, D. W.; King, P. W.; Dukovic, G. Role of Surface-Capping Ligands in Photoexcited Electron Transfer between CdS Nanorods and [FeFe] Hydrogenase and the Subsequent H2 Generation. *J. Phys. Chem. C* **2018**, *122* (1), 741–750.

(68) Utterback, J. K.; Wilker, M. B.; Brown, K. A.; King, P. W.; Eaves, J. D.; Dukovic, G. Competition between Electron Transfer, Trapping, and Recombination in CdS Nanorod–Hydrogenase Complexes. *Phys. Chem. Chem. Phys.* **2015**, *17* (8), 5538–5542.

(69) Utterback, J. K.; Wilker, M. B.; Mulder, D. W.; King, P. W.; Eaves, J. D.; Dukovic, G. Quantum Efficiency of Charge Transfer Competing against Nonexponential Processes: The Case of Electron Transfer from CdS Nanorods to Hydrogenase. *J. Phys. Chem. C* **2019**, *123* (1), 886–896.

(70) Ratzloff, M. W.; Wilker, M. B.; Mulder, D. W.; Lubner, C. E.; Hamby, H.; Brown, K. A.; Dukovic, G.; King, P. W. Activation Thermodynamics and H/D Kinetic Isotope Effect of the Hox to HredH+ Transition in [FeFe] Hydrogenase. *J. Am. Chem. Soc.* **2017**, *139* (37), 12879–12882.

(71) Brown, K. A.; King, P. W. Coupling Biology to Synthetic Nanomaterials for Semi-Artificial Photosynthesis. *Photosynth. Res.* **2020**, *143* (2), 193–203.

(72) King, P. W. Designing Interfaces of Hydrogenase–Nanomaterial Hybrids for Efficient Solar Conversion. *Biochim. Biophys. Acta - Bioenerg.* **2013**, *1827* (8), 949–957.

(73) Pandey, A. S.; Harris, T. V; Giles, L. J.; Peters, J. W.; Szilagyi, R. K. Dithiomethylether as a Ligand in the Hydrogenase H-Cluster. *J. Am. Chem. Soc.* **2008**, *130* (13), 4533–4540.

Chapter 2

(1) Utterback, J. K.; Ruzicka, J. L.; Keller, H. R.; Pellows, L. M.; Dukovic, G. Electron Transfer from Semiconductor Nanocrystals to Redox Enzymes. *Annu. Rev. Phys. Chem.* **2020**, *71* (1), 335–359.

(2) Brown, K. A.; King, P. W. Coupling Biology to Synthetic Nanomaterials for Semi-Artificial Photosynthesis. *Photosynth. Res.* **2020**, *143* (2), 193–203.

(3) Chiang, W.; Morshed, O.; D. Krauss, T. *Quantum Confined Semiconductor Nanocrystals*; American Chemical Society, 2023.

(4) Alivisatos, A. P. Semiconductor Clusters, Nanocrystals, and Quantum Dots. *Science* **1996**, *271* (5251), 933–937.

(5) Brown, K. A.; Wilker, M. B.; Boehm, M.; Dukovic, G.; King, P. W. Characterization of Photochemical Processes for H2 Production by CdS Nanorod–[FeFe] Hydrogenase Complexes. *J. Am. Chem. Soc.* **2012**, *134* (12), 5627–5636.

(6) Wilker, M. B.; Shinopoulos, K. E.; Brown, K. A.; Mulder, D. W.; King, P. W.; Dukovic, G. Electron Transfer Kinetics in CdS Nanorod–[FeFe]-Hydrogenase Complexes and Implications for Photochemical H2 Generation. *J. Am. Chem. Soc.* **2014**, *136* (11), 4316–4324.

(7) Artz, J. H.; Mulder, D. W.; Ratzloff, M. W.; Lubner, C. E.; Zadvornyy, O. A.; LeVan, A. X.; Williams, S. G.; Adams, M. W. W.; Jones, A. K.; King, P. W.; Peters, J. W. Reduction Potentials of [FeFe]-Hydrogenase Accessory Iron–Sulfur Clusters Provide Insights into the Energetics of Proton Reduction Catalysis. *J. Am. Chem. Soc.* **2017**, *139* (28), 9544–9550.

(8) Ratzloff, M. W.; Wilker, M. B.; Mulder, D. W.; Lubner, C. E.; Hamby, H.; Brown, K. A.; Dukovic, G.; King, P. W. Activation Thermodynamics and H/D Kinetic Isotope Effect of the Hox to HredH+ Transition in [FeFe] Hydrogenase. *J. Am. Chem. Soc.* **2017**, *139* (37), 12879–12882.

(9) W., K. P.; C., P. M.; L., G. M.; Michael, S. Functional Studies of [FeFe] Hydrogenase Maturation in an Escherichia Coli Biosynthetic System. *J. Bacteriol.* **2006**, *188* (6), 2163–2172.

(10) Shulenberger, K.; Keller, H.; Pellows, L.; Brown, N.; Dukovic, G. Photocharging of Colloidal CdS Nanocrystals. *J. Phys. Chem. C 125* (41), 22650–22659.

(11) Yu, W. W.; Peng, X. Formation of High-Quality CdS and Other II - VI Semiconductor Nanocrystals in Noncoordinating Solvents: Tunable Reactivity of Monomers. *Communications* **2002**, *114* (13), 2368–2371.

(12) Peterson, M. D.; Jensen, S. C.; Weinberg, D. J.; Weiss, E. A. Mechanisms for Adsorption of Methyl Viologen on Cds Quantum Dots. *ACS Nano* **2014**, *8* (3), 2826–2837.

(13) William Yu, W.; Qu, L.; Guo, W.; Peng, X. Experimental Determination of the Extinction Coefficient of CdTe, CdSe, and CdS Nanocrystals. *Chem. Mater*. **2003**, *15* (14), 2854–2860.

(14) Amirav, L.; Alivisatos, A. P. Photocatalytic Hydrogen Production with Tunable Nanorod Heterostructures. *J. Phys. Chem. Lett.* **2010**, *1* (7), 1051–1054.

(15) Pearce, O. M.; Duncan, J. S.; Damrauer, N. H.; Dukovic, G. Ultrafast Hole Transfer from CdS Quantum Dots to a Water Oxidation Catalyst. *J. Phys. Chem. C* **2018**, *122* (30), 17559–17565.

(16) Tseng, H.-W.; B. Wilker, M.; H. Damrauer, N.; Dukovic, G. Charge Transfer Dynamics between Photoexcited CdS Nanorods and Mononuclear Ru Water-Oxidation Catalysts. *J. Am. Chem. Soc.* **2013**, *135* (9), 3383–3386.

(17) Klimov, V. I. Spectral and Dynamical Properties of Multiexcitons in Semiconductor Nanocrystals. *Annu. Rev. Phys. Chem.* **2007**, *58* (1), 635–673.

(18) Zhu, H.; Yang, Y.; Wu, K.; Lian, T. Charge Transfer Dynamics from Photoexcited Semiconductor Quantum Dots. *Annu. Rev. Phys. Chem.* **2016**, *67* (1), 259–281.

(19) Kambhampati, P. Unraveling the Structure and Dynamics of Excitons in Semiconductor Quantum Dots. *Acc. Chem. Res.* **2011**, *44* (1), 1–13.

(20) Veamatahau, A.; Jiang, B.; Seifert, T.; Makuta, S.; Latham, K.; Kanehara, M.; Teranishi, T.; Tachibana, Y. Origin of Surface Trap States in CdS Quantum Dots: Relationship between Size Dependent Photoluminescence and Sulfur Vacancy Trap States. *Phys. Chem. Chem. Phys.* **2015**, *17* (4), 2850–2858.

(21) Boles, M. A.; Ling, D.; Hyeon, T.; Talapin, D. V. The Surface Science of Nanocrystals. *Nature Materials*. Nature Publishing Group January 22, 2016, pp 141–153.

(22) Shulenberger, K. E.; Jilek, M. R.; Sherman, S. J.; Hohman, B. T.; Dukovic, G. Electronic Structure and Excited State Dynamics of Cadmium Chalcogenide Nanorods. *Chem. Rev.* **2023**, *123* (7), 3852–3903.

(23) Vempati, S.; Ertas, Y.; Uyar, T. Sensitive Surface States and Their Passivation Mechanism in CdS Quantum Dots. *J. Phys. Chem. C* **2013**, *117* (41), 21609–21618.

(24) Utterback, J. K.; Wilker, M. B.; Brown, K. A.; King, P. W.; Eaves, J. D.; Dukovic, G. Competition between Electron Transfer, Trapping, and Recombination in CdS Nanorod–Hydrogenase Complexes. *Phys. Chem. Chem. Phys.* **2015**, *17* (8), 5538–5542.

(25) Wilker, M. B.; Utterback, J. K.; Greene, S.; Brown, K. A.; Mulder, D. W.; King, P. W.; Dukovic, G. Role of Surface-Capping Ligands in Photoexcited Electron Transfer between CdS Nanorods and [FeFe] Hydrogenase and the Subsequent H2 Generation. *J. Phys. Chem. C* **2018**, *122* (1), 741–750.

(26) Utterback, J. K.; Wilker, M. B.; Mulder, D. W.; King, P. W.; Eaves, J. D.; Dukovic, G.

Quantum Efficiency of Charge Transfer Competing against Nonexponential Processes: The Case of Electron Transfer from CdS Nanorods to Hydrogenase. *J. Phys. Chem. C* **2019**, *123* (1), 886–896.

Chapter 3

(1) Lubitz, W.; Ogata, H.; Rüdiger, O.; Reijerse, E. Hydrogenases. *Chemical Reviews*. American Chemical Society April 23, 2014, pp 4081–4148.

(2) Peters, J. W.; Schut, G. J.; Boyd, E. S.; Mulder, D. W.; Shepard, E. M.; Broderick, J. B.; King, P. W.; Adams, M. W. W. [FeFe]- and [NiFe]-Hydrogenase Diversity, Mechanism, and Maturation. *Biochim. Biophys. Acta - Mol. Cell Res.* **2015**, *1853* (6), 1350–1369.

(3) Hosseinzadeh, P.; Lu, Y. Design and Fine-Tuning Redox Potentials of Metalloproteins Involved in Electron Transfer in Bioenergetics. *Biochim. Biophys. Acta - Bioenerg.* **2016**, *1857* (5), 557–581.

(4) Jeuken, L. J. C.; Jones, A. K.; Chapman, S. K.; Cecchini, G.; Armstrong, F. A. Electron-Transfer Mechanisms through Biological Redox Chains in Multicenter Enzymes. *J. Am. Chem. Soc.* **2002**, *124* (20), 5702–5713.

(5) Paquete, C. M.; Louro, R. O. Unveiling the Details of Electron Transfer in Multicenter Redox Proteins. *Acc. Chem. Res.* **2014**, *47* (1), 56–65.

(6) Moser, C. C.; Page, C. C.; Farid, R.; Dutton, P. L. Biological Electron Transfer. *J. Bioenerg. Biomembr.* **1995**, *27* (3), 263–274.

(7) Artz, J. H.; Zadvornyy, O. A.; Mulder, D. W.; Keable, S. M.; Cohen, A. E.; Ratzloff, M. W.; Williams, S. G.; Ginovska, B.; Kumar, N.; Song, J.; McPhillips, S. E.; Davidson, C. M.; Lyubimov, A. Y.; Pence, N.; Schut, G. J.; Jones, A. K.; Soltis, S. M.; Adams, M. W. W.; Raugei, S.; King, P. W.; Peters, J. W. Tuning Catalytic Bias of Hydrogen Gas Producing Hydrogenases. *J. Am. Chem. Soc.* **2020**, *142* (3), 1227–1235.

(8) Stripp, S. T.; Duffus, B. R.; Fourmond, V.; Léger, C.; Leimkühler, S.; Hirota, S.; Hu, Y.; Jasniewski, A.; Ogata, H.; Ribbe, M. W. Second and Outer Coordination Sphere Effects in Nitrogenase, Hydrogenase, Formate Dehydrogenase, and CO Dehydrogenase. *Chem. Rev.* **2022**, *122* (14), 11900–11973.

(9) Artz, J. H.; Mulder, D. W.; Ratzloff, M. W.; Lubner, C. E.; Zadvornyy, O. A.; LeVan, A. X.; Williams, S. G.; Adams, M. W. W.; Jones, A. K.; King, P. W.; Peters, J. W. Reduction Potentials of [FeFe]-Hydrogenase Accessory Iron–Sulfur Clusters Provide Insights into the Energetics of Proton Reduction Catalysis. *J. Am. Chem. Soc.* **2017**, *139* (28), 9544–9550.

(10) Kisgeropoulos, E. C.; Artz, J. H.; Blahut, M.; Peters, J. W.; King, P. W.; Mulder, D. W. Properties of the Iron-Sulfur Cluster Electron Transfer Relay in an [FeFe]-Hydrogenase That Is Tuned for H_2 Oxidation Catalysis. *J. Biol. Chem.* **2024**, *300* (6).

(11) Adams, M. W. The Mechanisms of H2 Activation and CO Binding by Hydrogenase I and Hydrogenase II of Clostridium Pasteurianum. *J. Biol. Chem.* **1987**, *262* (31), 15054–15061.

(12) Brown, K. A.; Wilker, M. B.; Boehm, M.; Dukovic, G.; King, P. W. Characterization of Photochemical Processes for H2 Production by CdS Nanorod–[FeFe] Hydrogenase

Complexes. *J. Am. Chem. Soc.* **2012**, *134* (12), 5627–5636.

(13) Wilker, M. B.; Shinopoulos, K. E.; Brown, K. A.; Mulder, D. W.; King, P. W.; Dukovic, G. Electron Transfer Kinetics in CdS Nanorod–[FeFe]-Hydrogenase Complexes and Implications for Photochemical H2 Generation. *J. Am. Chem. Soc.* **2014**, *136* (11), 4316–4324.

(14) Ratzloff, M. W.; Wilker, M. B.; Mulder, D. W.; Lubner, C. E.; Hamby, H.; Brown, K. A.; Dukovic, G.; King, P. W. Activation Thermodynamics and H/D Kinetic Isotope Effect of the Hox to HredH+ Transition in [FeFe] Hydrogenase. *J. Am. Chem. Soc.* **2017**, *139* (37), 12879–12882.

(15) Peterson, M. D.; Jensen, S. C.; Weinberg, D. J.; Weiss, E. A. Mechanisms for Adsorption of Methyl Viologen on Cds Quantum Dots. *ACS Nano* **2014**, *8* (3), 2826–2837.

(16) William Yu, W.; Qu, L.; Guo, W.; Peng, X. Experimental Determination of the Extinction Coefficient of CdTe, CdSe, and CdS Nanocrystals. *Chem. Mater.* **2003**, *15* (14), 2854–2860.

(17) Amirav, L.; Alivisatos, A. P. Photocatalytic Hydrogen Production with Tunable Nanorod Heterostructures. *J. Phys. Chem. Lett.* **2010**, *1* (7), 1051–1054.

(18) Pearce, O. M.; Duncan, J. S.; Damrauer, N. H.; Dukovic, G. Ultrafast Hole Transfer from CdS Quantum Dots to a Water Oxidation Catalyst. *J. Phys. Chem. C* **2018**, *122* (30), 17559–17565.

(19) Lorent, C.; Katz, S.; Duan, J.; Kulka, C. J.; Caserta, G.; Teutloff, C.; Yadav, S.; Apfel, U. P.; Winkler, M.; Happe, T.; Horch, M.; Zebger, I. Shedding Light on Proton and Electron Dynamics in [FeFe] Hydrogenases. *J. Am. Chem. Soc.* **2020**, *142* (12), 5493–5497.

(20) Sensi, M.; Baffert, C.; Fourmond, V.; de Gioia, L.; Bertini, L.; Léger, C. Photochemistry and Photoinhibition of the H-Cluster of FeFe Hydrogenases. *Sustain. Energy Fuels* **2021**, *5* (17), 4248–4260.

(21) Chica, B.; Ruzicka, J.; Kallas, H.; Mulder, D. W.; Brown, K. A.; Peters, J. W.; Seefeldt, L. C.; Dukovic, G.; King, P. W. Defining Intermediates of Nitrogenase MoFe Protein during N2 Reduction under Photochemical Electron Delivery from CdS Quantum Dots. *J. Am. Chem. Soc.* **2020**, *142* (33), 14324–14330.

(22) Chica, B.; Ruzicka, J.; Pellows, L. M.; Kallas, H.; Kisgeropoulos, E.; Vansuch, G. E.; Mulder, D. W.; Brown, K. A.; Svedruzic, D.; Peters, J. W.; Dukovic, G.; Seefeldt, L. C.; King, P. W. Dissecting Electronic-Structural Transitions in the Nitrogenase MoFe Protein P-Cluster during Reduction. *J. Am. Chem. Soc.* **2022**, *144* (13), 5708–5712.

(23) Vansuch, G. E.; Mulder, D. W.; Chica, B.; Ruzicka, J. L.; Yang, Z.-Y.; Pellows, L. M.; Willis, M. A.; Brown, K. A.; Seefeldt, L. C.; Peters, J. W.; Dukovic, G.; King, P. W. Cryo-Annealing of Photoreduced CdS Quantum Dot–Nitrogenase MoFe Protein Complexes Reveals the Kinetic Stability of the E4(2N2H) Intermediate. *J. Am. Chem. Soc.* **2023**, *145* (39), 21165–21169.

(24) Pellows, L. M.; Vansuch, G. E.; Chica, B.; Yang, Z.-Y.; Ruzicka, J. L.; Willis, M. A.; Clinger, A.; Brown, K. A.; Seefeldt, L. C.; Peters, J. W.; Dukovic, G.; Mulder, D. W.; King, P. W. Low-Temperature Trapping of N2 Reduction Reaction Intermediates in Nitrogenase MoFe Protein–CdS Quantum Dot Complexes. *J. Chem. Phys.* **2023**, *159* (23), 235102.

Chapter 4

(1) Brown, K. A.; Harris, D. F.; Wilker, M. B.; Rasmussen, A.; Khadka, N.; Hamby, H.; Keable, S.; Dukovic, G.; Peters, J. W.; Seefeldt, L. C.; King, P. W. Light-Driven Dinitrogen Reduction Catalyzed by a CdS:Nitrogenase MoFe Protein Biohybrid. *Science* **2016**, *352* (6284), 448.

(2) Hamby, H.; Li, B.; Shinopoulos, K. E.; Keller, H. R.; Elliott, S. J.; Dukovic, G. Light-Driven Carbon−carbon Bond Formation via CO2 Reduction Catalyzed by Complexes of CdS Nanorods and a 2-Oxoacid Oxidoreductase. *Proc. Natl. Acad. Sci.* **2020**, *117* (1), 135.

(3) Chaudhary, Y. S.; Woolerton, T. W.; Allen, C. S.; Warner, J. H.; Pierce, E.; Ragsdale, S. W.; Armstrong, F. A. Visible Light-Driven CO2 Reduction by Enzyme Coupled CdS Nanocrystals. *Chem. Commun.* **2012**, *48* (1), 58–60.

(4) Woolerton, T. W.; Sheard, S.; Reisner, E.; Pierce, E.; Ragsdale, S. W.; Armstrong, F. A. Efficient and Clean Photoreduction of CO2 to CO by Enzyme-Modified TiO2 Nanoparticles Using Visible Light. *J. Am. Chem. Soc.* **2010**, *132* (7), 2132–2133.

(5) Zhang, L.; Can, M.; Ragsdale, S. W.; Armstrong, F. A. Fast and Selective Photoreduction of CO2 to CO Catalyzed by a Complex of Carbon Monoxide Dehydrogenase, TiO2, and Ag Nanoclusters. *ACS Catal.* **2018**, *8* (4), 2789–2795.

(6) Brown, K. A.; Wilker, M. B.; Boehm, M.; Hamby, H.; Dukovic, G.; King, P. W. Photocatalytic Regeneration of Nicotinamide Cofactors by Quantum Dot–Enzyme Biohybrid Complexes. *ACS Catal.* **2016**, *6* (4), 2201–2204.

(7) Ipe, B. I.; Niemeyer, C. M. Nanohybrids Composed of Quantum Dots and Cytochrome P450 as Photocatalysts. *Angew. Chemie Int. Ed.* **2006**, *45* (3), 504–507.

(8) Ding, Y.; Lee, C. C.; Hu, Y.; Ribbe, M. M.; Nagpal, P.; Chatterjee, A. Light-Driven Transformation of Carbon Monoxide into Hydrocarbons Using CdS@ZnS : VFe Protein Biohybrids. *ChemSusChem* **2023**, *16* (20), e202300981.

(9) Brown, K. A.; Dayal, S.; Ai, X.; Rumbles, G.; King, P. W. Controlled Assembly of Hydrogenase-CdTe Nanocrystal Hybrids for Solar Hydrogen Production. *J. Am. Chem. Soc.* **2010**, *132* (28), 9672–9680.

(10) Madden, C.; Vaughn, M. D.; Díez-Pérez, I.; Brown, K. A.; King, P. W.; Gust, D.; Moore, A. L.; Moore, T. A. Catalytic Turnover of [FeFe]-Hydrogenase Based on Single-Molecule Imaging. *J. Am. Chem. Soc.* **2012**, *134* (3), 1577–1582.

(11) Brown, K. A.; Wilker, M. B.; Boehm, M.; Dukovic, G.; King, P. W. Characterization of Photochemical Processes for H2 Production by CdS Nanorod–[FeFe] Hydrogenase Complexes. *J. Am. Chem. Soc.* **2012**, *134* (12), 5627–5636.

(12) Wilker, M. B.; Shinopoulos, K. E.; Brown, K. A.; Mulder, D. W.; King, P. W.; Dukovic, G. Electron Transfer Kinetics in CdS Nanorod–[FeFe]-Hydrogenase Complexes and

Implications for Photochemical H2 Generation. *J. Am. Chem. Soc.* **2014**, *136* (11), 4316–4324.

(13) Utterback, J. K.; Wilker, M. B.; Brown, K. A.; King, P. W.; Eaves, J. D.; Dukovic, G. Competition between Electron Transfer, Trapping, and Recombination in CdS Nanorod–Hydrogenase Complexes. *Phys. Chem. Chem. Phys.* **2015**, *17* (8), 5538–5542.

(14) Utterback, J. K.; Wilker, M. B.; Mulder, D. W.; King, P. W.; Eaves, J. D.; Dukovic, G. Quantum Efficiency of Charge Transfer Competing against Nonexponential Processes: The Case of Electron Transfer from CdS Nanorods to Hydrogenase. *J. Phys. Chem. C* **2019**, *123* (1), 886–896.

(15) Utterback, J. K.; Ruzicka, J. L.; Keller, H. R.; Pellows, L. M.; Dukovic, G. Electron Transfer from Semiconductor Nanocrystals to Redox Enzymes. *Annu. Rev. Phys. Chem.* **2020**, *71* (1), 335–359.

(16) Wilker, M. B.; Utterback, J. K.; Greene, S.; Brown, K. A.; Mulder, D. W.; King, P. W.; Dukovic, G. Role of Surface-Capping Ligands in Photoexcited Electron Transfer between CdS Nanorods and [FeFe] Hydrogenase and the Subsequent H2 Generation. *J. Phys. Chem. C* **2018**, *122* (1), 741–750.

(17) Wu, K.; Zhu, H.; Liu, Z.; Rodríguez-Córdoba, W.; Lian, T. Ultrafast Charge Separation and Long-Lived Charge Separated State in Photocatalytic CdS–Pt Nanorod Heterostructures. *J. Am. Chem. Soc.* **2012**, *134* (25), 10337–10340.

(18) Klimov, V. I. Spectral and Dynamical Properties of Multiexcitons in Semiconductor Nanocrystals. *Annu. Rev. Phys. Chem.* **2007**, *58* (1), 635–673.

(19) Shulenberger, K. E.; Jilek, M. R.; Sherman, S. J.; Hohman, B. T.; Dukovic, G. Electronic Structure and Excited State Dynamics of Cadmium Chalcogenide Nanorods. *Chem. Rev.* **2023**, *123* (7), 3852–3903.

(20) Jasrasaria, D.; Philbin, J. P.; Yan, C.; Weinberg, D.; Alivisatos, A. P.; Rabani, E. Sub-Bandgap Photoinduced Transient Absorption Features in CdSe Nanostructures: The Role of Trapped Holes. *J. Phys. Chem. C* **2020**, *124* (31), 17372–17378.

(21) Morris-Cohen, A. J.; Frederick, M. T.; Cass, L. C.; Weiss, E. A. Simultaneous Determination of the Adsorption Constant and the Photoinduced Electron Transfer Rate for a Cds Quantum Dot–Viologen Complex. *J. Am. Chem. Soc.* **2011**, *133* (26), 10146–10154.

(22) Wu, K.; Du, Y.; Tang, H.; Chen, Z.; Lian, T. Efficient Extraction of Trapped Holes from Colloidal CdS Nanorods. *J. Am. Chem. Soc.* **2015**, *137* (32), 10224–10230.

(23) W., K. P.; C., P. M.; L., G. M.; Michael, S. Functional Studies of [FeFe] Hydrogenase Maturation in an Escherichia Coli Biosynthetic System. *J. Bacteriol.* **2006**, *188* (6), 2163–2172.

(24) Carbone, L.; Nobile, C.; De Giorgi, M.; Della Sala, F.; Morello, G.; Pompa, P.; Hytch, M.;

Snoeck, E.; Fiore, A.; R. Franchini, I.; Nadasan, M.; F. Silvestre, A.; Chiodo, L.; Kudera, S.; Cingolani, R.; Krahne, R.; Manna, L. Synthesis and Micrometer-Scale Assembly of Colloidal CdSe/CdS Nanorods Prepared by a Seeded Growth Approach. *Nano Lett.* **2007**, *7* (10), 2942–2950.

(25) William Yu, W.; Qu, L.; Guo, W.; Peng, X. Experimental Determination of the Extinction Coefficient of CdTe, CdSe, and CdS Nanocrystals. *Chem. Mater.* **2003**, *15* (14), 2854–2860.

(26) Amirav, L.; Paul Alivisatos, A. Photocatalytic Hydrogen Production with Tunable Nanorod Heterostructures. *J. Phys. Chem. Lett.* **2010**, *1* (7), 1051–1054.

(27) Schneider, C. A.; Rasband, W. S.; Eliceiri, K. W. NIH Image to ImageJ: 25 Years of Image Analysis. *Nat. Methods* **2012**, *9* (7), 671–675.

(28) Klinger, E.; Rickert, D.; Hasenauer, J. PyABC: Distributed, Likelihood-Free Inference. *Bioinformatics* **2018**, *34* (20), 3591–3593.

(29) Gillespie, D. T. A General Method for Numerically Simulating the Stochastic Time Evolution of Coupled Chemical Reactions. *J. Comput. Phys.* **1976**, *22* (4), 403–434.

(30) Artz, J. H.; Zadvornyy, O. A.; Mulder, D. W.; Keable, S. M.; Cohen, A. E.; Ratzloff, M. W.; Williams, S. G.; Ginovska, B.; Kumar, N.; Song, J.; McPhillips, S. E.; Davidson, C. M.; Lyubimov, A. Y.; Pence, N.; Schut, G. J.; Jones, A. K.; Soltis, S. M.; Adams, M. W. W.; Raugei, S.; King, P. W.; Peters, J. W. Tuning Catalytic Bias of Hydrogen Gas Producing Hydrogenases. *J. Am. Chem. Soc.* **2020**, *142* (3), 1227–1235.

(31) Peters, J. W.; Schut, G. J.; Boyd, E. S.; Mulder, D. W.; Shepard, E. M.; Broderick, J. B.; King, P. W.; Adams, M. W. W. [FeFe]- and [NiFe]-Hydrogenase Diversity, Mechanism, and Maturation. *Biochim. Biophys. Acta - Mol. Cell Res.* **2015**, *1853* (6), 1350–1369.

(32) Zhu, H.; Lian, T. Enhanced Multiple Exciton Dissociation from CdSe Quantum Rods: The Effect of Nanocrystal Shape. *J. Am. Chem. Soc.* **2012**, *134* (27), 11289–11297.

(33) Taguchi, S.; Saruyama, M.; Teranishi, T.; Kanemitsu, Y. Quantized Auger Recombination of Biexcitons in CdSe Nanorods Studied by Time-Resolved Photoluminescence and Transient-Absorption Spectroscopy. *Phys. Rev. B* **2011**, *83* (15), 155324.

(34) Htoon, H.; Hollingsworth, J. A.; Dickerson, R.; Klimov, V. I. Effect of Zero- to One-Dimensional Transformation on Multiparticle Auger Recombination in Semiconductor Quantum Rods. *Phys. Rev. Lett.* **2003**, *91* (22), 227401.

(35) Nakibli, Y.; Kalisman, P.; Amirav, L. Less Is More: The Case of Metal Cocatalysts. *J. Phys. Chem. Lett.* **2015**, *6* (12), 2265–2268.

(36) King, P. W.; Svedruzic, D.; Cohen, J.; Schulten, K.; Seibert, M.; Ghirardi, M. L. Structural and Functional Investigations of Biological Catalysts for Optimization of Solar-Driven H2 Production Systems. In *Proc.SPIE*; 2006; Vol. 6340, p 63400Y.

(37) Cornish-Bowden, A. *Fundamentals of Enzyme Kinetics*; John Wiley & Sons, 2013.

Chapter 5

(1) Kagan, C. R.; Lifshitz, E.; Sargent, E. H.; Talapin, D. V. Building Devices from Colloidal Quantum Dots. Science **2016**, 353 (6302), 885.

(2) García De Arquer, F. P.; Armin, A.; Meredith, P.; Sargent, E. H. Solution-Processed Semiconductors for next-Generation Photodetectors. Nat. Rev. Mater. **2017**, 2 (3), 1–16.

(3) Medintz, I. L.; Uyeda, H. T.; Goldman, E. R.; Mattoussi, H. Quantum Dot Bioconjugates for Imaging, Labelling and Sensing. Nat. Mater. **2005**, 4 (6), 435–446.

(4) Nozik, A. J.; Beard, M. C.; Luther, J. M.; Law, M.; Ellingson, R. J.; Johnson, J. C. Semiconductor Quantum Dots and Quantum Dot Arrays and Applications of Multiple Exciton Generation to Third-Generation Photovoltaic Solar Cells. Chem. Rev. **2010**, 110 (11), 6873–6890.

(5) Kamat, P. V. Quantum Dot Solar Cells. Semiconductor Nanocrystals as Light Harvesters. J. Phys. Chem. C **2008**, 112 (48), 18737–18753.

(6) Colvin, V. L.; Schlamp, M. C.; Alivisatos, A. P. Light-Emitting Diodes Made from Cadmium Selenide Nanocrystals and a Semiconducting Polymer. Nature **1994**, 370 (4), 354–357.

(7) Melnychuk, C.; Guyot-Sionnest, P. Multicarrier Dynamics in Quantum Dots. Chem. Rev. **2021**, 121 (4), 2325–2372.

(8) Zhao, L.; Hu, L.; Fang, X. Growth and Device Application of CdSe Nanostructures. Adv. Funct. Mater. **2012**, 22 (8), 1551–1566.

(9) Vokhmintcev, K. V.; Samokhvalov, P. S.; Nabiev, I. Charge Transfer and Separation in Photoexcited Quantum Dot-Based Systems. Nano Today **2016**, 11 (2), 189–211.

(10) Schimpf, A. M.; Knowles, K. E.; Carroll, G. M.; Gamelin, D. R. Electronic Doping and Redox-Potential Tuning in Colloidal Semiconductor Nanocrystals. Acc. Chem. Res. **2015**, 48 (7), 1929–1937.

(11) Guyot-Sionnest, P. Charging Colloidal Quantum Dots by Electrochemistry. Microchim. Acta **2008**, 160 (3), 309–314.

(12) Norris, D. J.; Efros, A. L.; Erwin, S. C. Doped Nanocrystals. Science **2008**, 319 (5871), 1776–1779.

(13) Haase, M.; Weller, H.; Henglein, A. Photochemistry and Radiation Chemistry of Colloidal Semiconductors. 23. Electron Storage on Zinc Oxide Particles and Size Quantization. J. Phys. Chem. **1988**, 92 (2), 482–487.

(14) Schimpf, A. M.; Gunthardt, C. E.; Rinehart, J. D.; Mayer, J. M.; Gamelin, D. R. Controlling Carrier Densities in Photochemically Reduced Colloidal ZnO Nanocrystals: Size Dependence and Role of the Hole Quencher. J. Am. Chem. Soc. **2013**, 135 (44), 16569–16577.

(15) Shim, M.; Guyot-Sionnest, P. Organic-Capped ZnO Nanocrystals: Synthesis and n-Type Character. J. Am. Chem. Soc. **2001**, 123 (47), 11651–11654.

(16) van Dijken, A.; Meulenkamp, E. A.; Vanmaekelbergh, D.; Meijerink, A. Influence of Adsorbed Oxygen on the Emission Properties of Nanocrystalline ZnO Particles. J. Phys. Chem. B **2000**, 104 (18), 4355–4360.

(17) Subramanian, V.; E. Wolf, E.; V. Kamat, P. Green Emission to Probe Photoinduced Charging Events in ZnO−Au Nanoparticles. Charge Distribution and Fermi-Level Equilibration. J. Phys. Chem. B **2003**, 107 (30), 7479–7485.

(18) Faucheaux, J. A.; Jain, P. K. Plasmons in Photocharged ZnO Nanocrystals Revealing the Nature of Charge Dynamics. J. Phys. Chem. Lett. **2013**, 4 (18), 3024–3030.

(19) Wood, A.; Giersig, M.; Mulvaney, P. Fermi Level Equilibration in Quantum Dot−Metal Nanojunctions. J. Phys. Chem. B **2001**, 105 (37), 8810–8815.

(20) Valdez, C. N.; F. Delley, M.; M. Mayer, J. Cation Effects on the Reduction of Colloidal ZnO Nanocrystals. J. Am. Chem. Soc. **2018**, 140 (28), 8924–8933.

(21) Zhang, B.; Chang, R.; Wang, K.; Lü, J.-T.; Wang, S. Optical Phonon Behaviors of Photocharged Nanocrystals: Effects of Free Charge Carriers. J. Phys. Chem. Lett. **2018**, 9 (17), 5055–5062.

(22) Rinehart, J. D.; Schimpf, A. M.; Weaver, A. L.; Cohn, A. W.; Gamelin, D. R. Photochemical Electronic Doping of Colloidal CdSe Nanocrystals. J. Am. Chem. Soc. **2013**, 135 (50), 18782–18785.

(23) Tsui, E. Y.; Hartstein, K. H.; Gamelin, D. R. Selenium Redox Reactivity on Colloidal CdSe Quantum Dot Surfaces. J. Am. Chem. Soc. **2016**, 138 (35), 11105–11108.

(24) Shim, M.; Guyot-Sionnest, P. N-Type Colloidal Semiconductor Nanocrystals. Nature **2000**, 407, 981–983.

(25) Shim, M.; Wang, C.; Guyot-Sionnest, P. Charge-Tunable Optical Properties in Colloidal Semiconductor Nanocrystals. J. Phys. Chem. B **2001**, 105 (12), 2369–2373.

(26) Wang, C.; Shim, M.; Guyot-Sionnest, P. Electrochromic Nanocrystal Quantum Dots. Science **2001**, 291 (5512), 2390–2392.

(27) Hu, R.; Wu, Z.; Zhang, Y.; R. Yakovlev, D.; Liang, P.; Qiang, G.; Guo, J.; Jia, T.; Sun, Z.;

Bayer, M.; Feng, D. Long-Lived Negative Photocharging in Colloidal CdSe Quantum Dots Revealed by Coherent Electron Spin Precession. J. Phys. Chem. Lett. **2019**, 10 (17), 4994–4999.

(28) Hartley, C. L.; Dempsey, J. L. Electron-Promoted X-Type Ligand Displacement at CdSe Quantum Dot Surfaces. Nano Lett. **2019**, 19 (2), 1151–1157.

(29) Hartstein, K. H.; Erickson, C. S.; Tsui, E. Y.; Marchioro, A.; Gamelin, D. R. Electron Stability and Negative-Tetron Luminescence in Free-Standing Colloidal n-Type CdSe/CdS Quantum Dots. ACS Nano **2017**, 11 (10), 10430–10438.

(30) Zeng, Y.; Kelley, D. F. Excited Hole Photochemistry of CdSe/CdS Quantum Dots. J. Phys. Chem. C **2016**, 120 (31), 17853–17862.

(31) Wu, K.; Lim, J.; I. Klimov, V. Superposition Principle in Auger Recombination of Charged and Neutral Multicarrier States in Semiconductor Quantum Dots. ACS Nano **2017**, 11 (8), 8437–8447.

(32) Koh, W. K.; Koposov, A. Y.; Stewart, J. T.; Pal, B. N.; Robel, I.; Pietryga, J. M.; Klimov, V. I. Heavily Doped N-Type PbSe and PbS Nanocrystals Using Ground-State Charge Transfer from Cobaltocene. Sci. Rep. **2013**, 3, 1–8.

(33) Wehrenberg, B. L.; Guyot-Sionnest, P. Electron and Hole Injection in PbSe Quantum Dot Films. J. Am. Chem. Soc. **2003**, 125 (26), 7806–7807.

(34) Araujo, J. J.; Brozek, C. K.; Kroupa, D. M.; Gamelin, D. R. Degenerately N-Doped Colloidal PbSe Quantum Dots: Band Assignments and Electrostatic Effects. Nano Lett. **2018**, 18 (6), 3893–3900.

(35) Joost, U.; Šutka, A.; Oja, M.; Smits, K.; Döbelin, N.; Loot, A.; Järvekülg, M.; Hirsimäki, M.; Valden, M.; Nõmmiste, E. Reversible Photodoping of TiO2 Nanoparticles for Photochromic Applications. Chem. Mater. **2018**, 30 (24), 8968–8974.

(36) Schimpf, A. M.; Lounis, S. D.; Runnerstrom, E. L.; Milliron, D. J.; Gamelin, D. R. Redox Chemistries and Plasmon Energies of Photodoped In2O3 and Sn-Doped In2O3 (ITO) Nanocrystals. J. Am. Chem. Soc. **2015**, 137 (1), 518–524.

(37) Palomaki, P. K. B.; Miller, E. M.; Neale, N. R. Control of Plasmonic and Interband Transitions in Colloidal Indium Nitride Nanocrystals. J. Am. Chem. Soc. **2013**, 135 (38), 14142–14150.

(38) Liu, Z.; Beaulac, R. Nature of the Infrared Transition of Colloidal Indium Nitride Nanocrystals: Nonparabolicity Effects on the Plasmonic Behavior of Doped Semiconductor Nanomaterials. Chem. Mater. **2017**, 29 (17), 7507–7514.

(39) Liu, H.; Keuleyan, S.; Guyot-Sionnest, P. N- and p-Type HgTe Quantum Dot Films. J. Phys.

Chem. C **2011**, 116 (1), 1344–1349.

(40) Seob Jeong, K.; Deng, Z.; Keuleyan, S.; Liu, H.; Guyot-Sionnest, P. Air-Stable n-Doped Colloidal HgS Quantum Dots. J. Phys. Chem. Lett. **2014**, 5 (7), 1139–1143.

(41) Wheeler, L. M.; Neale, N. R.; Chen, T.; Kortshagen, U. R. Hypervalent Surface Interactions for Colloidal Stability and Doping of Silicon Nanocrystals. Nat. Commun. **2013**, 4, 1–10.

(42) Burke, R.; Bren, K. L.; Krauss, T. D. Semiconductor Nanocrystal Photocatalysis for the Production of Solar Fuels. J. Chem. Phys. **2021**, 154 (3), 030901.

(43) Utterback, J. K.; Ruzicka, J. L.; Keller, H. R.; Pellows, L. M.; Dukovic, G. Electron Transfer from Semiconductor Nanocrystals to Redox Enzymes. Annu. Rev. Phys. Chem. **2020**, 71 (1), 335–359.

(44) Li, X.-B.; Xin, Z.-K.; Xia, S.-G.; Gao, X.-Y.; Tung, C.-H.; Wu, L.-Z. Semiconductor Nanocrystals for Small Molecule Activation via Artificial Photosynthesis. Chem. Soc. Rev. **2020**, 49 (24), 9028–9056.

(45) Tang, Z. R.; Han, B.; Han, C.; Xu, Y. J. One Dimensional CdS Based Materials for Artificial Photoredox Reactions. J. Mater. Chem. A **2017**, 5 (6), 2387–2410.

(46) Cheng, L.; Xiang, Q.; Liao, Y.; Zhang, H. CdS-Based Photocatalysts. Energy Environ. Sci. **2018**, 11 (6), 1362–1391.

(47) Wilker, M. B.; Schnitzenbaumer, K. J.; Dukovic, G. Recent Progress in Photocatalysis Mediated by Colloidal II-VI Nanocrystals. Isr. J. Chem. **2012**, 52 (11–12), 1002–1015.

(48) Wu, K.; Du, Y.; Tang, H.; Chen, Z.; Lian, T. Efficient Extraction of Trapped Holes from Colloidal CdS Nanorods. J. Am. Chem. Soc. **2015**, 137 (32), 10224–10230.

(49) Zhu, H.; Yang, Y.; Wu, K.; Lian, T. Charge Transfer Dynamics from Photoexcited Semiconductor Quantum Dots. Annu. Rev. Phys. Chem. **2016**, 67 (1), 259–281.

(50) Chen, P. E.; Anderson, N. C.; Norman, Z. M.; Owen, J. S. Tight Binding of Carboxylate, Phosphonate, and Carbamate Anions to Stoichiometric CdSe Nanocrystals. J. Am. Chem. Soc. **2017**, 139 (8), 3227–3236.

(51) Wang, J.; Ding, T.; Wu, K. Electron Transfer into Electron-Accumulated Nanocrystals: Mimicking Intermediate Events in Multielectron Photocatalysis II. J. Am. Chem. Soc. **2018**, 140 (32), 10117–10120.

(52) Amirav, L.; Alivisatos, A. P. Photocatalytic Hydrogen Production with Tunable Nanorod Heterostructures. J. Phys. Chem. Lett. **2010**, 1 (7), 1051–1054.

(53) Amirav, L.; Alivisatos, A. P. Luminescence Studies of Individual Quantum Dot

Photocatalysts. J. Am. Chem. Soc. **2013**, 135 (35), 13049–13053.

(54) Simon, T.; Bouchonville, N.; Berr, M. J.; Vaneski, A.; Adrovic, A.; Volbers, D.; Wyrwich, R.; Döblinger, M.; Susha, A. S.; Rogach, A. L.; Jäckel, F.; Stolarczyk, J. K.; Feldmann, J. Redox Shuttle Mechanism Enhances Photocatalytic H2 Generation on Ni-Decorated CdS Nanorods. Nat. Mater. **2014**, 13 (11), 1013–1018.

(55) Li, Q.; Zhao, F.; Qu, C.; Shang, Q.; Xu, Z.; Yu, L.; R. McBride, J.; Lian, T. Two-Dimensional Morphology Enhances Light-Driven H2 Generation Efficiency in CdS Nanoplatelet-Pt Heterostructures. J. Am. Chem. Soc. **2018**, 140 (37), 11726–11734.

(56) Yu, W. W.; Qu, L.; Guo, W.; Peng, X. Experimental Determination of the Extinction Coefficient of CdTe, CdSe, and CdS Nanocrystals. Chem. Mater. **2003**, 15 (14), 2854–2860.

(57) Peterson, M. D.; Jensen, S. C.; Weinberg, D. J.; Weiss, E. A. Mechanisms for Adsorption of Methyl Viologen on Cds Quantum Dots. ACS Nano **2014**, 8 (3), 2826–2837.

(58) Dhaene, E.; Billet, J.; Bennett, E.; Van Driessche, I.; De Roo, J. The Trouble with ODE: Polymerization during Nanocrystal Synthesis. Nano Lett. **2019**, 19 (10), 7411–7417.

(59) Yu, W. W.; Peng, X. Formation of High-Quality CdS and Other II - VI Semiconductor Nanocrystals in Noncoordinating Solvents: Tunable Reactivity of Monomers. Communications **2002**, 114 (13), 2368–2371.

(60) Manthiram, K.; Beberwyck, B. J.; Talapin, D. V.; Alivisatos, A. P. Seeded Synthesis of CdSe/CdS Rod and Tetrapod Nanocrystals. J. Vis. Exp. **2013**, 82 (82), 50731.

(61) Boatman, E. M.; Lisensky, G. C.; Nordell, K. J. A Safer, Easier, Faster Synthesis for CdSe Quantum Dot Nanocrystals. J. Chem. Educ. **2005**, 82 (11), 1697–1699.

(62) Pearce, O. M.; Duncan, J. S.; Damrauer, N. H.; Dukovic, G. Ultrafast Hole Transfer from CdS Quantum Dots to a Water Oxidation Catalyst. J. Phys. Chem. C **2018**, 122 (30), 17559–17565.

(63) Schneider, C. A.; Rasband, W. S.; Eliceiri, K. W. NIH Image to ImageJ: 25 Years of Image Analysis. Nat. Methods **2012**, 9 (7), 671–675.

(64) Tseng, H.-W.; B. Wilker, M.; H. Damrauer, N.; Dukovic, G. Charge Transfer Dynamics between Photoexcited CdS Nanorods and Mononuclear Ru Water-Oxidation Catalysts. J. Am. Chem. Soc. **2013**, 135 (9), 3383–3386.

(65) Klimov, V. I. Spectral and Dynamical Properties of Multiexcitons in Semiconductor Nanocrystals. Annu. Rev. Phys. Chem. **2007**, 58 (1), 635–673.

(66) Kambhampati, P. Unraveling the Structure and Dynamics of Excitons in Semiconductor Quantum Dots. Acc. Chem. Res. **2011**, 44 (1), 1–13.

(67) Cohn, A. W.; Rinehart, J. D.; Schimpf, A. M.; Weaver, A. L.; Gamelin, D. R. Size Dependence of Negative Trion Auger Recombination in Photodoped Cdse Nanocrystals. Nano Lett. **2014**, 14 (1), 353–358.

(68) Klimov, V. I.; Mikhailovsky, A. A.; McBranch, D. W.; Leatherdale, C. A.; Bawendi, M. G. Quantization of Multiparticle Auger Rates in Semiconductor Quantum Dots. Science **2000**, 287 (5455), 1011–1014.

(69) Sewall, S. L.; Cooney, R. R.; Anderson, K. E. H.; Dias, E. A.; Kambhampati, P. State-to-State Exciton Dynamics in Semiconductor Quantum Dots. Phys. Rev. B **2006**, 74 (23), 1–8.

(70) Peterson, M. D.; Cass, L. C.; Harris, R. D.; Edme, K.; Sung, K.; Weiss, E. A. The Role of Ligands in Determining the Exciton Relaxation Dynamics in Semiconductor Quantum Dots. Annu. Rev. Phys. Chem. **2014**, 65 (1), 317–339.

(71) Klimov, V. I.; Schwarz, C. J.; McBranch, D. W.; Leatherdale, C. A.; Bawendi, M. G. Ultrafast Dynamics of Inter- and Intraband Transitions in Semiconductor Nanocrystals: Implications for Quantum-Dot Lasers. Phys. Rev. B **1999**, 60 (4), R2177–R2180.

(72) Klimov, V. I.; McBranch, D. W.; Leatherdale, C. A.; Bawendi, M. G. Electron and Hole Relaxation Pathways in Semiconductor Quantum Dots. Phys. Rev. B **1999**, 60 (19), 13740–13749.

(73) Sewall, S. L.; Cooney, R. R.; Kambhampati, P. Experimental Tests of Effective Mass and Atomistic Approaches to Quantum Dot Electronic Structure: Ordering of Electronic States. Appl. Phys. Lett. **2009**, 94 (24), 243116.

(74) Tsui, E. Y.; Carroll, G. M.; Miller, B.; Marchioro, A.; Gamelin, D. R. Extremely Slow Spontaneous Electron Trapping in Photodoped N-Type CdSe Nanocrystals. Chem. Mater. **2017**, 29 (8), 3754–3762.

(75) Park, Y.-S.; Ki Bae, W.; M. Pietryga, J.; I. Klimov, V. Auger Recombination of Biexcitons and Negative and Positive Trions in Individual Quantum Dots. ACS Nano **2014**, 8 (7), 7288–7296.

(76) Koch, M.; Kheng, K.; Robin, I. C.; André, R. Biexcitonic Complexes and the Decay Dynamics of Trion and Exciton in a Single CdSe Quantum Dot. Phys. Status Solidi Curr. Top. Solid State Phys. **2006**, 3 (11), 3916–3919.

(77) Türck, V.; Rodt, S.; Heitz, R.; Stier, O.; Strassburg, M.; Pohl, U. W.; Bimberg, D. Charged Excitons and Biexcitons in Self-Organized CdSe Quantum Dots. Phys. Status Solidi Basic Res. **2001**, 224 (1), 217–221.

(78) Bonati, C.; Mohamed, M. B.; Tonti, D.; Zgrablic, G.; Haacke, S.; Van Mourik, F.; Chergui, M. Spectral and Dynamical Characterization of Multiexcitons in Colloidal CdSe

Semiconductor Quantum Dots. Phys. Rev. B **2005**, 71 (20), 1–6.

(79) Kilina, S.; Ivanov, S.; Tretiak, S. Effect of Surface Ligands on Optical and Electronic Spectra of Semiconductor Nanoclusters. J. Am. Chem. Soc. **2009**, 131 (22), 7717–7726.

(80) Kalyuzhny, G.; W. Murray, R. Ligand Effects on Optical Properties of CdSe Nanocrystals. J. Phys. Chem. B **2005**, 109 (15), 7012–7021.

(81) Bullen, C.; Mulvaney, P. The Effects of Chemisorption on the Luminescence of CdSe Quantum Dots. Langmuir **2006**, 22 (7), 3007–3013.

(82) Krause, M. M.; Kambhampati, P. Linking Surface Chemistry to Optical Properties of Semiconductor Nanocrystals. Phys. Chem. Chem. Phys. **2015**, 17 (29), 18882–18894.

(83) De Roo, J.; Yazdani, N.; Drijvers, E.; Lauria, A.; Maes, J.; S. Owen, J.; Van Driessche, I.; Niederberger, M.; Wood, V.; C. Martins, J.; Infante, I.; Hens, Z. Probing Solvent–Ligand Interactions in Colloidal Nanocrystals by the NMR Line Broadening. Chem. Mater. **2018**, 30 (15), 5485–5492.

(84) Kitaguchi, H.; Ohkubo, K.; Ogo, S.; Fukuzumi, S. Electron-Transfer Oxidation Properties of Unsaturated Fatty Acids and Mechanistic Insight into Lipoxygenases. J. Phys. Chem. A **2006**, 110 (5), 1718–1725.

(85) Van De Walle, C. G.; Neugebauer, J. Universal Alignment of Hydrogen Levels in Semiconductors, Insulators and Solutions. Nature **2003**, 423, 626–628.

(86) Walukiewicz, W. Intrinsic Limitations to the Doping of Wide-Gap Semiconductors. Phys. B **2001**, 302–303, 123–134.

(87) Knauf, R. R.; Lennox, J. C.; Dempsey, J. L. Quantifying Ligand Exchange Reactions at CdSe Nanocrystal Surfaces. Chem. Mater. **2016**, 28 (13), 4762–4770.

(88) Cohn, A. W.; Janßen, N.; Mayer, J. M.; Gamelin, D. R. Photocharging ZnO Nanocrystals: Picosecond Hole Capture, Electron Accumulation, and Auger Recombination. J. Phys. Chem. C **2012**, 116 (38), 20633–20642.

(89) Hines, D. A.; Kamat, P. V. Recent Advances in Quantum Dot Surface Chemistry. ACS Appl. Mater. Interfaces **2014**, 6 (5), 3041–3057.

(90) Xu, L.; Liang, H. W.; Yang, Y.; Yu, S. H. Stability and Reactivity: Positive and Negative Aspects for Nanoparticle Processing. Chem. Rev. **2018**, 118 (7), 3209–3250.

(91) Hagfeldt, A.; Graetzel, M. Light-Induced Redox Reactions in Nanocrystalline Systems. Chem. Rev. **1995**, 95 (1), 49–68.

(92) Young, R. M.; Jensen, S. C.; Edme, K.; Wu, Y.; Krzyaniak, M. D.; Vermeulen, N. A.; Dale,

E. J.; Stoddart, J. F.; Weiss, E. A.; Wasielewski, M. R.; Co, D. T. Ultrafast Two-Electron Transfer in a CdS Quantum Dot–Extended-Viologen Cyclophane Complex. J. Am. Chem. Soc. **2016**, 138 (19), 6163–6170.

(93) Zhu, H.; Song, N.; Lv, H.; L. Hill, C.; Lian, T. Near Unity Quantum Yield of Light-Driven Redox Mediator Reduction and Efficient H2 Generation Using Colloidal Nanorod Heterostructures. J. Am. Chem. Soc. **2012**, 134 (28), 11701–11708.

(94) Kalisman, P.; Nakibli, Y.; Amirav, L. Perfect Photon-to-Hydrogen Conversion Efficiency. Nano Lett. **2016**, 16 (3), 1776–1781.

(95) Cohn, A. W.; Schimpf, A. M.; Gunthardt, C. E.; Gamelin, D. R. Size-Dependent Trap-Assisted Auger Recombination in Semiconductor Nanocrystals. Nano Lett. **2013**, 13 (4), 1810–1815.